On Impact and Volcanism across the Cretaceous-Paleogene Boundary

On Impact and Volcanism across the Cretaceous-Paleogene Boundary

Pincelli M. Hull[1*◆], André Bornemann[2*◆], Donald Penman[1◆], Michael J. Henehan[1,3◆], Richard D. Norris[4◆†], Paul A. Wilson[5◆†], Peter Blum[6◆†], Laia Alegret[7], Sietske Batenburg[8†], Paul R. Bown[9†], Timothy J. Bralower[10], Cecile Cournede[11,12†], Alexander Deutsch[13†], Barbara Donner[14], Oliver Friedrich[15†], Sofie Jehle[16†], Hojung Kim[9†], Dick Kroon[17], Peter Lippert[18†],Dominik Loroch[13†], Iris Moebius[15,19†], Kazuyoshi Moriya[20†], Daniel J. Peppe[21], Gregory E. Ravizza[22†], Ursula Röhl[14†], Jonathan D. Schueth[23], Julio Sepúlveda[24†], Philip Sexton[25†], Elizabeth Sibert[4,26,27†], Kasia K. Śliwińska[28†], Roger E. Summons[29†], Ellen Thomas[1,30], Thomas Westerhold[14†], Jessica H. Whiteside[5†], Tatsuhiko Yamaguchi[31†], James C. Zachos[32]

[1] Department of Geology and Geophysics, Yale University, 210 Whitney Ave, New Haven, CT 06511, USA
[2] Bundesanstalt für Geowissenschaften und Rohstoffe, Stilleweg 2, 30655 Hannover, Germany
[3] GFZ German Research Centre for Geosciences, Telegrafenberg, 14473 Potsdam, Germany
[4] Scripps Institution of Oceanography, University of California San Diego, 9500 Gilman Drive, La Jolla, CA 92093-0244, USA
[5] National Oceanography Centre Southampton, University of Southampton, Waterfront Campus, European Way, Southampton SO14 3ZH, UK
[6] International Ocean Discovery Program, Texas A&M University, 1000 Discovery Drive, College Station, TX 77845, USA
[7] Departamento de Ciencias de la Tierra & Instituto Universitario de Ciencias Ambientales, Universidad Zaragoza, 50009 Zaragoza, Spain
[8] Géosciences, Université de Rennes 1, Campus de Beaulieu, 35042 Rennes, France
[9] Department of Earth Sciences, University College London, Gower Street, London WC1E 6BT, UK
[10] Department of Geosciences, Pennsylvania State University, University Park, PA, USA
[11] CEREGE, Université Aix-Marseille, Europole de l'Arbois BP 80 1, 13545 Aix en Provence, France
[12] Institute for Rock Magnetism, University of Minnesota, John T. Tale Hall, 116 Church St. SE, Minneapolis, MN 55455, USA
[13] Institut für Planetologie, Universität Münster, Wihelm-Klemm-St. 10, 48149 Münster, Germany
[14] MARUM – Center for Marine Environmental Sciences, University of Bremen, Leobener Strasse 8, 28359 Bremen, Germany
[15] Institute of Earth Sciences, Heidelberg University, Im Neuenheimer Feld 234-236, 69120 Heidelberg, Germany
[16] Institut für Geophysik und Geologie, Universität Leipzig, Talstr. 35, 04103 Leipzig, Germany
[17] School of Geosciences, University of Edinburgh, Edinburgh EH8 9XP, United Kingdom
[18] Department of Geology & Geophysics, The University of Utah, 115 S 1460 E, Salt Lake City, UT 84112-0102, USA
[19] Department of Biogeochemical Systems, Max Planck Institute for Biogeochemistry, Hans-Knöll St. 10, 07745 Jena, Germany
[20] Department of Earth Sciences, Waseda University, Nishiwaseda 1-6-1, Shinjyuku-ku, Tokyo 169-8050, Japan
[21] Department of Geosciences, Baylor University, One Bear Place #97354, Waco Texas 76798-7354, USA
[22] Department of Geology & Geophysics, University of Hawai'I at Manoa, Honolulu, HI 96822, USA
[23] ConocoPhillips Company, 925 N Eldridge Pkwy, Houston, TX 77079, USA
[24] Department of Geological Sciences and Institute of Arctic and Alpine Research, University of Colorado Boulder, UCB 450, Boulder CO 830309-0450, USA
[25] School of Environment, Earth & Ecosystem Sciences, The Open University, Walton Hall, Milton Keynes MK7 6AA, UK
[26] Harvard Society of Fellows, Harvard University, 78 Mount Auburn Street, Cambridge, MA 02138, USA
[27] Department of Earth and Planetary Sciences, Harvard University, 20 Oxford Street, Cambridge, MA 02138, USA
[28] Department of Stratigraphy, Geological Survey of Denmark and Greenland (GEUS), Øster Voldgade 10, DK-1350 Copenhagen K, Denmark
[29] Department of Earth, Atmospheric and Planetary Science, Massachusetts Institute of Technology, Cambridge, MA 02139, USA
[30] Department of Earth and Environmental Sciences, Wesleyan University, Middletown CT 06459, USA
[31] National Museum of Nature and Science, 4-1-1 Amakubo, Tsukuba, 305-0005, Japan
[32] Department of Earth and Planetary Sciences, University of California Santa Cruz, CA 95064, USA

[*] Co-first authors (pincelli.hull@yale.edu and andre.bornemann@bgr.de)
[◆] First seven authors in order of contribution, all others alphabetical
[†] Primary Contribution: IODP Expedition 342 K/Pg boundary investigation

Abstract

The cause of the end-Cretaceous mass extinction is vigorously debated due to the occurrence of a very large bolide impact and flood basalt volcanism near the boundary. Disentangling their relative importance is complicated by uncertainty regarding kill mechanisms and the relative timing of volcanogenic outgassing, impact, and extinction. We use carbon cycle modeling and paleotemperature records to constrain the timing of volcanogenic outgassing. We found support for major outgassing beginning and ending distinctly prior to the impact, with only impact coinciding with mass extinction and biologically amplified carbon cycle change. Our models show that these extinction-related carbon cycle changes would have allowed the ocean to absorb massive amounts of CO_2, thus limiting the global warming otherwise expected from post-extinction volcanism.

Introduction

Sixty-six million years ago two planetary-scale disturbances occurred within less than a million years of one another. An asteroid of more than 10 km in diameter collided with the Yucatan Peninsula at the boundary between the Cretaceous and the Paleogene (~66 Ma), producing the ~200 km wide Chicxulub impact crater (*1-4*). Impact markers at hundreds of sites globally co-occur with the deposition of the Cretaceous-Paleogene (K/Pg) boundary clay and include elevated abundances of siderophilic elements such as iridium, osmium, and nickel, and tektites and shocked quartz (*1, 5, 6*). During the K/Pg boundary-spanning magnetochron C29r (65.688-66.398 Ma, ~ 710,000 years long (*7*)), an estimated ~500,000 km^3 of lava flooded across much of India and into the deep sea in a large igneous province (LIP) known as the Deccan Traps (*8, 9*). Deccan volcanism was, like most flood basalt eruptions (*9-11*), episodic, with flows deposited in pulses throughout magnetochron C29r (*12, 13*). That both volcanism and the impact event occurred within several hundred thousand years of the K/Pg extinctions is beyond reasonable doubt (*5, 9, 12, 13*). However, this still leaves many aspects uncertain, including the relative timing and magnitude of volcanic effects on the biosphere (*13, 14*), the potential relationship between impact and volcanism (*8, 13, 15*), and whether impact or volcanism acted as the sole, primary, or joint drivers of extinction (*5, 10, 16*).

The case for the Chicxulub impact as a driver of K/Pg mass extinction includes processes hypothesized to operate during the days and decades following the collision. The bolide impact injected an estimated >50,000 km^3 of ejecta (*4*), ~ 325 Gt of sulfur and ~425 Gt CO_2 and other volatiles (*17*) into the atmosphere from the marine carbonate and anhydrite target rock of the Yucatan Peninsula (*5, 18*). The combined effects of an expanding impact fireball and the re-entry of molten ejecta from the skies (*19*) may have raised temperatures to the point of spontaneous combustion near the impactor and caused severe heat stress and even death many thousands of km away from the impact site in minutes to days after impact (*20*). In the days to years that followed, nitrogen and sulfur vapors reacted to form nitric and sulfuric acids and, with CO_2 gases, acidified the oceans (*21-23*). Finally, models and empirical evidence suggest that the combination of dust and aerosols precipitated a severe impact winter in the decades post-impact (*24-27*).

Impressive though these environmental effects may be, some researchers question whether the Chicxulub impactor acted as the sole or main driver of the K/Pg mass extinction for three primary reasons. First, no single kill mechanism appears to explain the extinction patterns: acidification (*28, 29*) and primary productivity decline (*30*) (due to darkness and cold (*26*)) are favored in the marine realm, whereas heat exposure and/loss of productivity (due to fires, darkness and cold (*18, 26*)) are favored in the terrestrial realm (*31, 32*). Second, asteroid and comet impacts occur throughout the history of life (although likely none in the last ~500 Myr of the size and force of Chicxulub (*33*)), but no other mass extinction is unambiguously linked to such a collision (*34*). Third, flood basalt volcanism is strongly implicated as the driver of two of the greatest mass extinctions in the last half billion years (the Permian-Triassic [P/T] and Triassic-Jurassic [T/J]) leading some to favor a similar role for Deccan volcanism in the K/Pg mass extinction (e.g., *35*). However, most episodes of flood basalt volcanism after the T/J produced no increase in extinction rates (*36*), potentially due to important Earth system changes that dampened the effects of flood basalts post-P/T.

Questions regarding the role of Deccan volcanism in driving the K/Pg mass extinction arise because of the relative lack of evidence for a volcanogenic driver. Despite advances in chronology, the timing of the most voluminous Deccan eruptions relative to the K/Pg extinctions

remains unclear (e.g., ref. 8 vs. 9). Many earlier authors argued that most Deccan flood basalts (>85%) were emplaced in a relatively short interval before the K/Pg, starting around the C29r/C30n boundary (~66.39 Ma) and ending well before the K/Pg impact (*11, 12*). In contrast, Renne et al. (*13*) and Sprain et al. (*9*) proposed that the vast majority of Deccan basalts were emplaced after the impact. Schoene et al. (*8*) largely agree with the basalt flow ages of refs. 9 and 13, but place the K/Pg boundary higher in the lava pile (i.e., the upper part of, or above, the Poladpur unit), and therefore propose major pulses of emplacement just before and just after the impact (*8*).

Pre- and post-impact scenarios are debated in part because they are tied to different environmental disruption scenarios. Pre-event volcanism may have acted in concert with the impact to drive K/Pg extinctions (*10*), whereas post-event volcanism suggests a role for volcanism in the delayed recovery of biodiversity (*13*). For the environment and life, the main environmental effects of large igneous provinces are attributed to volatile release (*37-39*), not lava emplacement, and the magnitude of volcanic outgassing is not necessarily linked directly to the volume of erupted lava. If early eruptive phases of flood basalt volcanism have higher volatile concentrations, then most volatiles could have been released before the impact, even if most of the lava was emplaced afterwards (*9*).

Here we provide constraints on Deccan Trap outgassing by comparing exceptionally well-resolved and temporally detailed ocean drilling and global temperature records, with five modeled end-member scenarios for the timing, magnitude, and composition of outgassing (*40*). These comparisons allow us to consider the relative effects of Deccan Trap outgassing and bolide impact on the marine carbon cycle and biological change.

Marine environmental record of outgassing

Deccan Trap degassing released a mix of volatiles including sulfur dioxide (SO_2), chlorine (Cl) and other halogens, and carbon dioxide (CO_2), with sulfur having perhaps the greatest direct effect on ecosystems through acidification and pronounced global cooling (>4.5°C) (*38*). The environmental effects of sulfur dioxide, however, would have been relatively short-lived (years to centuries at most) and difficult to detect in slowly accumulating deep-sea sediments. In

contrast, the influence of CO_2 emissions should be clearly evident in marine sediments as a global warming event paired with a carbon isotope anomaly (*41*). We used this diagnostic fingerprint of CO_2 emissions as a proxy for the timing of potentially disruptive outgassing of sulfur (and other noxious gasses) and to test which volcanic degassing scenarios are compatible with the observed record.

Two dominant features are clear in our global temperature compilation (Fig. 1) (*40*). First, marine and terrestrial records show a late Maastrichtian warming event of ~2°C on average (Figs. S1-S16; *42, 43, 44*) in the Cretaceous part of C29r that cools back to pre-event temperatures prior to the K/Pg boundary (Fig. 1). Second, the earliest Danian has temperatures comparable to those in the late Maastrichtian prior to the warming event, with temperatures gradually increasing to become >1°C warmer on average by ~600 kyr after the impact. Benthic foraminiferal oxygen isotope records typically track changes in global mean temperatures, and they show both these features (Figs. 1, 2, S13a), as do most other archives (Figs. S1-S16). The two exceptions are the bulk carbonate records and fish teeth phosphate records from El Kef (Figs. S10c, S11, S12), which likely do not track global temperature for extinction-related reasons (*40*), thus we excluded them from the calculation of global mean temperatures.

Our multiproxy, astronomically tuned record from the North Atlantic site (*45*) has an exceptionally complete Maastrichtian sequence and a mm-thick tektite layer at the K-Pg boundary (Figs. 2, S17-S19). The record documents an excursion to lower values in $\delta^{13}C$ in bulk sediments coincident with $\delta^{18}O$ decline (a warming indicator) as well as a decline in osmium isotope values (Fig. 2, S20-S21). Similar patterns are seen in records from the South Atlantic Walvis Ridge and the North Pacific Shatsky Rise (Figs. 2, S18-S19; *42, 46*). The similarity of these records amongst three such widespread localities and four sites (Fig. 2), suggests that they provide a remarkably complete record of magnetochron C29r. Slight temporal offsets in the apparent onset and recovery from latest Maastrichtian warming (among all sites) and in early Paleogene carbon isotope patterns at Shatsky Rise, due either to short unconformities and/or the limitations of cyclostratigraphic age models, illustrate the current temporal uncertainties (Fig. 2). Temperature and atmospheric CO_2, as reflected in both our $\delta^{18}O$ and $\delta^{13}C$ anomalies, and recent boron isotope records (*23*), returned to pre-warming values in the very latest Maastrichtian. The

most prominent feature in the records is the dramatic decline in $\delta^{13}C$ isotopes and change in sedimentary $CaCO_3$ content beginning at the K/Pg boundary (Fig. 2).

We investigated the timing of Deccan Trap outgassing by modeling the effects of CO_2 and sulfur emissions on long-term global temperatures using the geochemical box model LOSCAR (Long-term Ocean Sediment CArbon Reservoir v. 2.0.4) (*47*). Guided by published hypotheses for the timing and volume of trap emplacement, we tested five major Deccan Trap emission scenarios differing in the timing of volatile release: (i) Case 1: Leading, majority (87%) of degassing pre-K/Pg boundary (after (*10*)) (ii) Case 2: 50/50, half of degassing prior to and half following the K/Pg boundary (after lower estimate in (*9*)); (iii) Case 3: Punctuated, four pulses with one major event just preceding the K/Pg boundary (after (*8*)), (iv) Case 4: Lagging, majority (87%) of degassing post-K/Pg boundary (inverse Case 1 pre-/post- outgassing volumes, (*13*)); and (v) Case 5: Spanning, emissions released evenly throughout magnetochron C29r (after (*12*)) (Table 1). All volcanic outgassing scenarios assume the same (i) initial climatic and oceanographic conditions: 600 ppm pCO_2 and climate sensitivity of 2-4°C per CO_2 doubling (*41*), LOSCAR's Paleogene ocean configuration and circulation, and marine $[Mg^{2+}]$ of 42 mmol/kg and $[Ca^{2+}]$ of 21 mmol/kg; (ii) K/Pg impact volatile release from the target rock (325 Gt S; 425 Gt CO_2)(*17*); (iii) upper and lower end-estimates for total volcanic outgassing volumes (4091-9545 Gt C and 3200-8500 Gt S (*10*) at constant ratios) (*40*); and iv) extinction related changes in the marine carbon cycle (*41, 48*) (including reductions in both organic carbon and carbonate export and increases in intermediate-depth organic carbon remineralization, see Table 1) that taper back to pre-event values over 1.77 Myr following the extinction (*49*). In most outgassing scenarios, we assumed a common onset of Deccan degassing at the C30n/C29r boundary, following geochronology of the traps (*8, 9, 12, 50*). In the GTS 2012 age framework (*7*) used to align the temperature records, C30n/C29r is 358 kyr prior to the K/Pg boundary, rather than the ~250-300 kyrs indicated by the most recent $^{40}Ar/^{39}Ar$ and U-Pb geochronology (*8, 50*). Simulations were initially tuned (*40*) to find the biological scenario (iv) that minimized data-model mismatches (Figs. S22-S27) and multiple scenarios for climate sensitivity and outgassing are considered in assessing goodness of fit (Figs. 3-4, S25, S28-S32, Table 2).

Three modeled scenarios differ distinctly from the observed pattern of temperature change (Fig. 3), thus we consider them unlikely to represent the true outgassing history. Case 3 fails to reproduce the late Maastrichtian warming and shows a pronounced boundary-crossing warming event that is not supported by proxy data. In Case 4, late Maastrichtian warming is too muted and early Paleocene warming is too pronounced, and in Case 5 warming increases up to the K/Pg boundary, unlike the empirical record (Fig. 3). Relatively poor model fit is also indicated by high mean absolute errors (MAEs) for Cases 3 and 4 as compared to Cases 1 and 2 (Table 2). The temporal dynamics of $\delta^{13}C$ in Cases 3 and 5 also deviate from the empirical record (Fig 4).

Only two outgassing scenarios produce modeled temperatures resembling the empirical records: the leading case (Case 1) and the 50:50 case (Case 2). We thus consider these the two most likely of the tested scenarios to represent Deccan Trap outgassing. In Case 1, most CO_2 and SO_2 degassing occurred in the latest Maastrichtian, leading to global warming and subsequent cooling prior to the K/Pg. The relatively constant early Paleocene temperatures of Case 1, with a gradual warming over the 600kyrs following the impact, are also consistent with empirical records (Figs. 1-3, S17-S18). Case 2 (50:50) also matches the empirical temperature record well (Fig. 3), with the lowest MAEs of all cases (Table 2). The Late Cretaceous warming differs between Case 1 and Case 2 due to the reduced Late Cretaceous volcanic outgassing in the latter. Although uncertainty about climate sensitivity (*51*) and total Deccan Trap emissions (*10, 12*) has a greater effect on modeled temperatures than the difference in outgassing volume (Figs. 3, S25, S28), carbon isotopes also support Case 2 as the more likely scenario (Fig. 4; MAEs in Table S31).

The climatic effects of a major pulse (50%) of Deccan outgassing released over the ~350 kyr immediately following the impact (Case 2) were limited by extinction-related changes to the carbon cycle, including the reduction in $CaCO_3$ export from pelagic calcifiers to the seafloor. Marine $CaCO_3$ export indirectly affects atmospheric CO_2 by changing the distribution of carbon and alkalinity between the surface and deep-ocean, and slows the removal of alkalinity from the system via $CaCO_3$ burial (*41*). The difference between Case 1 and 2 is almost imperceptible, with Case 2 having slightly warmer (~0.25°C) early Danian temperatures than Case 1. Notably, more rapid Paleocene outgassing, such as modeled in Case 3 (ref. 8), exceeds the capacity of the altered marine carbon cycle to absorb CO_2.

Our results inform several important boundary debates. First, if there was a large pulse of emplacement just 20-60 kyrs prior to the impact (*8*), most CO_2 outgassing (and associated environmental impacts) must have preceded lava emplacement by several hundred thousand years. This would be prior to the eruption of the most voluminous stages of Deccan volcanism (i.e., pre-Wai subgroup) as modeled for Case 1 and 2 (Fig. 3-4; see expanded discussion in (*40*)). Second, roughly equal pre- and post-impact volcanic degassing is supported (i.e., Case 2, Figs. 3-4), a hypothesized scenario in ref. 9. However, our results are not consistent with most (>75%) volcanogenic degassing post-impact (i.e., outgassing more similar to eruptive volumes in refs. *9, 13*), because modeled warming is too muted in the Cretaceous and too pronounced in the early Paleocene (i.e., Case 4) as compared to empirical records (Fig. 3). Third, impact-related volatile release from the target rock has a negligible climatic effect (Fig. S24), so is unlikely to account for the dramatic warming indicated by fish teeth $\delta^{18}O$ in the first 100 kyr (*52*). Instead, this record likely predominantly reflects changes in fish biology rather than temperature. Fourth, biotic recovery can account for the apparently gradual early Danian warming as observed in marine records if it begins at or shortly after impact and occurs over >1.5 myr. This biotic recovery scenario reproduces the general pattern of change in $\delta^{13}C$ gradients (Figs. 2, S27), carbonate saturation state (Figs. 2c, S27) and temperature, but differs from recovery hypotheses that posit a delay in the onset of biological recovery for ~ 500kyr or more (e.g., *40, 49, 53*).

No marine evidence for joint cause in mass extinction

The fossil record indicates no lasting, outsized, or cascading effect of the late Maastrichtian warming event on marine ecosystems of the sort that might predispose them to mass extinction by impact. First, we found no evidence for elevated extinction rates in the latest Cretaceous in marine taxa (Table S1), excepting a contested record from Seymour Island, Antarctica (e.g., *54, 55*). The scarcity of biostratigraphic datums in the Cretaceous portion of magnetochron C29r signifies a conspicuous lack of extinction in widespread species including planktonic foraminifera, nannoplankton, radiolarians, and ammonites (*7*). Second, late Cretaceous outgassing did not have a lasting effect on the community structure of well-fossilized taxa. Although range and community shifts coincided with warming, a shift back to the pre-warming-like communities occurred prior to impact (see Table S1). Third, marine carbon cycle indicators

($\delta^{13}C$ and carbonate deposition) show no discernable effect of late Maastrichtian outgassing and warming on a major ecosystem function: the export and cycling of carbon. The $\delta^{13}C$ anomaly size (~0.2-0.3 per mil; see also ref. *44*) is consistent with a volcanogenic driver as in Case 2 (Figs. 2, 4, S28) given the magnitude of warming, without biological amplification.

In contrast, major and enduring changes to ecosystems coincided with the K/Pg impact. In deep-sea records, impact markers occur at the level of the abrupt mass extinction of >90% planktonic foraminifera and 93% of nannoplankton species (Fig. 2). These groups exhibit rapid turnover and high dominance in community composition in the first 500 kyrs of the Paleocene (*56, 57*), an interval where bulk carbonate $\delta^{18}O$ likely reflects community composition rather than surface ocean temperatures (Figs. 5, S33-S35). At the same time, tracers of the marine carbon cycle indicate a profound change in marine ecosystem function. The community structure of some groups such as small fishes, which show no evidence of elevated extinction, changed permanently (*58*). The $\delta^{13}C$ composition of planktonic foraminifera and nannoplankton fell to or below that of benthic foraminifera at the iridium anomaly (Figs. 2,5, S34-S35; *43, 49*). The loss or inversion of the $\delta^{13}C$ gradient typically maintained by the biological pump is unmatched in the fossil record of pelagic calcifiers (~170 million years), and indicates that the K/Pg boundary impact had an outsized effect on the marine carbon cycle.

After the impact, an already altered marine carbon cycle is needed to counteract the CO_2 emitted by a major post-impact pulse of outgassing as in Case 2 (Fig. 3) to avoid a warming event of the same magnitude as the Late Cretaceous warming event. This suggests that the major ecological change of the K/Pg mass extinction must have occurred prior to any major post-impact volcanism. Our modeling does support a scenario in which Deccan volcanism could have contributed to the aftermath of the impact and mass extinction as in (*13*), if environmentally destructive gases such as SO_2, halogens, or sulfate aerosols contributed to (or drove) the persistence of unusual marine communities for the first ~500 kyrs of the Paleocene. This might be particularly true if the evolution of the magma chamber led to higher sulfur content of later emissions, as in other eruption types (*59*). However, no observations document acidification coupled to extreme cold snaps in the earliest Paleocene as predicted by this hypothesis, and there

is no explanation for why SO_2 would have greater biotic effects in the well-buffered early Danian oceans than in the latest Maastrichtian oceans (Fig. S1-S18).

Conclusion

We combined climatic, biotic, and carbon cycle records with modeled impact and outgassing scenarios, and found support for a bolide impact as the primary driver of the end-Cretaceous mass extinction. Our analysis suggests that roughly 50% of Deccan Trap CO_2 outgassing occurred well before the impact, but does not support the suggestion (*8*) that a large outgassing event took place just before (~10-60 kyrs). This suggests a pronounced decoupling between CO_2 outgassing and lava flow emplacement if ref. 8 is correct, or a relative impact and eruption chronology similar to ref. 9 and our best-supported, 50:50 outgassing scenario. The Late Cretaceous warming event attributed to Deccan degassing is of a comparable size to small warming events in the Paleocene and early Eocene that are not associated with elevated extinction or turnover (*43, 60*), similar to what we find for the late Maastrichtian. We therefore conclude that impact and extinction created the initial opportunity for the rise of Cenozoic species and communities, but Deccan volcanism might have contributed to shaping them during the extinction aftermath.

Acknowledgements: This research used samples and/or data provided by the International Ocean Discovery Program (IODP), which was sponsored by the US National Science Foundation and participating countries under management of Joint Oceanographic Institutions, Inc, and its predecessors –the (Integrated) Ocean Drilling Program and the Deep Sea Drilling Program. We thank the JOIDES Resolution crew of IODP Expedition 342 and W. Hale and A. Wuelbers for help with sampling. We also thank the many centers and staff scientists who enabled the measurements, including Leanne Elder in the Hull Lab (Yale University), Brad Erkkila and Marvin Wint at the Yale Analytical and Stable Isotope Center, Dyke Andreasen at the UCSC Stable Isotope Laboratory, and F. Demory (CERGE) for help with magnetic data production and processing. This work benefited from helpful discussions with Jaume Dinarès-Turell, the insights of C. Brenhin Keller, and the comments of four anonymous reviewers.
Funding: IODP USSSP Post-Expedition Activity award and Yale University support to P.M.H.; Deutsche Forschungsgemeinschaft [DFG; grant numbers BO2505/8-1, EH 89/20-2] funding for

A.B.; Yale Peabody Museum support to M.J.H.; Spanish Ministry of Economy and Competitiveness and FEDER funds (CGL2017-84693-R) to L.A.; DFG funding [grant number VO687/14] to S.J.B.; a Richard Foster Flint Postdoctoral Fellowship (Dept. G&G, Yale University) for D.P.; DFG funding [grant number FR2544/2] to O.F.; NSF funding (EAR-132552) and American Chemical Society Petroleum Research Fund grant (PRF#52822-DN18) to D.J.P; DFG funding [grant numbers RO1113/3, RO1113/4, and RO1113/8] to U.R.; a NASA Exobiology Program grant (NNX09AM88G) to R.E.S.; a Danish Council for Independent Research/Natural Sciences (DFF/FNU; Grant 11-107497) award to K.K.Ś; NSF funding (OCE #1536611) to E.T; DFG funding [grant number WE5479/3] to T.W; and a NERC (NE/K006800/1) and Royal Society Wolfson award to P.A.W. **Author contributions:** Among the first six authors, P.M.H conceived and co-led the study, drafted the manuscript, contributed to model design, generated empirical data, and edited data tables and figures; A.B. co-led the study and coordinated data generation, reporting, figures, and tables, generated empirical data and substantially contributed to the study design and text; D.P. led LOSCAR modeling and substantially contributed to study design and text, M.J.H. compiled and aligned age models for the global temperature compilation, prepared related tables and figures, and substantially contributed to the study design and text; R.D.N., P.A.W, and P.B. led IODP Expedition 342, with R.D.N. and P.A.W. substantially contributing to study design and text. Among the remaining co-authors, L.A., S.B., P.R.B., T.J.B., C.C., A.D., B.D., O.F., S.J., H.K., D.K., P.L., D.L., I.M., K.M., D.J.P., G.E.R., U.R., J.S., J.D.S., E.S., K.K.Ś., R.E.S., E.T., T.W., J.H.W., and T.Y. contributed empirical datasets, figures, and related analyses, interpretations and text; and L.A., P.R.B., T.J.B., O.F., D.K., P.S., J.S., E.T., T.W., J.H.W., J.C.Z. substantially contributed to ideas and/or text. All authors read and approved the final text. **Data and materials availability:** all data is available in the manuscript and the supplementary material.

References

1. L. W. Alvarez, W. Alvarez, F. Asaro, H. V. Michel, Extraterrestrial cause for the Cretaceous-Tertiary extinction - experimental results and theoretical interpretation. *Science* **208**, 1095-1108 (1980).
2. A. R. Hildebrand *et al.*, Chicxulub crater - a possible Cretaceous Tertiary Boundary impact crater on the Yucatan Peninsula, Mexico. *Geology* **19**, 867-871 (1991).
3. B. Collen *et al.*, Clarifying misconceptions of extinction risk assessment with the IUCN Red List. *Biology Letters* **12**, 20150843 (2016).
4. J. Morgan *et al.*, Size and morphology of the Chicxulub impact crater. *Nature* **390**, 472-476 (1997).
5. P. Schulte *et al.*, The Chicxulub Asteroid Impact and Mass Extinction at the Cretaceous-Paleogene Boundary. *Science* **327**, 1214-1218 (2010).
6. G. Ravizza, D. VonderHaar, A geochemical clock in earliest Paleogene pelagic carbonates based on the impact-induced Os isotope excursion at the Cretaceous-Paleogene boundary. *Paleoceanography* **27**, PA3219 (2012).
7. F. M. Gradstein, J. G. Ogg, M. D. Schmitz, G. M. Ogg, *The Geologic Time Scale 2012*. (Elsevier B.V., Amsterdam, 2012).
8. B. Schoene *et al.*, U-Pb constraints on pulsed eruption of the Deccan Traps across the end-Cretaceous mass extinction. *Science* **363**, 862-866 (2019).
9. C. J. Sprain *et al.*, The eruptive tempo of Deccan volcanism in relation to the Cretaceous-Paleogene boundary. *Science* **363**, 866-870 (2019).
10. A. L. Chenet *et al.*, Determination of rapid Deccan eruptions across the Cretaceous-Tertiary boundary using paleomagnetic secular variation: 2. Constraints from analysis of eight new sections and synthesis for a 3500-m-thick composite section. *Journal of Geophysical Research-Solid Earth* **114**, B06103 (2009).
11. A. L. Chenet, X. Quidelleur, F. Fluteau, V. Courtillot, S. Bajpai, K-40-Ar-40 dating of the Main Deccan large igneous province: Further evidence of KTB age and short duration. *Earth and Planetary Science Letters* **263**, 1-15 (2007).
12. B. Schoene *et al.*, U-Pb geochronology of the Deccan Traps and relation to the end-Cretaceous mass extinction. *Science* **347**, 182-184 (2015).
13. P. R. Renne *et al.*, State shift in Deccan volcanism at the Cretaceous-Paleogene boundary, possibly induced by impact. *Science* **350**, 76-78 (2015).
14. P. R. Renne *et al.*, Time Scales of Critical Events Around the Cretaceous-Paleogene Boundary. *Science* **339**, 684-687 (2013).
15. M. A. Richards *et al.*, Triggering of the largest Deccan eruptions by the Chicxulub impact. *Geological Society of America Bulletin* **127**, 1507-1520 (2015).
16. E. Font *et al.*, Deccan volcanism induced high-stress environment during the Cretaceous-Paleogene transition at Zumaia, Spain: Evidence from magnetic, mineralogical and biostratigraphic records. *Earth and Planetary Science Letters* **484**, 53-66 (2018).
17. N. Artemieva, J. Morgan, E. S. Party, Quantifying the Release of Climate-Active Gases by Large Meteorite Impacts With a Case Study of Chicxulub. *Geophysical Research Letters* **44**, 10180-10188 (2017).
18. S. P. S. Gulick *et al.*, The first day of the Cenozoic. *Proceedings of the National Academy of Sciences of the United States of America* **116**, 19342-19351 (2019).

19. D. A. Kring, D. D. Durda, Trajectories and distribution of material ejected from the Chicxulub impact crater: implications for postimpact wildfires. *Journal of Geophysical Research-Planets* **107**, (2002).
20. J. Morgan, N. Artemieva, T. Goldin, Revisiting wildfires at the K-Pg boundary. *J Geophys Res-Biogeo* **118**, 1508-1520 (2013).
21. S. Ohno *et al.*, Production of sulphate-rich vapour during the Chicxulub impact and implications for ocean acidification. *Nature Geoscience* **7**, 279-282 (2014).
22. T. Tyrrell, A. Merico, D. I. A. McKay, Severity of ocean acidification following the end-Cretaceous asteroid impact. *Proceedings of the National Academy of Sciences of the United States of America* **112**, 6556-6561 (2015).
23. M. J. Henehan *et al.*, Rapid ocean acidification and protracted Earth System recovery followed the end-Cretaceous Chixulub impact. *Proceedings of the National Academy of Sciences of the United States of America*, (2019).
24. J. Vellekoop *et al.*, Rapid short-term cooling following the Chicxulub impact at the Cretaceous-Paleogene boundary. *Proceedings of the National Academy of Sciences of the United States of America* **111**, 7537-7541 (2014).
25. K. Kaiho *et al.*, Global climate change driven by soot at the K-Pg boundary as the cause of the mass extinction. *Sci Rep-Uk* **6**, (2016).
26. J. Brugger, G. Feulner, S. Petri, Baby, it's cold outside: Climate model simulations of the effects of the asteroid impact at the end of the Cretaceous. *Geophysical Research Letters* **44**, 419-427 (2017).
27. C. G. Bardeen, R. R. Garcia, O. B. Toon, A. J. Conley, On transient climate change at the Cretaceous-Paleogene boundary due to atmospheric soot injections. *Proceedings of the National Academy of Sciences of the United States of America* **114**, E7415-E7424 (2017).
28. L. Alegret, E. Thomas, K. C. Lohmann, End-Cretaceous marine mass extinction not caused by productivity collapse. *Proceedings of the National Academy of Sciences of the United States of America* **109**, 728-732 (2012).
29. B. J. Marshall, R. C. Thunell, M. J. Henehan, Y. Astor, K. E. Wejnert, Planktonic foraminiferal area density as a proxy for carbonate ion concentration: A calibration study using the Cariaco Basin ocean time series. *Paleoceanography* **28**, 363-376 (2013).
30. M. Aberhan, S. Weidemeyer, W. Kiessling, R. A. Scasso, F. A. Medina, Faunal evidence for reduced productivity and uncoordinated recovery in Southern Hemisphere Cretaceous-Paleogene boundary sections. *Geology* **35**, 227-230 (2007).
31. P. M. Sheehan, T. A. Hansen, Detritus Feeding as a Buffer to Extinction at the End of the Cretaceous. *Geology* **14**, 868-870 (1986).
32. D. S. Robertson, M. C. McKenna, O. B. Toon, S. Hope, J. A. Lillegraven, Survival in the first hours of the Cenozoic. *Geological Society of America Bulletin* **116**, 760-768 (2004).
33. E. M. Shoemaker, Impact cratering through geologic time. *Journal of the Royal Astronomical Society of Canada* **92**, 297-309 (1998).
34. J. D. Archibald *et al.*, Cretaceous Extinctions: Multiple Causes. *Science* **328**, 973-973 (2010).
35. G. Keller, J. Punekar, P. Mateo, Upheavals during the Late Maastrichtian: Volcanism, climate and faunal events preceding the end-Cretaceous mass extinction. *Palaeogeography Palaeoclimatology Palaeoecology* **441**, 137-151 (2016).
36. S. V. Sobolev *et al.*, Linking mantle plumes, large igneous provinces and environmental catastrophes. *Nature* **477**, 312-U380 (2011).

37. M. T. Jones, D. A. Jerram, H. H. Svensen, C. Grove, The effects of large igneous provinces on the global carbon and sulphur cycles. *Palaeogeography Palaeoclimatology Palaeoecology* **441**, 4-21 (2016).
38. A. Schmidt *et al.*, Selective environmental stress from sulphur emitted by continental flood basalt eruptions. *Nature Geoscience* **9**, 77-82 (2016).
39. S. Self, S. Blake, K. Sharma, M. Widdowson, S. Sephton, Sulfur and chlorine in Late Cretaceous Deccan magmas and eruptive gas release. *Science* **319**, 1654-1657 (2008).
40. Materials and methods are available as supplementary materials at the Science website.
41. M. J. Henehan, P. M. Hull, D. E. Penman, J. W. B. Rae, D. N. Schmidt, Biogeochemical significance of pelagic ecosystem function: an end-Cretaceous case study. *Philosophical Transactions of the Royal Society B-Biological Sciences* **371**, 20150510 (2016).
42. J. S. K. Barnet *et al.*, A new high-resolution chronology for the late Maastrichtian warming event: Establishing robust temporal links with the onset of Deccan volcanism. *Geology* **46**, 147-150 (2018).
43. J. S. K. Barnet *et al.*, A high-fidelity benthic stable isotope record of Late Cretaceous-Early Eocene climate change and carbon-cycling. *Paleoceanography and Paleoclimatology* **34**, 672-691 (2019).
44. L. Q. Li, G. Keller, Abrupt deep-sea warming at the end of the Cretaceous. *Geology* **26**, 995-998 (1998).
45. R. D. Norris, P. A. Wilson, P. Blum, a. t. E. Scientists, in *Proc. IODP, 342,* R. D. Norris, Wilson, P.A., Blum, P., and the Expedition 342 Scientists, Ed. (Integrated Ocean Drilling Program, College Station, TX, 2014).
46. N. Robinson, G. Ravizza, R. Coccioni, B. Peucker-Ehrenbrink, R. Norris, A high-resolution marine Os-187/Os-188 record for the late Maastrichtian: distinguishing the chemical fingerprints of Deccan volcanism and the KP impact event. *Earth and Planetary Science Letters* **281**, 159-168 (2009).
47. R. E. Zeebe, LOSCAR: Long-term Ocean-atmosphere-Sediment CArbon cycle Reservoir Model v2.0.4. *Geoscientific Model Development* **5**, 149-166 (2012).
48. J. C. Zachos, M. A. Arthur, W. E. Dean, Geochemical evidence for suppression of pelagic marine productivity at the Cretaceous/Tertiary boundary. *Nature* **337**, 61-64 (1989).
49. H. S. Birch, H. K. Coxall , P. N. Pearson, D. Kroon, D. N. Schmidt, Partial collapse of the marine carbon pump after the Cretaceous-Paleogene boundary. *Geology* **44**, 287-290 (2016).
50. C. J. Sprain, P. R. Renne, W. A. Clemens, G. P. Wilson, Calibration of chron C29r: New high-precision geochronologic and paleomagnetic constraints from the Hell Creek region, Montana. *Geological Society of America Bulletin* **130**, 1615-1644 (2018).
51. E. J. Rohling *et al.*, Comparing Climate Sensitivity, Past and Present. *Annual Review of Marine Science, Vol 10* **10**, 261-+ (2018).
52. K. G. MacLeod, P. C. Quinton, J. Sepulveda, M. H. Negra, Postimpact earliest Paleogene warming shown by fish debris oxygen isotopes (El Kef, Tunisia). *Science* **360**, 1467-1469 (2018).
53. S. D'Hondt, P. Donaghay, J. C. Zachos, D. Luttenberg, M. Lindinger, Organic carbon fluxes and ecological recovery from the Cretaceous-Tertiary mass extinction. *Science* **282**, 276-279 (1998).

54. J. D. Witts *et al.*, Macrofossil evidence for a rapid and severe Cretaceous-Paleogene mass extinction in Antarctica. *Nat Commun* **7**, 11738 (2016).
55. T. S. Tobin, Recognition of a likely two phased extinction at the K-Pg boundary in Antarctica. *Sci Rep-Uk* **7**, 16317 (2017).
56. P. M. Hull, R. D. Norris, T. J. Bralower, J. D. Schueth, A role for chance in marine recovery from the end-Cretaceous extinction. *Nature Geoscience* **4**, 856-860 (2011).
57. J. J. Pospichal, in *The Cretaceous-Tertiary event and other catastrophes in Earth history: Geological Society of America Special Paper 307,* G. Ryder, D. Fastovsky, S. Gartner, Eds. (1996), pp. 335-360.
58. E. C. Sibert, M. Friedman, P. M. Hull, G. Hunt, R. D. Norris, Two pulses of origination in Pacific pelagic fish following the Cretaceous-Paleogene Mass Extinction. *Proceedings of the Royal Society B-Biological Sciences*, 20181194 (2018).
59. M. Edmonds, New geochemical insights into volcanic degassing. *Philosophical Transactions of the Royal Society a-Mathematical Physical and Engineering Sciences* **366**, 4559-4579 (2008).
60. P. F. Sexton *et al.*, Eocene global warming events driven by ventilation of oceanic dissolved organic carbon. *Nature* **471**, 349-352 (2011).
61. R. D. Norris, in *Palaeobiology II,* D. E. G. Briggs, P. G. Crowther, Eds. (Blackwell Science Ltd., Oxford, 2001), pp. 229-231.

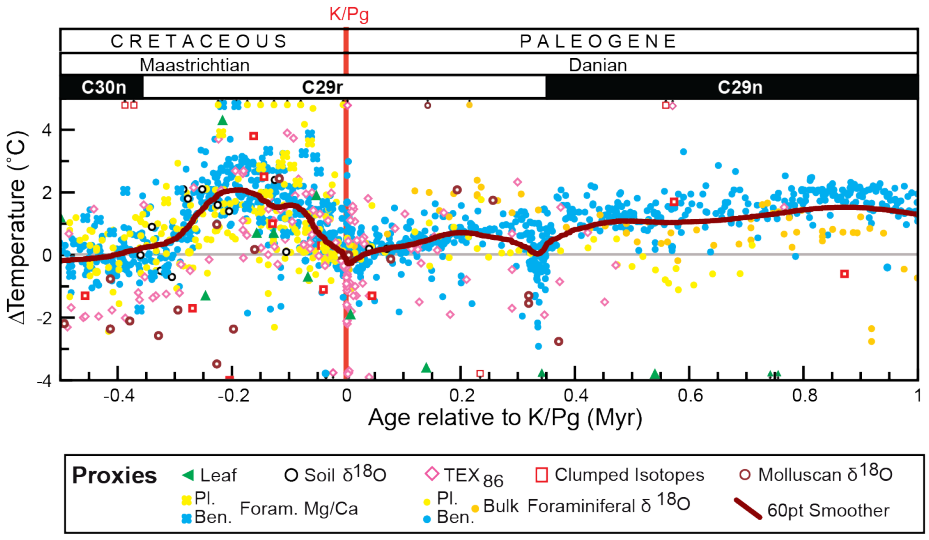

Figure 1. Global temperature change across the Cretaceous-Paleogene boundary. New and existing empirical temperature records from marine sediments (foraminiferal $\delta^{18}O$ and Mg/Ca, TEX_{86}), shallow marine carbonates (clumped isotopes of mollusk carbonate), and terrestrial proxies (leaf margin analysis, biomarkers, clumped isotopes of mollusk carbonate) were aligned to common age model (Table S2 and S3) and normalized to the latest Cretaceous temperature within each record. A 60pt fast Fourier transform smoother of global temperature change is shown in dark red. Data are provided in Table S4-S12. Some outlying data points do not fall within plot bounds, but can be seen in Figs. S1-S16.

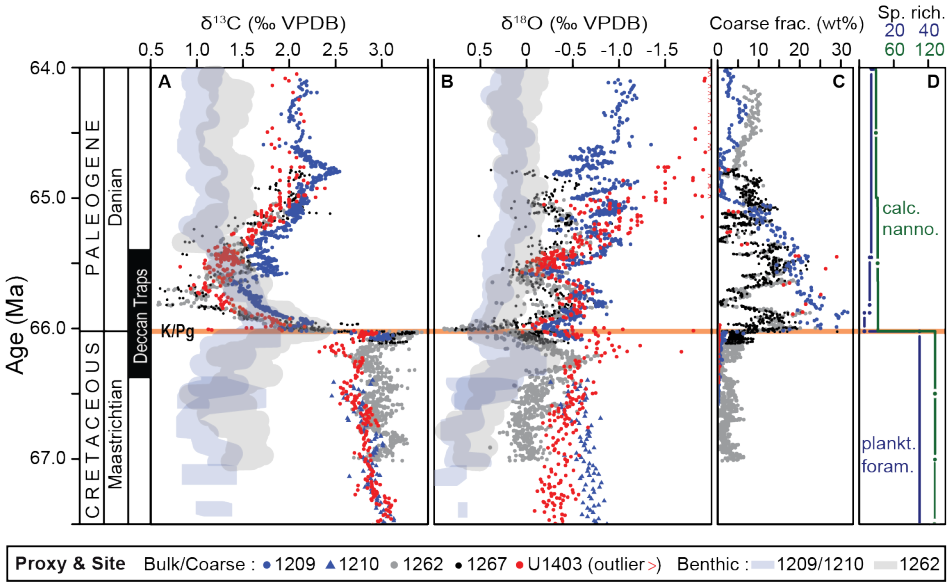

Figure 2. K/Pg boundary dynamics at the best-resolved deep-sea sites globally: Shatsky Rise, Walvis Ridge, and J-Anomaly Ridge. High resolution carbon (A) and oxygen (B) isotope dynamics in benthic foraminifera (transparent lines) and bulk carbonate (discrete points), and sediment composition (C, weight % coarse fraction), at Shatsky Rise (blue), Walvis Ridge (grey), and J-Anomaly Ridge (red), compared to (D) global records of nannofossil (grey) and foraminifera (blue, from (*61*)) species richness (*40*). Major interval of Deccan Trap emplacement (estimated 93% of volume) indicated at left by the black bar, after ref 9.

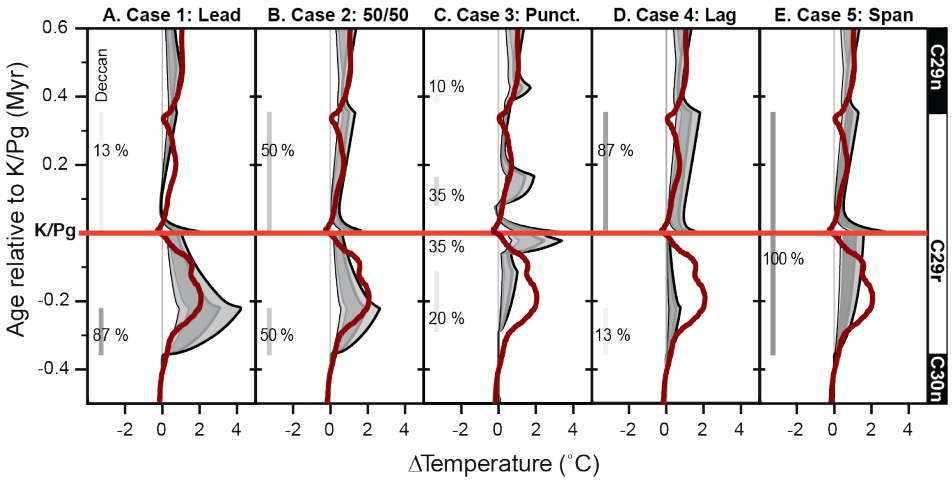

Figure 3. Global temperature change across the Cretaceous-Paleogene boundary as compared to five scenarios for Deccan Trap outgassing. Outgassing scenarios include (A) Case 1 (Leading): most outgassing prior to impact, (B) Case 2 (50/50): 50% outgassing prior to and 50% post impact, (C) Case 3 (Punctuated), (D) Case 4 (Lagging): most outgassing post impact, and (E) Case 5 (Spanning): continuous outgassing throughout magnetochron C29r (Table 1). Each model scenario is represented by four lines (bounding a shaded region) delineating different combinations of climate sensitivity and volcanic outgassing: high degassing (9545 GtC and 8500 GtS) and 3°C/doubling (thick grey line); high degassing and 4°C/doubling (thick black line); low degassing (4090 GtC and 3200 GtS) and 3°C/doubling (thin grey line), and low degassing and 2°C/doubling (thin black line), and compared to a 60pt fast Fourier transform smoother of global temperature change (red line) from Fig. 1. Deccan outgassing timing indicated by bars at left, with the shading intensity of the bar indicative of the proportion outgassing in that interval.

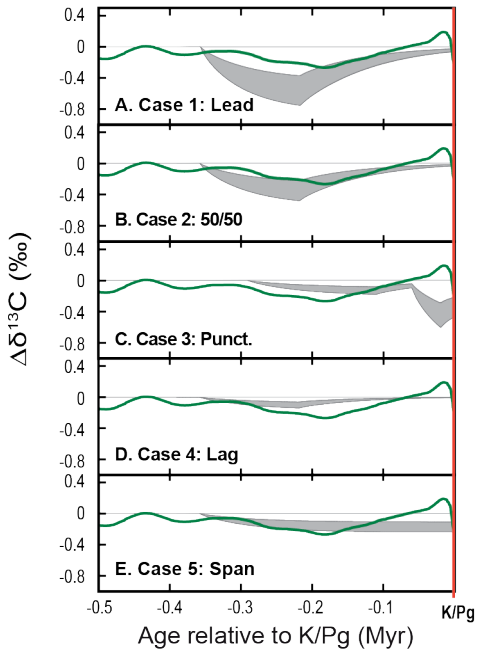

497

498

499 **Figure 4. Surface ocean $\delta^{13}C$ change across the late Maastrichtian warming as compared to**
500 **five scenarios for Deccan Trap outgassing.** Bulk carbonate $\Delta\delta^{13}C$ (20pt fast Fourier transform
501 smoother of Site U1403 and Site 1262 data) shown against surface ocean $\delta^{13}C$ for end-member
502 outgassing and climate sensitivity scenarios (grey envelope) for each case as detailed in Fig. 3. In
503 each case, carbonate carbon isotopes are expressed as $\Delta\delta^{13}C$, relative to the late Maastrichtian
504 high of 3.03 ‰ at 0.432 Myr prior to the onset of the CO_2 release (see also Figs. S36-S37).

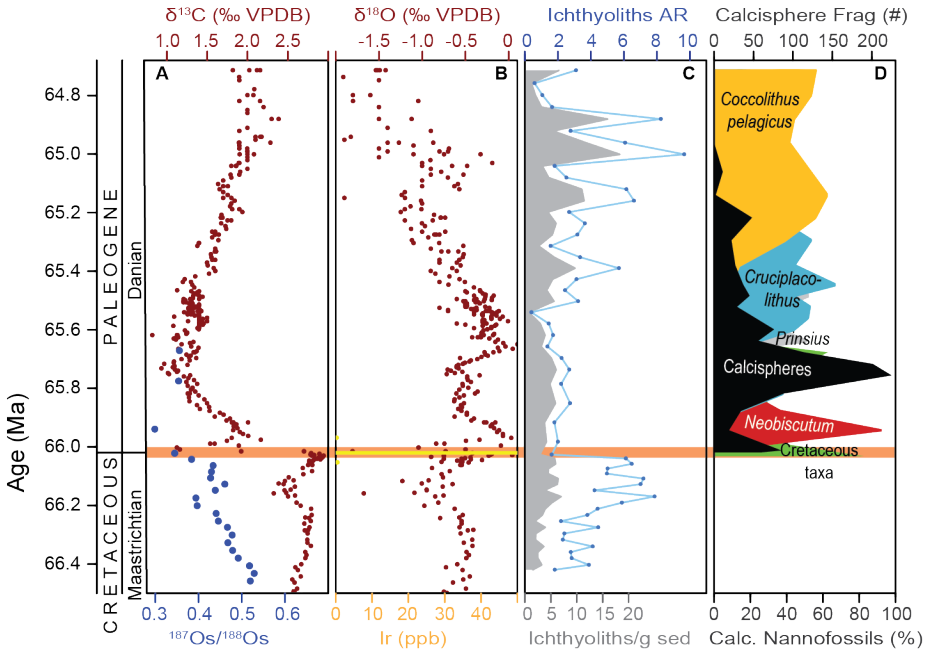

505

506 **Figure 5. Late Cretaceous warming and early Paleocene record of environmental and**
507 **biotic change at IODP Site U1403, J-Anomaly Ridge, Newfoundland.** A negative carbon
508 isotope anomaly (A) coincides with late Cretaceous warming in $\delta^{18}O$ (B), and osmium isotope
509 evidence for volcanism (A) at IODP Site U1403. The collapse in surface ocean $\delta^{13}C$ values (A)
510 coincides with iridium anomaly (B), and step change in fish tooth accumulation (C). Earliest
511 Paleocene $\delta^{18}O$ values of bulk carbonate appear to be strongly influenced by vital effects driven
512 by rapid turnover in the dominant calcareous nannofossil taxa (D) in sites globally (Figs. S18,
513 S34, S35). Data in Tables S12, S16, S17, S29.

514

515

Table 1. Model parameters for five focal Deccan outgassing scenarios tested in LOSCAR.

		Case 1: Leading	Case 2: 50/50	Case 3: Punct.	Case 4: Lagging	Case 5: Spanning
Volcanic Outgassing	*Pulse 1 (Pre): Volume*	87% of total h: 8305 Gt C, 7395 Gt S l: 3559 Gt C, 2784 Gt S	50% of total high: 4773 Gt C, 4250 Gt S low: 2045 Gt C, 1600 Gt S	20% of total h: 1909 Gt C, 1700 Gt S l: 818 Gt C, 640 Gt S	13% of total high: 1241 Gt C, 1105 Gt S low: 532 Gt C, 416 Gt S	100% of total high: 9545 Gt C, 8500 Gt S low: 4091 Gt C, 3200 Gt S
	Timing	Starts: -358 kyr Ends: -218 kyr	Starts: -358 kyr Ends: -218 kyr	Starts: -290 kyr Ends: -110 kyr	Starts: -358 kyr Ends: -218 kyr	Starts: -358 kyr Ends: 355 kyr
	Pulse 2 (Pre): Volume			35% of total h: 3340 Gt C, 2975 Gt S l: 1431 Gt C, 1120 Gt S		
	Timing			Starts: -60 kyr Ends: -20 kyr		
	Pulse 1 (Post): Volume	13% of total h: 1241 Gt C, 1105 Gt S l: 532 Gt C, 416 Gt S	50% of total high: 4773 Gt C, 4250 Gt S low: 2045 Gt C, 1600 Gt S	35% of total h: 3340 Gt C, 2975 Gt S l: 1431 Gt C, 1120 Gt S	87% of total high: 8305 Gt C, 7395 Gt S low: 3559 Gt C, 2784 Gt S	
	Timing	Starts: 0 kyr Ends: 355 kyr	Starts: 0 kyr Ends: 355 kyr	Starts: 80 kyr Ends: 170 kyr	Starts: 0 kyr Ends: 355 kyr	
	Pulse 2 (Post): Volume			10% of total h: 955 Gt C, 850 Gt S l: 409 Gt C, 320 Gt S		
	Timing			Starts: 390 kyr Ends: 430 kyr		
Impact Outgas.	*Volume*	100% of total 115 Gt C, 325 Gt S	100% of total 115 Gt C, 325 Gt S	100% of total 115 Gt C, 325 Gt S	100% of total 115 Gt C, 325 Gt S	100% of total 115 Gt C, 325 Gt S
	Timing	Starts: 0 kyr Ends: 1 kyr	Starts: 0 kyr Ends: 1 kyr	Starts: 0 kyr Ends: 1 kyr	Starts: 0 kyr Ends: 1 kyr	Starts: 0 kyr Ends: 1 kyr
Biotic Change	*Organic Export Flux Δ*	50% reduction	50% reduction	50% reduction	50% reduction	50% reduction
	$CaCO_3$ Export Flux Δ	42.5% reduction	42.5% reduction	42.5% reduction	42.5% reduction	42.5% reduction
	Frac. Int.-depth C_{org} remin. Δ	22% increase	22% increase	22% increase	22% increase	22% increase
	Timing	Starts: 0 kyr immediately tapers Ends: 1770 kyr	Starts: 0 kyr immediately tapers Ends: 1770 kyr	Starts: 0 kyr immediately tapers Ends: 1770 kyr	Starts: 0 kyr immediately tapers Ends: 1770 kyr	Starts: 0 kyr immediately tapers Ends: 1770 kyr

Table 2. Mean absolute error (MAE) and mean minimum absolute error (MMAE) of cases relative to the interpolated global temperature record. The mean minimum absolute error (MMAE) was calculated for each case by determining whether the empirical data fell outside of the temperature range bounded by the high and low outgassing scenarios given a climate sensitivity of 3°C/CO_2 doubling, and, if so, by how much. MAEs were also calculated for each outgassing volume and climate sensitivity shown in Fig. 3. MMAEs and MAEs were calculated on a 20 kyr interpolated time step from 360kyr prior to 600 kyr post K/Pg. Case 2 consistently has the lowest MAEs and Case 1 and 2 have the lowest MMAEs.

	Mean Min. Abs. Error	***High Volc., 3°C/CO_2 doub.***	***High Volc., 4°C/CO_2 doub.***	***Low Volc., 3°C/CO_2 doub***	***Low Volc., 2°C/CO_2 doub***
Case 1	0.25	0.46	0.65	0.50	0.58
Case 2	0.21	0.35	0.43	0.48	0.58
Case 3	0.45	0.59	0.65	0.58	0.64
Case 4	0.45	0.61	0.69	0.56	0.63
Case 5	0.29	0.40	0.44	0.53	0.61

Supplementary Materials for

On Impact and Volcanism across the Cretaceous-Paleogene Boundary

Pincelli M. Hull, André Bornemann, Donald Penman, Michael J. Henehan, Richard D. Norris, Paul A. Wilson, Peter Blum, Laia Alegret, Sietske Batenburg, Paul R. Bown, Timothy J. Bralower, Cecile Cournede, Alexander Deutsch, Barbara Donner, Oliver Friedrich, Sofie Jehle, Hojung Kim, Dick Kroon, Peter Lippert,Dominik Loroch, Iris Moebius, Kazuyoshi Moriya, Daniel J. Peppe, Gregory E. Ravizza, Ursula Röhl, Jonathan D. Schueth, Julio Sepúlveda, Philip Sexton, Elizabeth Sibert, Kasia K. Śliwińska, Roger E. Summons, Ellen Thomas, Thomas Westerhold, Jessica H. Whiteside, Tatsuhiko Yamaguchi, James C. Zachos

correspondence to: pincelli.hull@yale.edu

This PDF file includes:

Other Supplementary Materials for this manuscript includes the following:

Materials and Methods

Sites and materials

Here we present highly resolved, multiproxy records from three ocean drilling localities: J-Anomaly Ridge, North Atlantic (Integrated Ocean Drilling Program [IODP] Site U1403), Shatsky Rise, North Pacific (Ocean Drilling Program [ODP] Site 1209, Deep Sea Drilling Program [DSDP] Site 577), and Walvis Ridge, South Atlantic (ODP Sites 1262 and 1267).

This is the first detailed study of Cretaceous-Paleogene (K/Pg) sediments from IODP Site U1403, which was drilled on the flank of the J-Anomaly Ridge in 2012 at 39°56.60′N, 51°48.20′W at a present water depth of 4,949 m (*45*). Shipboard scientists immediately recognized that the two K/Pg spanning holes (U1403A and U1403B) were remarkably complete, with an intact ejecta layer and all nannofossil biozones present (*62*). The results presented here include a highly resolved bulk carbonate stable isotope record sampled shipboard at a resolution varying from ~20 cm in the Danian, to 2 cm across the boundary, and ~10 cm in the Upper Cretaceous (Table S12). This bulk carbonate carbon and oxygen isotope record, spanning the last 2.5 million years of the Cretaceous and the first 3 million years of the Paleocene, is one of the longest highly resolved records of its kind across the K/Pg boundary (Fig. S17). Additional samples for complementary measurements (i.e., sedimentology, magnetostratigraphy, biostratigraphy, cyclostratigraphy, iridium measurements, faunal and organic geochemistry analyses) were sampled during the post-cruise sampling party and in subsequent sampling requests and are detailed below.

We also present new K/Pg records from two of the best studied deep-sea K/Pg boundary localities, Walvis Ridge and Shatsky Rise, while leveraging existing resources from these sites. Shatsky Rise sites include the well-studied ODP Site 1209 on the Shatsky Rise (*63, 64*) at 32°39.1001′N, 158°30.3560′W and 2,387 m current water depth and DSDP Site 577 at 32°26.5′N, 157°30.4′W and 2,685 m current water depth (*65*). Walvis Ridge sites include ODP Site 1262 at 27°11.15′S, 1°34.62′E and 4,759 m current water depth (*66*) and ODP Site 1267 at 28°5.89′S, 1°42.66′E and 4,355 m current water depth (*67*). ODP Sites from Shatsky Rise and Walvis Ridge have been used along with the deep-sea sediments outcropping in Zumaia, Spain, to develop and refine a complete astrochronological age model for the Paleocene and latest Cretaceous (*68-72*). With a biostratigraphically complete K/Pg boundary section, and a globally aligned cyclostratigraphic age model spanning from the very latest Cretaceous through the

Paleocene, ODP Site 1209 and the nearby ODP Sites 1210 and 1211 have been extensively studied across the boundary, with studies including a resolved benthic foraminiferal and, in the Cretaceous, bulk carbonate stable carbon and oxygen isotope records (*73-75*), community dynamics across the boundary in nannoplankton (*76-81*), foraminifera (*56, 82, 83*), and fish (*84*), productivity change (*85*), environmental change (*86, 87*), extinction drivers (*28*), and global compilations of boundary sections and dynamics (*5*). The new high-resolution records presented here include a resolved boundary record of bulk carbonate oxygen and carbon isotopes (shown in part in: *56*) (Table S11), complementary records of early Paleocene foraminiferal oxygen and carbon isotopes (Table S11), and a resolved earliest Danian record of nannoplankton community composition (Table S18). These new and existing records from ODP Site 1209 allow us to test the generality of patterns and explanations derived from Site U1403 records in the context of the much broader body of work from Shatsky Rise, including studies on the historic DSDP 577 holes (e.g., *48, 53, 65, 88-95*), at the same location. The same is true of Walvis Ridge. From Walvis Ridge we present a new resolved bulk isotope record (Tables S9) and weight percent coarse fraction record from ODP Site 1267 (Table S13), to test the generality of these existing resources from ODP Site 1262 (*96*), with the underlying records published here for the first time (Tables S10, S14).

The high-resolution records at J-Anomaly Ridge, Shatsky Rise, and Walvis Ridge are shown in Fig. 2. The data in this figure is provided in Tables S9-S15 and refs. (*42, 43, 56, 73-75, 96, 97*) using age models from refs. (*72, 98, 99*).

Together, these records (Figs. 2 and S18) are the most temporally resolved and finely sequenced records of the K/Pg boundary. They offer the opportunity to finely detail the temporal sequence of change in open ocean sites relatively far from the impactor: the central equatorial Pacific (ODP Site 1209, DSDP Site 577), the mid latitude North Atlantic (IODP Site U1403), and the Southeast Atlantic (ODP Sites 1262 and 1267). Distance from the impactor is an important criterion, because proximal sites in the Caribbean and in some locations along the eastern seaboard of North America are stratigraphically complex, and include some combination of the following: expanded ejecta deposits, tsunami deposits, mass wasting deposits, and hiatuses (*5, 100-106*). Part of the historic debate on the timing of boundary-related events in open marine sediments, and the possibility of multiple impacts or impacts asynchronous with the boundary, has arisen from studies that interpret the depositional history (in particular, the timing of

deposition) at proximal sites as if they reflected processes and rates typical of normal marine sedimentation (e.g., *107, 108, 109*). Thus, our study focuses on records from the relatively open ocean basins in the latest Cretaceous (the Atlantic and Pacific) that should capture the open-ocean response to the events of the K/Pg boundary.

Age model overview

Two main types of age models are used in this study: cyclostratigraphic age models and bio- and/or magnetostratigraphic age models. Data from the three high resolution localities (J-Anomaly Ridge: IODP Site U1403, Shatsky Rise; ODP Sites 1209 and 1210; and Walvis Ridge ODP Sites 1262 and 1267) are shown in the geologic time domain using cyclostratigraphic age models. For Site U1403 we combined a completed cyclostratigraphic age model for the Maastrichtian (*110*) with a new cyclostratigraphic age model for the Danian (detailed below). The Site U1403 age model uses a K/Pg boundary age of 66.022 Ma to be consistent with the boundary used by Dinarès-Turell et al. (2014) (*72*) in other cyclostratigraphic age models for this interval (*72, 74, 75, 98, 99*). This boundary age differs from the most recent radiometric ages for the K/Pg boundary of 66.016 ± 0.05 Ma (*8*) for U-Pb and 66.052 ± 0.008 Ma (*50*) for $^{40}Ar/^{39}Ar$, but falls within the uncertainties of those estimates (including systematic error). We use the existing cyclostratigraphic framework for the K/Pg boundary sections at Sites 1209, 1210, 1262, and 1267 from Dinarès-Turrell et al. (2014) (*72*), with its extension further into the Maastrichtian by Woelders et al. (2017) (*97*).

Geologic Time Scale (GTS) 2012, with a K/Pg boundary age of 66.04 Ma (*7*), forms the framework for the other age models used in this study and shown in the compilation in Figure 1. The data in Figure 1 are a compilation of temperature estimates from marine and terrestrial sites around the world (Fig. S1-S16), updated to a common timescale (primarily) by updating the bio- and magnetostratigraphic marker ages to match those of GTS 2012. In order to construct GTS 2012-compliant age models for all localities (detailed below and shown in Tables S2-S4), the records from Sites U1403, 1209, 1210, 1262, and 1267, which were on the Dinarès-Turell et al. (2014) (*72*) age model, were shifted to match the K/Pg boundary age in the global compilation.

As explained in the main text, new geochronological estimates for the age of the magnetochron C29r/C30n reversal are much closer to the K/Pg boundary (i.e., ~250-300 kyrs is indicated by the most recent $^{40}Ar/^{39}Ar$ and U-Pb geochronology (*8, 50*), and 358 kyr prior by

GTS 2012 (*7*)). As a result, we used the magnetochron C29r/C30n reversal as the starting point for our modeled Deccan trap outgassing, in the GTS 2012 age framework, to be able to directly compare our empirical data with the model scenarios. Even so, we find a ~50 kyr difference in the onset of late Maastrichtian warming in the empirical records and our models (Fig. 3). This offset suggests that this major phase of outgassing most likely began shortly after the C29r/C30n boundary at ~300 kyr (assuming GTS 2012 ages (*7*)) or ~215 kyr (assuming absolute ages (e.g., *8, 50*)) prior to the K/Pg boundary, rather than at the C29r/C30n boundary as modeled (*12, 50*).

Cyclostratigraphic age model for U1403

The Maastrichtian to Danian interval of Site U1403 was analyzed by XRF-scanning (X-Ray Fluorescence) in the MARUM XRF Core Scanner Lab in Bremen, Germany. The AVAATECH instrument, serial no.11, with an Oxford Instruments 100W Neptune Rh X-Ray tube and a Canberra X-PIPS Silicon Drift Detector (SDD, Model SXD 15C-150-500) was set to a step-size of 15 mm, a slit down-core of 10 mm, and a slit cross-core of 12 mm. A first run was applied with 10Kv, 1.0 mA, for 20 s, and a second run at 50 Kv, 0.2 mA, for 20 s. The data were processed with WIN AXIL batch software using a 10Kv_Cl-Rh model and a 50Kv model, respectively. Outliers as a result of an uneven core surface were removed. The Danian XRF record is presented in Supplemental Table S21 and complements the already published Maastrichtian record (*110*).

Two holes were drilled at IODP Site U1403: Holes U1403A and U1403B. A shipboard splice, subsequently updated by Batenburg et al. (*110*), was used to generate a common depth scale between these two holes (classically known as meters composite depth [mcd], but called CCSF [core composite depth below sea floor] at Site U1403). The K/Pg impact ejecta layer was not used as an anchor point in building the composite splice between these two holes. Because of the highly resolved sampling across the K/Pg boundary, this omission created numerous issues with regards to building an accurate relative stratigraphy of the event for the samples that were collected off the main splice in the boundary cores (342-U1403A-26X, 342-U1403B-28X) due to a 20 cm CCSF offset between the ejecta layer in the two holes on the CCSF scale. To address this problem in the relative depth scale and age model, we adjusted the splice to include the impact ejecta layer as the tie point between the boundary cores at the two sites. The secondary tie point linked the K/Pg boundary in Hole B (which is not in the splice) with 247.7 m rCCSF

(revised CCSF) in Hole A. We then recalculated the CCSFs for Hole B, Core 28 by a linear interpolation between the boundary and the neighboring splice tie points. Only the coarse fraction, fish teeth and iridium records contain samples that required this CCSF revision. The effect of this adjustment is shown in Table S22.

To obtain detailed age control for the Danian interval of U1403, we correlated the iron record and the sedimentary banding pattern to the existing cyclostratigraphic framework of Site 1209 (*72*). A direct cyclostratigraphic interpretation of the interval above the K/Pg at U1403 is hampered by the relatively short length of the record and the complex nature of orbitally forced sedimentation patterns directly following the K/Pg, which is documented in records worldwide (*72, 111*). A detailed comparison of Site U1403 to Site 1209 was made using the banding patterns in the core photographs and the Fe counts from XRF analysis (expressed as log Fe, Fig. S38), supported by variations in magnetic susceptibility (*112*). In addition, a bandpass filter was applied using AnalySeries (*113*) to the log Fe record, centered at 2.2 m with a bandwidth of 1.7 to 3.3 m (Fig. S38). The 2.2 m filter follows the oscillations of the log Fe record and the sedimentary banding patterns, with maxima in the bandpass filter coinciding with groups of dark bands, likely representing maxima in the 405-kyr cycle of eccentricity-modulated precession. An age model for the Danian of U1403 was constructed by assigning ages of long-eccentricity (405 kyr) maxima and minima in the La2011 eccentricity solution (*114*) to levels in U1403 corresponding to interpreted 405-kyr extremes in Site 1209 (*72*). An additional cyclostratigraphic investigation of Site 1209 (*111*) proposes the same number of interpreted long-eccentricity cycles post-K/Pg and a similar interpretation of the position of 405-kyr cycle extremes, except for the placement of the second 405-kyr maximum above the K/Pg boundary. The age model for the Danian of U1403 was combined with the Maastrichtian cyclostratigraphic age model (Table S23, Fig. S38). The resulting age model is broadly consistent with shipboard based nannofossil biostratigraphy in the Maastrichtian (*110*), updated Danian nannofossil biostratigraphy (Tables S24 & S25), and osmium isotope stratigraphy (see below).

The comparison of bulk isotope records from J-Anomaly Ridge, Shatsky Rise, and Walvis Ridge highlights the relative certainty in the age models for the three sites (Fig. 2). IODP Site U1403 on J-Anomaly Ridge is relatively poorly constrained in the uppermost Maastrichtian due to the lack of magnetostratigraphic control (see below), and changes in sedimentation rates within long eccentricity cycles. At ODP Site 1209, the uppermost Maastrichtian is disturbed by

drilling. These uncertainties and offsets are shown by differences in the timing of the peak $\delta^{18}O$ excursion in the Cretaceous portion of C29R. At Shatsky Rise, the minimum in $\delta^{18}O$ of benthic foraminifera appears to precede that at Walvis Ridge by ~87 kyrs, although this offset is primarily due to a single anomalously low $\delta^{18}O$ value at Shatsky Rise. In bulk isotope space, the minimum values at Walvis Ridge precede those at J-Anomaly Ridge by ~37 kyrs. In the early Danian, the agreement between the three sites generally seems better (Fig. 2), although slight differences in the relative timing of peaks and troughs in bulk carbonate $\delta^{18}O$ attest to the uncertainty in current time constraints, and provide a new tool for evaluating age models in this contested interval.

Bio- and Magnetostratigraphy at Site U1403

The construction of cyclostratigraphic age models depends on reliable indicators of geologic time such as geological boundaries (i.e., the impact markers used to align the boundary cores between U1403A and U1403B), biostratigraphically important datum levels, magnetochron boundaries, and chemostratigraphically important events. For Site U1403, nannofossil biostratigraphy, osmium isotope stratigraphy, and light stable isotope stratigraphy provided additional constraints for the construction and/or testing of the cyclostratigraphic age model.

Although the sedimentary weight percent carbonate at Site U1403 is typically above 50% in the upper Maastrichtian, the sediments are devoid of planktonic foraminifera –a common biostratigraphic marker. Calcareous nannoplankton, however, are abundant in the upper Maastrichtian and lower Danian and provided critical constraints on the Maastrichtian cyclostratigraphic age model (*45, 110*) (Figs. S39). With minor updates to the shipboard biostratigraphy (Tables S24 and S25), the nannofossil datums in the Danian are generally consistent with the cyclostratigraphic age model (Figs. S38). Other taxa were not well-enough preserved to be of use in biostratigraphy. Silica was not well preserved in sediments deposited during this time period (*45*), and radiolarian datums were not provided or used in shipboard age models for sediments older than ~63 Ma. Organic matter preservation was similarly poor, so dinocyst and palynomorph zonation were not possible (Table S26).

Shipboard pass-through magnetometry during Expedition 342 failed to collect reliable magnetochron data for the upper Maastrichtian through lower Paleocene of Site U1403. Discrete,

high-resolution paleomagnetic samples were collected during the post-cruise sampling party in order to attempt to identify the highly important magnetochron spanning the K/Pg boundary (magnetochron C29R). Seventy-two discrete samples were taken in XCB cores from the splice between U1403A-25X, 1-124cm (233.97 m ccsf) and U1403B-30X2, 84cm (271.09 m ccsf). Samples were obtained at a resolution of ~0.30 m (excepting a disturbed interval around 254 m ccsf) from the split core sections by pressing 7 cm^3 plastic cubes into the sediment in the least disturbed, central region of the core. All magnetic measurements were performed at CEREGE (Aix-en-Provence, France) using a SQUID cryogenic magnetometer (2G Enterprises, model 755R, with noise level of $10^{-11}Am^2$) with an attached automatic alternating field 3-axis degausser system (maximum peak field 170 mT) placed in a magnetically shielded room (field of ~250 nT). The natural remanent magnetization (NRM) was measured and samples were demagnetized using a step-wise alternating field (AF) up to 60 mT. All discrete sample data were volume corrected (7 cm^3). Data visualization and analysis were realized using Paleomac software (*115*) and correlated to the geomagnetic polarity timescale (GPTS 2012) (*7, 116*).

A small overprint (< 10-15 mT), possibly due to viscous remanent magnetization (VRM) or an isothermal remanent magnetization (IRM), was removed by using a progressive alternating field to isolate only one component of magnetization (or Characteristic Remanent Magnetization, ChRM). For 42 samples, a normal or reverse polarity could be attributed using the direction of the ChRM because of their unequivocal behavior. For 13 samples, a polarity was tentatively assigned, although some caution should be taken because of their behavior upon AF treatment (large alpha95 and/or low intensity). The 17 remaining samples were excluded from the final interpretation because of their ambiguous or erratic behavior upon AF treatment (alpha 95>20). Using the ChRM inclinations allowed us to define 7 magnetozones (Fig. S40).

Paleomagnetic data from the discrete analyses unfortunately failed to provide additional time constraint around the K/Pg boundary. Overall, the polarity sequence appears sound for the Paleogene magnetochrons C27R to C29N, where a continuous normal and reverse polarity stratigraphy was established. However, magnetochron C29R, the short magnetic subchron bracketing the K/Pg boundary and spanning most of the Deccan trap eruptions (*12, 13*), could not be defined due to unclear paleomagnetic results (Table S27, Fig. S40). Similar issues (lower NRM intensities, possibly disturbed sediments) continued in the Cretaceous portion of the cores, where chrons C30N and C30R were only tentatively attributed.

Osmium isotope geochemistry

Osmium isotope chemostratigraphy provides a useful geochronometer around the K/Pg boundary because of two globally recognized features in the osmium isotope record: a drop of ~0.13 $^{187}Os/^{188}Os$ beginning around the C30N/C29R magnetochron boundary, and a drop of ~0.25 $^{187}Os/^{188}Os$ coincident with the K/Pg boundary iridium anomaly (*6, 46, 117*). These two osmium isotope events are attributed to the onset of Deccan volcanism and the extraterrestrial impact, respectively, as discussed in the literature (e.g., *6, 46, 117, 118*).

An osmium isotope record spanning the uppermost Cretaceous through lowermost Paleocene was generated for IODP Site U1403 on the leachable osmium following the method of Ravizza (*119*) (Fig. S20). Leached osmium (from clays) was favored over the bulk digest methods (e.g., *46*) to minimize contamination from the abundant detrital components. This choice, combined with the low Os content, a blank correction of 0.02-0.03, and an unquantified Re contribution, means that the Site U1403 record presented here (Fig. S21, Table S16) can be interpreted in terms of the relative shape of the osmium profile, but likely does not accurately capture the absolute values, although the measured values are similar to those obtained from other sites (Fig. S21a). The large uncertainty ($\approx \pm 2.5\%$) in $^{187}Os/^{188}Os$ compared to previously reported Os isotope records is mainly the result of the low concentration of leachable Os in these samples, and the associated correction for procedural blanks, which can reach up to 10% of total analyte.

The osmium record at IODP Site U1403 is very similar to K/Pg boundary records from Bottacione Gorge, Shatsky Rise, Walvis Ridge, and Maud Rise (Fig. S21). Namely, osmium isotope ratios decline in the Upper Cretaceous, plateau during magnetochron C29R, and then drop again across the K/Pg boundary, before settling into a lower Paleocene baseline than in the Cretaceous. Unfortunately, IODP Site U1403, like the Walvis Ridge record, does not show a stable Cretaceous baseline or abrupt transition to declining osmium values coincident with the C30N/C29R boundary as in the 'classic' records of Bottacione Gorge and Shatsky Rise (*46, 117*). This means that osmium at Site U1403, like the magnetochron boundary, provides a poor time constraint. Even so, the current cyclostratigraphic age model extends the relative duration of the Upper Cretaceous plateau in osmium (highlighted in green in Fig. S21b) as compared to other sites. This pattern would suggest that the current age model overestimates the amount of time in the upper Cretaceous interval.

Iridium geochemistry

Iridium was measured across the U1403 K/Pg boundary using laser-ablation inductively coupled plasma–mass spectrometry as described and published in Loroch et al. 2016 (*120*).

Oxygen and carbon isotope geochemistry

We generated resolved and temporally expanded records of stable carbon and oxygen isotopes to consider the relative role of Deccan volcanism and impact in marine extinctions. This section discusses the methods used to collect new stable isotope data (carbon and oxygen) from carbonates at IODP Site U1403 and ODP Sites 1209, 1262 and 1267. We discuss published stable isotope records (shown in Fig. 1) in the section 'Temperature proxy compilation' below, including new $\delta^{18}O$ records from stable carbon isotope data published for Sites 1210, 1262, 1267, and 465 (i.e., records in Tables S5-S9)(*28*).

For IODP Site U1403 we generated a high resolution, ~5 myr long record of bulk carbonate stable carbon and oxygen isotopes comprising 646 measurements across four laboratories (Table S12). The Maastrichtian bulk samples from Site U1403 were analyzed at the Goethe-University Frankfurt (Germany) using a Finnigan MAT 253 coupled online to a Gasbench II or at Kanazawa-University (Japan) using a Finnigan Delta V Advantage coupled with Gasbench II (for details see (*121*)) and were published in Batenburg et al. 2017 (*110*). K/Pg boundary samples were analyzed at the Yale Analytical and Stable Isotope Center using a Thermo DeltaPlus XP and Paleocene samples were analyzed at the Friedrich-Alexander Universität Erlangen-Nürnberg with a Gasbench II connected to a ThermoFinnigan Five Plus mass spectrometer. All isotope values are reported in ‰ relative to the Vienna Peedee belemnite standard (VPDB). For all systems used, the analytical precision of replicates of standard measurements is better than 0.06 and 0.08 ‰ for carbon and oxygen, respectively. At Yale, weight percent carbonate (Table S19) was calculated by the deviation of the measured signal intensity from that predicted for a pure carbonate of the same mass, as determined by in-house standards. These weight percent carbonate measurements were combined with shipboard measurements of weight percent carbonate (*45*), to calculate a weight % carbonate record (shown in Fig. 2) derived from XRF measurements of Ca and Fe (Table S20). The sedimentary weight % coarse fraction (i.e., the mass proportion of the sample greater than 38 μm in size) was

determined for Site U1403 (as shown in Fig. 2) during sample preparation at Yale University (Table S15).

For ODP Site 1209, four new stable isotope records are presented in Table S11 for bulk carbonate, bulk foraminifera, the planktonic foraminifera genera *Praemurica* and *Woodringina*. Each are described below. The bulk carbonate record from ODP Site 1209 was generated with a Thermo-Finnigan MAT 253 mass spectrometer coupled to a Kiel Device at the University of California Santa Cruz, with analytical precision (1σ) of ± 0.05 ‰ for $\delta^{13}C$ and ± 0.08 ‰ for $\delta^{18}O$ based on repeated analyses of in-house standards. The boundary portion of this record was published in part previously in (*56*), but the data are provided here for the first time. To isolate the potential cause of the high amplitude $\delta^{18}O$ dynamics in the bulk carbonate in the lower Paleocene, we generated a novel type of 'bulk' record: bulk foraminifera. Bulk foraminifera were analyzed as a homogenized 38-125 μm size fraction, a size fraction dominated by immature and microperforate planktonic foraminifera (*56, 122*). For the same time interval (the lowermost Paleocene) we also analyzed *Woodringina* and an evolutionary series of *Praemurica* species. The bulk foraminifera and *Woodringina* records were analyzed at the MARUM (the Center for Marine Environmental Sciences) at the Universität Bremen on a Thermo-Finnigan MAT 251 mass spectrometer coupled to a Kiel Device. The MARUM lab analytical precision (1σ) for carbonate mass spectrometry is ± 0.05 ‰ for $\delta^{13}C$ and ± 0.07 ‰ for $\delta^{18}O$, based on replicate analysis of in-house and international standards. The *Praemurica* series was generated at the Scripps Institution of Oceanography using a Caroussel-48 automatic carbonate preparation device and a common acid bath (i.e., a Fairbanks device) coupled to a Finnigan MAT 252 mass spectrometer, with an analytical precision (1σ) of ± 0.04 ‰ for $\delta^{13}C$ and ± 0.09‰ for $\delta^{18}O$, respectively.

Organic geochemistry

The targeted analysis of aliphatic hydrocarbons in selected samples from Site 1403 across the K/Pg boundary provides qualitative information about the sources and preservation of organic matter in these sediments. Most algal steranes and bacterial hopanes were present below the limit of detection, whereas the signal of detected biomarkers was close to, or slightly above laboratory blanks and background contamination. This observation is consistent with the overall low total organic carbon (TOC%) of samples near the K/Pg boundary (0-0.3%;(*45*)). Thermal

maturity indices based on the stereochemistry of algal steranes and bacterial hopanes indicate a degree of thermal alteration between early and peak oil window (Table S29). However, the elevated degree of thermal maturity obtained from biomarkers is inconsistent with the low thermal alteration inferred from the burial history of the Newfoundland sediment drifts. Indeed, older, organic-rich sediments across the Cenomanian-Turonian boundary at Site U1407 contain organic matter that is thermally immature and relatively well preserved, as shown by high hydrogen indices and low T_{max} values (*62*). Given the low TOC% near the K/Pg boundary, it is likely that the prevalent organic matter preserved in these sediments is dominated by previously fossilized, thermally mature, allochthonous organic matter derived from the erosion of source rocks on the continent, similar to previous reports across the K/Pg in Stevns Klint, Denmark (*123*) and in Quaternary sediments (*124*). Furthermore, although we did not measure the functionalized precursors of steranes and hopanes, our results are consistent with the lack of functionalized lipids such as archaeal glycerol dialkyl glycerol tetraethers (GDGTs), in the same samples. Thus, given the low abundance of hydrocarbon biomarkers across the K/Pg boundary at Site U1403, and because of their non-indigenous source, they are not reliable indicators of changes in biological sources and environmental conditions in the overlying water column.

Lipid Extraction and Analysis: Metal tools were rinsed with organic solvents, and all glassware, aluminum foil, silica, quartz wool and quartz sand were combusted at 500ºC for 12 hours to remove any organic contamination. About 5-10 g of powdered sample was extracted with a Dionex ASE 250 using DCM:MeOH (9:1 v/v). 100 ng of d4 C_{29} ααα (20R)-ethylcholestane was added as an internal standard before extraction. Elemental sulfur was removed using acid-activated copper powder for 12 hours. Asphaltenes were removed (3x) by precipitation in 10-40 ml of hexane at ~4ºC overnight, following centrifugation at 2500 rpm for 30 min. Aliphatic hydrocarbons were separated from the maltene fraction on a silica gel column using *n*-hexane (3/8 dead volume). Samples were analyzed by gas chromatography – mass spectrometry in full scan and metastable reaction monitoring (GC–MRM–MS) modes on a Micromass AutoSpec Ultima mass spectrometer interfaced to an Agilent 6890 N gas chromatograph at the Massachusetts Institute of Technology as described in (*125*). MRM-MS is a sensitive analytical technique that provides an elevated signal to noise ratio for the identification of compounds that are normally unresolved, co-eluting, or present in very low abundance.

Temperature proxy compilation

In order to assess the similarity of the LOSCAR model run temperatures with global temperature change across the K/Pg boundary, we compiled relatively resolved records of temperature across this time interval and updated the temperature calculations and age models as needed. Although our compilation represents the most comprehensive database (Table S4) of temperature estimates across the K/Pg boundary, and allows us to examine the relative similarity of temperature dynamics across sites and proxy types, it does not include every published temperature record for the Maastrichtian and Paleocene, nor does it attempt to estimate a global-absolute temperature through this interval. We choose to include records with relatively high temporal resolution in order to assess a relative temperature change across the K/Pg boundary. Temperature records from a small portion of the compilation time frame (i.e., only the Paleocene) were not included because we were not able to calculate a temperature relative to the latest Cretaceous in such instances. So while there are more published paleotemperature proxy records around this time (e.g., *126, 127*), they were excluded if they lacked the temporal resolution around the boundary needed to express them in this way with confidence. Furthermore, our compilation and analyses are based on relative temperature changes because our focus is on understanding relative change in temperatures through time. The use of absolute temperatures from sites with different starting temperatures would obscure the detection of changes in temperatures (i.e., 2-4°C warming is less than the differences in temperature expected with latitude, across the marine/terrestrial divide, and among proxy types). Thus, temperature change within each dataset was calculated relative to the latest Cretaceous values, rather than as the mean of a time frame, in order to minimize the effect of sparse or changing sampling densities across intervals of interest. Finally, temperature change through time for all combined proxy data is estimated using a 60-pt fast Fourier transform smoother across all datasets. With aligned age models and updated temperature estimates, as needed, this compilation serves as a starting point for future work on global temperature dynamics across the K/Pg boundary.

Data and transformations include:

- **Benthic foraminiferal $\delta^{18}O$** measurements from Shatsky Rise ((*73, 90*), and this study: Table S5), Hess Rise in the low-latitude Pacific (this study: Table S7), Walvis Ridge in the mid-latitude Southeast Atlantic ((*44, 128*), and this study: Tables S6 and S8), Maud Rise in the high-latitude South Atlantic (*129*), and Blake Nose (*130*), J-Anomaly Ridge (*131*), and Bass River (*132*) in the Northwest Atlantic, New Jersey margin. For details of the revised age models used for each site, see Tables S2-S4. Temperatures were calculated via the equation of ref. (*133*) with species offsets, where necessary, taken from ref. (*134*), after (*73*). For these calculations, we assume an ice-free mean ocean seawater value of -1.2 ‰. Here we consider relative changes in temperature rather than absolute values, thus the assumptions should have a minimal biasing effect on data interpretation.
- **Planktonic foraminiferal $\delta^{18}O$** measurements from Walvis Ridge in the mid-latitude Southeast Atlantic (*44, 49*), Maud Rise in the high-latitude South Atlantic (*135, 136*), and Blake Nose (*130*) and Bass River (*132*) in the North Atlantic. For details of age models, see Tables S2-S4. As with benthic foraminiferal data, we use the $\delta^{18}O$-temperature calibration from ref. (*133*), assuming ice free conditions.
- **Palaeosol carbonate $\delta^{18}O$** measurements from continental USA (*137, 138*). We use ref. (*138*) option 2 for calculated temperatures, as preferred by the original authors. Sample ages are assigned according to the comprehensive new age model for this formation derived from biostratigraphy, magnetostratigraphy and geochronology from ref. (*139*).
- **Bivalve and gastropod carbonate $\delta^{18}O$** measurements from Seymour Island, Antarctica (*140*), omitting those samples with evident trace metal contamination indicated by Sr, Mn and Fe concentrations. Data shown are averages of several measurements for each time interval. Ages are assigned based on linear interpolation between magnetochron boundaries (*140*), updated to GTS 2012 (*7*).
- **Clumped isotope** measurements from bivalves from Hell Creek, USA (*141*) and brachiopods from Seymour Island, Antarctica (*142*). Note that we binned clumped isotope data as in the original studies, and omitted those samples with evident trace metal contamination as indicated by Sr, Mn and Fe concentrations. We also omitted gastropod and carbonate vein measurements from ref. (*141*), as they display signs of diagenetic alteration/thermal resetting. Age models for Hell Creek and Seymour Island data are

based on linear interpolation between magnetostratigraphic reversals from refs. (*140, 143*).

- **TEX_{86}** measurements from the New Jersey Margin (*144*) and Brazos River (*24*) in the USA, and Bajada del Jagüel, Argentina (*97*). Data points flagged as displaying high BIT index (> 0.3) were omitted. Age models for New Jersey and Brazos River were constructed using dinoflagellate biostratigraphic datums (*24, 144*). For Bajada del Jagüel ages are as published (*97*). At Bass River (*145*), ages are assigned according to the age model of ref. (*132*)
- **Leaf Margin analyses** from the Williston Basin, continental USA (*136, 146-150*). Where necessary, temperatures were recalculated using the temperature calibration and uncertainty model of ref. (*151*). Age models for these floras are based on magnetostratigraphic tie points (*152*) with ages reassigned according to GTS 2012 (*7*).
- **Mg/Ca temperatures** from Bass River, New Jersey Margin (*97*). Temperatures are as calculated by the original authors, omitting those from the bioturbated interval around the K/Pg boundary. Ages are assigned according to the age model in ref. (*132*).

In addition, in a few cases not all data provided in a given study was included in the compilation here because issues like very poor preservation, reworking, or a lack of stratigraphic control affected just a part of the record. However, it should be noted that these exclusions have no visible effect on the estimates of global temperature change. For example, in the case of Bass River (*97*), the uppermost 15cm of the Maastrichtian is heavily bioturbated (*153*). For this reason we do not include Mg/Ca or $\delta^{18}O$ data from that interval in our composite, following (*97*). In addition, Woelders et al.'s earliest TEX_{86} data point (at 18 cm below the K/Pg boundary) is anomalously high, which could be the result of sediment mixing, so we also exclude this data point from our compilation.

We also omit some New Jersey Margin data from ref. (*132*). Specifically, we do not plot the anomalously light data from the indurated or heavily reworked sections at Bass River at and above the K/Pg boundary. In addition, we do not plot data from the shallower Ancora hole from the same study, where the uppermost Maastrichtian cooling seen elsewhere on the New Jersey margin appears to be missing. This, we suggest, may be the result of a fall in sea level of ~50 m in the very latest Maastrichtian part of C29r, as indicated by benthic foraminiferal assemblages

and planktic:benthic foraminiferal ratios (*153-155*) at the downslope Bass River site. Prior to this sea level fall the estimated water depth at Ancora was ~45m (*132*), so it is likely that such a sizeable sea level change would have exposed Ancora to erosion, especially since rip-up clasts at many New Jersey margin sites at this time suggest the area may have been subject to tsunami or megastorm events (*153*). The absence of a discrete spherule bed at Ancora despite its presence at Bass River downslope (*154*) supports this interpretation.

Finally, as discussed in the main text, two proxy types (fish teeth $\delta^{18}O$ and bulk carbonate $\delta^{18}O$) record dynamics unique to that proxy type for reasons that we suspect are due to biological responses of the living organisms in the early Paleocene Ocean (Fig. S10c, S11, S12). Thus they are excluded from the global temperature compilation. In the case of the $\delta^{18}O$ of fish teeth, this proxy alone (from a single site) indicates an average warming of up to 4-5°C during the first 100,000 years of the early Paleocene as compared to background values of the uppermost Cretaceous (Fig. S10c). This would be an extraordinarily large and prolonged warming event, which would be improbable to miss in other proxies, especially given the exceptional preservation of carbonate in the lowermost Paleocene (*41*). Its magnitude would be similar to that of the largest known global warming event of the Cenozoic, the Paleocene Eocene Thermal Maximum, which is readily detected across a range of temperature proxies and sites (e.g., *156*). In addition, faunal analysis of dinoflagellates from the very same locality suggest the occurrence of cold-water taxa multiple times over the same interval (*157*), contradicting the fish tooth $\delta^{18}O$ signal. However, the dinoflagellate signal might also reflect biology (high-latitude origins) more than temperature. Thus, we suspect that fish, on average, shifted their depth habitat shallower in the earliest Paleocene in response to changing environmental conditions. There is also a change in the dominant fish tooth types making up ichthyolith debris in open ocean sites across the K/Pg boundary (*158*), and a wholesale turnover in near coastal taxa (*159, 160*), thus the new dominant taxa may have simply occupied a different depth habitat than the former dominants.

Similarly, bulk carbonate records show unique dynamics (i.e., high amplitude oscillations in $\delta^{18}O$; Figs. S11-S12) during an interval with large amplitude oscillations in the nannoplankton species comprising the majority of deep-sea carbonate oozes (e.g., Figs. 5, S34-S35). Although bulk carbonate $\delta^{18}O$ oscillations are coherent across sites (Figs. 2, S11-S12), they generally correspond to turnover in the dominant nannoplankton taxa present (Figs. 5, S34-S35) and do not match temperature dynamics in any other temperature proxy (Figs. S1-S16). This, and the

conflict with stable $\delta^{18}O$ values in planktonic foraminifera from the same time period and locations (including species-specific records and bulk foraminiferal records, Figs. 5, S34-S35), further suggests that bulk carbonate is not a reliable temperature proxy at this time. We suspect the dynamics seen in the bulk carbonate $\delta^{18}O$ reflects the changing taxonomic composition of the carbonate ooze (although it is perplexing to see the oscillations more strongly expressed in $\delta^{18}O$ than in $\delta^{13}C$), rather than a temperature signal. For these reasons, both fish teeth and bulk carbonate $\delta^{18}O$ values were excluded from estimates of global temperature change in our study.

Four records are provided here for the first time as part of this global compilation: benthic foraminiferal $\delta^{18}O$ records from ODP Site 1210 (Table S5), ODP Site 1262 (Table S6), DSDP Site 465 (Table S7), and benthic foraminiferal and bulk carbonate $\delta^{13}C$ and $\delta^{18}O$ records from ODP Site 1267 (Table S8). The corresponding carbon isotope records from the first three sites (Tables S5-S7) were published in Alegret et al. (*28*). The data from ODP Site 1267 is published here for the first time, and was generated at the University of California Santa Cruz, after (*28*). This record (also shown in Fig. S1c) is expanded across the very lowermost Danian, as is also apparent from XRF core scanning comparisons of ODP Site 1267 vs. 1262 in (*68*).

LOSCAR earth system modeling

We use the LOSCAR (Long-term Ocean-Sediment CArbon Reservoir, v 2.0.4 (*47*)) carbon cycle model to investigate the range of pCO_2 change caused by several possible scenarios of Deccan volcanic degassing of carbon and sulfur volatiles, in combination with pelagic calcifier extinction and organic carbon export reduction at the K/Pg boundary.

The Paleogene configuration of LOSCAR featuring a Tethys ocean basin (*47*) was employed, incorporating the modifications in (*41*) and described briefly below. Equilibrium constants for carbonate chemistry calculations were determined for K/Pg seawater $[Mg^{2+}]$ and $[Ca^{2+}]$ using Hain et al's MyAMI-based corrections (*161*). A $[Mg^{2+}]$ of 42 mmol/kg and $[Ca^{2+}]$ of 21 mmol/kg were used for all simulations. Seafloor bathymetry was more finely subdivided into 100 m depth intervals, rather than the standard 500 m interval. The exponential constant (n_{Si}) used in the silicate weathering feedback equation (after *162*) was 0.6 in all simulations, which is the strongest weathering feedback considered by Uchikawa and Zeebe (*163*). We used this strong silicate weathering feedback to reflect the presence of easily-weathered Deccan basalt exposure

at low latitudes during our interval of interest. A pre-event baseline pCO_2 of 600 ppm was used after (*41*).

SO_2 degassed from Deccan volcanism, and the Chicxulub impact, is assumed to be converted to sulfuric acid (H_2SO_4) in the atmosphere and subsequently rain out onto the Earth's surface (*38*). The portion falling into seawater would have rapidly dissociated to sulfate anion (SO_4^{2-}). This addition of an anionic salt reduces the negative charge deficit of the conservative salts (i.e., total alkalinity [TA]). Since neither sulfur nor sulfate is a tracer in LOSCAR, we simulate the acidification of the oceans through sulfate addition by prescribing an equivalent reduction in total alkalinity (TA, which is a tracer in LOSCAR) as 2 mol TA for every mol S emitted, as sulfate is a divalent anion. This TA reduction is applied to the surface ocean reservoirs only but is subsequently mixed throughout the ocean due to vertical mixing and thermohaline circulation in LOSCAR. A similar approach was taken by Tyrrell et al. (*22*) when modelling the influx of bolide-derived SO_2 release at the K/Pg boundary.

Three aspects of the LOSCAR modeling were poorly constrained by the available empirical data (biological change, outgassing volume, climate sensitivity), and we addressed this uncertainty by modeling a range of scenarios for each issue. We discuss each aspect below.

In order to include the biological effects on the marine carbon cycle of the mass extinction of many marine taxa and most marine pelagic calcifiers at the K/Pg boundary, we had to specify a percentage change in the export of organic carbon and of carbonate from the surface to deep ocean and in the rate of organic matter recycling in the water column. The K/Pg mass extinction affected all three aspects of the marine carbon cycle (i.e., *164*), but the amount and duration of change in each continues to be an area of active research (*28, 49, 85, 132*). As a result, we decided to explore the effects of varying each of these parameters for each volcanic emission scenario on observed changes in temperature, the surface-to-deep $\delta^{13}C$ gradient, and carbonate saturation state in the ocean. During the exploration of varying combinations of biological change, we assumed a climate sensitivity of 3°C/doubling (consistent with early Paleogene proxy estimates, as in *165*), a high Deccan trap total outgassing volume (9545 Gt C, 8500 Gt S), and an immediate gradual taper back to pre-event conditions over 1.77 Myr beginning in the earliest Paleocene.

We began our parameter exploration focusing on Case 1 outgassing (Leading: 87% prior to impact) and exploring a range of changes in pelagic organic carbon export (50-70% decrease)

and carbonate export (15-25% increase in the ratio of $CaCO_3$:C_{org}, resulting in a 35-65% reduction in pelagic $CaCO_3$ export flux) (Fig. S22). These were coupled to an increase in shallow water remineralization (the fraction of organic carbon export that is remineralized in the intermediate ocean reservoirs rather than the deep) from 78% prior to the K/Pg impact to 95% following the K/Pg impact. A parameterization of -50% C_{org}, +15% $CaCO_3$:C_{org} rain ratio (i.e., a 42.5% reduction in total carbonate export), with 95% shallow water remineralization post-impact produced early temperatures similar to empirical records (Figs. 3, S22). This combination had relatively modest effects on the carbonate saturation state of the deep ocean (Fig. S22), but it failed to fully collapse the $\delta^{13}C$ gradients between the surface and deep waters, as is observed in empirical records (Fig. 2), even when accounting for biological change (*49*). Notably, variation in remineralization rate had a relatively minimal effect on CO_2, although more remineralization did help decrease the $\delta^{13}C$ gradient and a 95% post-K/Pg remineralization rate was used in all subsequent simulations (Fig. S23). With this parameter exploration in hand (Fig. S22-S23), we choose a Case 1 (Leading) biological parameterization -50% C_{org}, +15% $CaCO_3$:C_{org} rain ratio) with 95% shallow remineralization (Fig. 3).

All Deccan Trap outgassing scenarios explored here (Fig. 3) assumed an additional K/Pg boundary impact degassing of 325 Gt S and 425 Gt CO_2 (*17*). We explored whether this impact degassing accounted for the small boundary spike in atmospheric pCO_2 in our models by running our favored Case 1 biological scenario with and without impact degassing (Fig. S24). Due to its very small volume, impact degassing has an almost negligible effect on atmospheric CO_2 concentrations, and the most significant boundary feature in all our models is a result of the instantaneous collapse of the biological pump (similar to Beerling et al. (*166*)). One boundary phenomenon not included in our modeling is the loss and regrowth of the terrestrial biosphere (*167*). Estimates for the duration of this vary, but are on the scale of several thousand years to 10,000 years (*167, 168*). The short-end estimates of terrestrial biomass loss and regrowth are very short relative to our model duration and time step, and the resolving power of most of our empirical records, and would have to be removed from the model in few time steps after being introduced. As a result, the very rapid loss and regrowth of the terrestrial biosphere was excluded from our simulations to avoid model integration issues. A second phenomenon not included in our modelling is the potential for dissociation of gas hydrates (*169, 170*) as a result of the continental shelf slope failure (*100-102*) because carbon emission estimates are relatively small

(300-1300 GtC (*169*)). At the lower-end estimate, these emissions match that of the boundary impact degassing, which had no discernable effect on model behavior (Fig. S24). At the upper-end, they would effectively increase the post-impact CO_2 release in a Case 2-like scenario by 25-60%, which should result in visibly elevated temperatures given the short time scale of release. This is not generally observed in the empirical temperature estimates (Fig. 1). Therefore, we considered the lower-end estimates for methane hydrate release as more likely (i.e., ~300 GtC) and did not include this factor in the modeled scenarios, which were evaluated primarily on the global temperature change record in Fig. 3.

A shortcoming of this series of LOSCAR model simulations (Fig. S22-S32) is that none of the simulations fully collapse the surface to deep carbon isotope gradient without oversaturating carbonates throughout the water column (i.e., see 70% C_{org} reduction scenario in Fig. S22). This could reflect the low vertical spatial resolution of the model (i.e., similar model parameters do collapse carbon isotope gradients in cGENIE), but even a small contribution of dissociated methane hydrates could fully collapse the carbon isotope gradient in LOSCAR (*169*).

Because we use a global temperature compilation as our primary test to distinguish amongst Cases 1-5, we explore the effect of the extreme ends of Deccan trap outgassing scenarios (4090-9545 Gt C and 3200-8500 Gt S (*10, 12, 40*)) and climate sensitivity from 2°C/doubling to 4°C/doubling, with 3°C/doubling consistent with early Paleogene proxy estimates (*165*) (Fig. S25). Note that the carbon degassing estimated by (*10*), is much greater than that indicated by(*39, 171*). The temperature range for Case 1 under differing combinations of total outgassing volume and climate sensitivity in Fig. S25 is the same as that shown in Fig. 1.

For Case 2 (50/50), we began the biological parameter exploration around the best Case 1 outgassing scenario exploring a range of C_{org} change (-25 to -60%) and $CaCO_3$:C_{org} rain ratio change (no change up to +40%) (Fig. S26). The best scenario was identical to our Case 1 exploration: -50% C_{org}, +15% $CaCO_3$:C_{org} rain ratio, with 95% shallow water remineralization. As in Case 1, we then explored the effect of the extreme ends of Deccan trap outgassing estimates and climate sensitivity on this scenario (Fig. S28), with the temperature range in Fig. S28 for Case 2 the same as in Fig. 1. For Case 3-5, we simply used the best-case biological scenario from Case 1 and 2 and explored the effect of changing outgassing and climate sensitivity in Figs. S29 and S30 respectively.

To simplify the model exploration and minimize the danger of overfitting, we assumed the same time scale of biological change for all modeled scenarios: an instantaneous biological change at the K/Pg boundary tapering back to the pre-extinction levels of organic carbon and inorganic export (and rates of remineralization) over the subsequent 1.77 Myr. There are multiple possible timescales indicated by the empirical records, including i) a ~400 kyr low followed by a ~400 kyr taper back to pre-event levels based on the duration of the peak abundance of the coarse fraction (i.e., planktonic foraminifera fraction) and subsequent recovery, as in (*56*) (Fig. 2); or ii) a ~800 kyr to million year recovery similar to changes in the relative deposition rates of nannoplankton (Fig. 2); or iii) several million years similar to carbonate deposition rates (*68, 164*), or iv) 1.77 million years based on the most recent estimate for the timing of biological pump recovery (*49*). To choose among these scenarios, we simulated multiple recovery scenarios and timescales (Fig. S27), and found that a protracted recovery of the biological pump, combined with an instantaneous onset of the biological recovery, led to temperature changes most consistent with the empirical records (Fig. 3).

LOSCAR Modelling and the Schoene et al Timing of Deccan Trap Emplacement

The Schoene et al. (*8*) emplacement scenario (i.e., Case 3) is similar to the 50/50 Case 2 scenario, in that there are roughly equal volumes of lava emplaced prior to and following the K/Pg impact, but differs from traditional hypotheses regarding the timing of emplacement. Namely Schoene et al. (*8*) show that the highest pre-impact emplacement occurred just 20-60 kyrs prior to the impact and that most post-impact emplacement occurred within several hundred thousand years of the K/Pg boundary. They hypothesize that this emplacement coincided with the degassing (and environmental impacts) of the Deccan volcanism. As Schoene et al. (*8*) recognized, this scenario results in appreciable warming of 2°C (Fig. S31) without a commensurate increase in terrestrial weathering, and this warming does not appear in any of the compiled temperature records (Figs. S1-S16). In addition, it leaves far too little CO_2 to drive the Late Cretaceous warming event of 2°C given current estimates of total outgassing (Fig. S31). Increasing total outgassing would solve this issue, but it would result in an even greater estimated temperature change just prior to impact. Increasing terrestrial weathering in-step with volcanic degassing and emplacement would negate the warming effect of Deccan volcanism (Fig. S32) as hypothesized by (*8*), but should be detectable in a negative carbon isotope

excursion in the surface and deep ocean just prior to impact, which is not observed (Fig. S32 vs. Fig. 2). In addition, the amount of weathering increase needed to offset the Schoene et al. warming signal is dramatic. Such an increase in weathering would result in a pronounced global cooling if applied to Case 1 and 2 (Figs. S41-S42) and was so impactful that we were unable to generate LOSCAR results for the low outgassing Case 2 scenario because the weathering pulled all the CO_2 from the atmosphere (Fig. S42).

One line of evidence Schoene et al. point to for the plausibility of greatly increased weathering in the latest Cretaceous prior to impact is the decline in osmium isotopes just prior the boundary (*8*). Although this decline in osmium isotopes has classically been attributed to the impact, with downcore smearing due to bioturbation, Schoene et al. postulated it could reflect increased weathering in-step with very latest Cretaceous Deccan Trap volcanism (*8*). We find this explanation unlikely. The negative $^{187}Os/^{188}Os$ excursion which spans the K-Pg boundary is mirrored by Ir enrichment (*6, 46*), a coincidence that is best explained by a common origin for the two signatures, and one that has also been documented in association with Popigai impact in the Late Eocene (*118*). If the osmium isotope decline began prior to the impact (and iridium emplacement), then the osmium isotope decline should appear to extend further back into the Cretaceous than the iridium anomaly, given that both are affected by sediment mixing (*172*), but this is not observed (*46*). In short, although we find the Case 2 scenario plausible (Figs. 3-4), but we do not find the timing or mechanisms proposed by Schoene et al. (i.e., Case 3) to be feasible given the data explored here.

Biological change quantification

We considered the relationship between Deccan volcanism and impact, and the ecology and evolution of marine species in one of three primary ways: i) indirectly through tracers of the carbon cycle (i.e., $\delta^{13}C$, carbonate deposition, carbonate preservation, etc.) at Sites U1403 and 1209; ii) directly through microfossil records at Sites U1403 and 1209; and iii) directly through a literature search of biological dynamics from the latest Cretaceous through earliest Paleocene (Table S1). Here we discuss the collection of new microfossil records from IODP Site U1403 and ODP Site 1209.

Sedimentary preservation at Site U1403 favored the preservation of calcareous nannofossils, benthic foraminifera, and ichthyoliths over other microfossil groups. Silica preservation was

generally poor precluding detailed study of radiolarian or diatom dynamics (*45*). The same was true of organic matter preservation, ruling out dinoflagellates (Table S26) and meaningful biomarker analysis (Table S28). Prior to the K/Pg impact and throughout much of the Paleocene, carbonate preservation was also poor enough to dissolve nearly all planktonic foraminifera due to the depth of the carbonate compensation depth, thereby precluding detailed faunal studies of planktonic foraminifera. Ostracods were not studied in detail at Site U1403, but a study of Late Cretaceous through Paleocene faunal dynamics at nearby Site U1407 revealed no increase in extinction rates across the K/Pg boundary relative to background rates (*173*).

Of the three potential groups at Site U1403 for detailed biotic study (calcareous nannoplankton, benthic foraminifera, and ichthyoliths), we investigated two: calcareous nannoplankton and ichthyoliths. Calcareous nannoplankton provide key biostratigraphic control on Site U1403 due to its preservation and abundance. Large amplitude oscillations in bulk carbonate $\delta^{18}O$ in the earliest Danian at IODP Site U1403 and ODP Site 1209, where rapid assemblage changes occur in both nannoplankton and foraminifera, led us to ask whether the $\delta^{18}O$ signal might simply reflect the dominance and turnover of successive nannoplankton clades. To test this, high resolution nannoplankton assemblage counts were carried out as described by Bown (*80*) at the University of College London (Site U1403; Table S17) and Penn State University (Site 1209; Table S18). For each sample listed at least 300 nannoplankton specimens were counted from randomly chosen fields of view of smears slides. At Site 1209, additional diversity scans of 50-fields of view were carried out to account for rare taxa, which are indicated with an 'x' in Table S18. Characteristic taxa at Site U1403 are show in Figure S39. Different workers collected the data at Site 1209 (JS, Penn State) and Site U1403 (HK and PB, at University College London), thus there are slight differences in taxonomy (e.g., *Coccolithus cavus* and *Coccolithus pelagicus* are grouped at Site 1209), although every effort was made to minimize differences in taxonomic concepts and naming. At both sites, reworking across the boundary (and downcore) was noted by a comparison of Cretaceous, Survivor and Incoming taxa and of the biostratigraphic age of rare down-smeared individuals (at Site 1209: *Fasciculithus*, *Sphenolithus primus*, and *Cruciplacolithus edwardsii*).

We generated new records of the mass accumulation rate of ichthyoliths at Site U1403. Bulk samples were dried, weighed, and digested with 5% acetic acid. All ichthyoliths in the >106 μm size fraction were picked to determine the ichthyoliths per gram sediment (methods as detailed in

174). The mass accumulation rate of ichthyoliths was then determined using the new cyclostratigraphic age model (i.e., Table S29) and a constant (1.08 g/cm^3) or variable dry bulk density (linearly interpolated from shipboard measurements). Ichthyolith mass accumulation rates were relatively insensitive to the dry bulk density used (Table S29), and the constant dry bulk density calculation is figured in Fig. 5.

Supplementary Discussion

Biological change in the Ocean

Deccan Trap outgassing in the latest Cretaceous is notable for the biological impacts it did, and did not, have on marine biota (Table S1). Biogeographic range changes in the latest Cretaceous include the extension of tropical and subtropical plankton to higher latitudes during peak warming (*175, 176*). At the same time, open ocean calcareous phytoplankton community structure suggests increasingly oligotrophic conditions (*177*). In our records, fish tooth abundance increased at Site U1403 in step with warming (Fig. S33, Table S29) and decreased at the K/Pg boundary. In contrast to evidence for ecological responses to warming attributed to Deccan Trap outgassing in the marine realm, there is no evidence for increased extinctions in the widespread open-ocean taxa used for biostratigraphy (e.g., foraminifera, coccolithophores, dinoflagellates, ammonoids, and ichthyoliths) as is apparent from the scarcity of biostratigraphic markers. In planktonic foraminifera, the single marker during this period is a short-lived species (*Plummerita hantkeninoides*) that originates in C29R and goes extinct at the K/Pg boundary. Given the intense interest pertaining to the timing and consequences of volcanism in the K/Pg boundary extinction, increasing age control around the boundary is a top priority. If Deccan volcanism caused significant extinctions, these would provide greater biostratigraphic control during this key time interval. The lack of markers based on last occurrences is thus notable and underscores the minimal effect of the Late Cretaceous warming on the viability of species. It has been argued that a local extinction event did occur in the shallow water marine fauna of Seymour Island coincident with late Cretaceous warming (*140*), but more extensive records do not support this (*54*). In addition, the relatively modest decline in marine $\delta^{13}C$ during late Maastrichtian warming is of the magnitude expected for a volcanogenic driver (Figs. 2,4, S22-S30), without appreciable feedbacks from the marine carbon pump (organic and/or inorganic). If, for instance, a short-pulse of volcanism just before the boundary (as in Case 3) had affected the function of marine communities we might expect the carbon cycle change to occur prior to the impact. Such a scenario would result in the collapse of $\delta^{13}C$ gradients prior to the impact ejecta (Fig. S43) and would be readily observable in the fossil record –but it is not.

On the basis of observed ecological changes, some have argued that Deccan volcanism had a destabilizing effect on communities (*178*), particularly on land (*179, 180*), but the rapid

rebound of marine plankton ranges and community structure within the latest Cretaceous and the lack of pronounced carbon cycle feedbacks in $\delta^{13}C$ suggests otherwise for the ocean. What is readily observed in the marine realm during the Late Cretaceous is multiple lines of evidence that marine communities responded to warming and coastal deoxygenation as it was occurring. Responses include the afore mentioned range shifts with warming and subsequent cooling (*175, 176*), and changes in community foraminiferal structure (composition and size structure) in coastal regions consistent with some combination of low oxygen, warm temperatures, increased environmental variability, and/or local sea level change (e.g., *181, 182-185*). In short, the biotic changes observed during the latest Cretaceous warming event are consistent with a global warming (and then cooling) event, but do not indicate a permanent change in marine ecosystems prior to impact.

A long-standing question is why Deccan volcanism would have such a muted effect when flood basalt volcanism is strongly implicated in the mass extinctions that the P/T and T/J boundaries. This differential response is potentially attributable to important earth system changes that dampened the effects of flood basalts post-P/T. Post P-T some combination of increased oxygen levels (*186*), the breakup of Pangea (*187*), and changes in the biological pump (*188, 189*) may have reduced the risk and/or intensity of marine anoxia during global warming events. In addition, after the T/J, the response of Earth's carbon cycle to exogenous perturbations fundamentally changed due to the rise of pelagic calcifiers (*41, 190, 191*). Together these changes profoundly altered the carbon cycle and its response to carbon injection events.

The effects of the K/Pg boundary differ from the Late Cretaceous warming event by coinciding with extensive evidence for marine extinctions, including the extinction of ammonites and mosasaurs (*192, 193*) and the near complete extinction of planktonic foraminifera and coccolithophores (>95% species-level extinction) (*94, 194-196*). At Site U1403, only the coccolithophores could be analyzed throughout the uppermost Cretaceous and lowermost Paleocene due to preservation, but a striking reduction in nannoplankton abundance, the disappearance of most Late Cretaceous species (there is some cross-boundary reworking; reworked specimens identified by criteria as defined in (*79, 80*)), and the first appearance of small, abundant calcispheres (calcareous dinoflagellates) all clearly coincide with the spherule layer (Figs. 5, S35; Tables S17, S24, S25). The near-complete extinction of coccolithophorids likely accounts for the ~500,000 year interval in the earliest Paleocene when bulk carbonate $\delta^{18}O$

records (typically a tracer of mixed-layer temperatures by coccolithophores) diverge from all other marine temperature estimates at Sites 1209, 1262, 1267 and U1403 (Figs. 5, S11, S12, S35). At Sites 1209 and U1403, the incoming Cenozoic taxa form a succession of acmes, with miniscule early forms (<3 μm) quickly replaced by larger taxa within the same lineages (e.g., *Cruciplacolithus*, *Prinsius*, *Coccolithus*), with the termination of rapid biotic succession coinciding with the stabilization of the bulk $\delta^{18}O$ values, similar to the rapid succession of foraminiferal taxa in the same interval (Fig. S34) (*56, 80, 95, 197*).

Following the impact, the collapse in $\delta^{13}C$ between planktonic and benthic species was so extraordinary that a total cessation of marine productivity was hypothesized when it was first observed (the Strangelove Ocean hypothesis) (*198*). Although more modest changes in the biological pump are now thought to account for the pattern (*23, 48, 49, 53, 85, 132, 199*), this collapse to reversal in carbon isotope gradients stands out as the largest carbon cycle perturbation in the pelagic carbonate fossil record for over 150 million years (i.e., since the evolution of pelagic calcifiers). Following the impact, surface to deep ocean $\delta^{13}C$ gradients recovered to ~75% of pre-extinction values within ~300,000-500,000 years, coinciding with the first major change increase in plankton community richness (*94, 200*). Notably, the timing of $\delta^{13}C$ gradient collapse and partial recovery occurs in step with changing carbonate preservation conditions in the Atlantic and Pacific Oceans (Fig. 2, (*48*)) and major changes in plankton community structure (*94*). In the late Maastrichtian, Site U1403 appears perched just above the carbonate compensation depth (i.e., the maximum depth below which carbonate is not preserved in sediments). Moderately well-preserved coccolithophores are abundant but the relatively dissolution-prone planktonic foraminifera are almost absent (Figs. 5, S34-S35)(*45*) until the earliest Paleocene when sediments go from nearly barren to ~30% planktonic foraminifera by weight. The pronounced change in carbonate preservation at Site U1403 reflects a global phenomenon, with distinct improvement in the quality of carbonate preservation in the deep-sea and a 1-2 km deepening of the CCD in the earliest Paleocene (*41*). However, the weight % coarse fraction dynamics differs among the three best resolved sites (Fig. 2), possibly due to orbitally paced changes in ocean circulation and/or chemistry.

Exceptions to the Global Temperature Compilation

The global temperature compilation documents fairly stable, roughly Cretaceous-like temperatures in the earliest Paleocene (Fig. 1), with distinct differences between the relative temperatures recorded in terrestrial (cooler) and marine (warmer) archives (Figs. S13-S14). Three exceptions necessitate discussion: very brief excursions, the Dan-C2 event, and the long-term warming trend.

The time-integrated nature of most samples in the compilation mean that they do not capture very short-term excursions including the impact winter and warming rebound. A 1-cm thick interval at most deep sea sites in the lower Paleogene spans several thousand years due to low sedimentation rates, and up to 10,000 years due to sediment mixing (*172*). Recent modeling work has emphasized the severity of the impact winter due to sulfur (*26*) and soot (*27*) in the years following the impact. This is generally consistent with empirical evidence from TEX_{86} for impact winter in the months to decades following the impact in highly expanded, coastal sections (*24, 144*). The same studies provide evidence of a warming overshoot of ~1-2°C in the first few thousand years following the impact winter (*144, 201*), consistent with a biospheric driver like the loss and regrowth of biomass. Interestingly, bulk carbonate records of $\delta^{13}C$ appear to have a two-step decline in values after the K/Pg impact, with the first step lasting a few thousand years (Figs. 5,S17-S19, S44), which is also consistent with a short-lived perturbation like the loss and regrowth of terrestrial biomass. However, planktonic foraminifera from the same sites do not show this two-step $\delta^{13}C$ drop (Figs. S34-S35), either because foraminiferal records are less temporally resolved (with individuals carried beyond their stratigraphic range due to mixing (*172*)) than bulk carbonate, or because the bulk carbonate record reflects changes in the composition of carbonate fine fraction (i.e., nannoplankton) rather than the global carbon cycle (*122*). Similarly, TEX_{86} records from shallow coastal locations must be interpreted with caution due to the confounding effects of different environmental factors on the distribution of archaeal GDGTs, like oxygen concentration (*202*) and ammonia oxidation rate (*203*) both of which can vary widely in shallow water settings, as well as the possibility of terrestrial sources of GDGTs not captured by the BIT index (*204, 205*). Regardless, a brief post-impact warming of a few thousand years, if it did occur (*144, 201*), it cannot be attributed to Deccan degassing and subsequent weathering feedbacks because the rate at which the warming signal was removed (less than one thousand years) is far too fast for the weathering feedbacks that typically

drawdown volcanogenic CO_2 inputs. This is important because it also means that it is very unlikely that any very short warming burst was driven by Deccan Trap volcanism.

The potential Dan-C2 event, which is recognized on the basis of a carbon isotope excursion in some localities, is hypothesized to be an earliest Paleocene global warming event that occurs ~250,000 - 300,000 years after the K/Pg boundary (*43, 130, 206*). The magnitude and duration of the Dan-C2 event would be consistent with a Deccan volcanism related driver, if outgassing were delayed relative to the impact as previously hypothesized (*15*), although the evidence for global warming during the Dan-C2 remains scant (*42*). If the Dan-C2 were a global warming event (which it appears not to be), it would tie Deccan volcanism to the recovery of biotic diversity rather than the loss, as this event occurs near a turning point in many geochemical and assemblage records from the open ocean, as they begin to return to pre-impact like values and diversities. The appeal of this possible link to the Dan-C2 event is that volcanic outgassing from a large igneous province has been hypothesized to drive some later hyperthermal events (like the PETM (*207*)). However, as we show here, extensive changes to the carbon cycle due to the K/Pg mass extinction should mask and/or mute the potential climate effect of volcanic degassing during the earliest Paleogene (Fig. 3, S28). However, Deccan outgassing might have occurred over a relatively shorter time interval than we modeled, and at a turning point in the strength of the biological pump, so that it might have had the carbon cycle effects attributed to the Dan-C2, with relatively muted (or non-existent) evidence for coincident global warming (*43, 130, 206*).

Finally, perhaps the most unexpected finding of our modeling regards the gradual long-term warming trend of about 1°C over the first 600 kyrs of the early Paleocene (Fig. 1). Our modeling demonstrates that the recovery of the biological pump in the aftermath of the K/Pg extinction resulted in a gradual increase in atmospheric pCO_2. In fact, this effect was so strong, that many of the scenarios for the timing of biological pump recovery result in far too sudden (and pronounced) warming in the earliest Paleocene (Fig. S27). The gradual and prolonged pump recovery, starting immediately in the K/Pg impact aftermath and continuing over 1.77 million years, was overall the best scenario for the warming trends observed. The difference amongst biological pump recovery scenarios in the pattern of ocean saturation state, pCO_2, and temperature change (Fig. S27), suggest a clear path forward for advancing our understanding of the timing of marine carbon cycle recovery after the K/Pg impact.

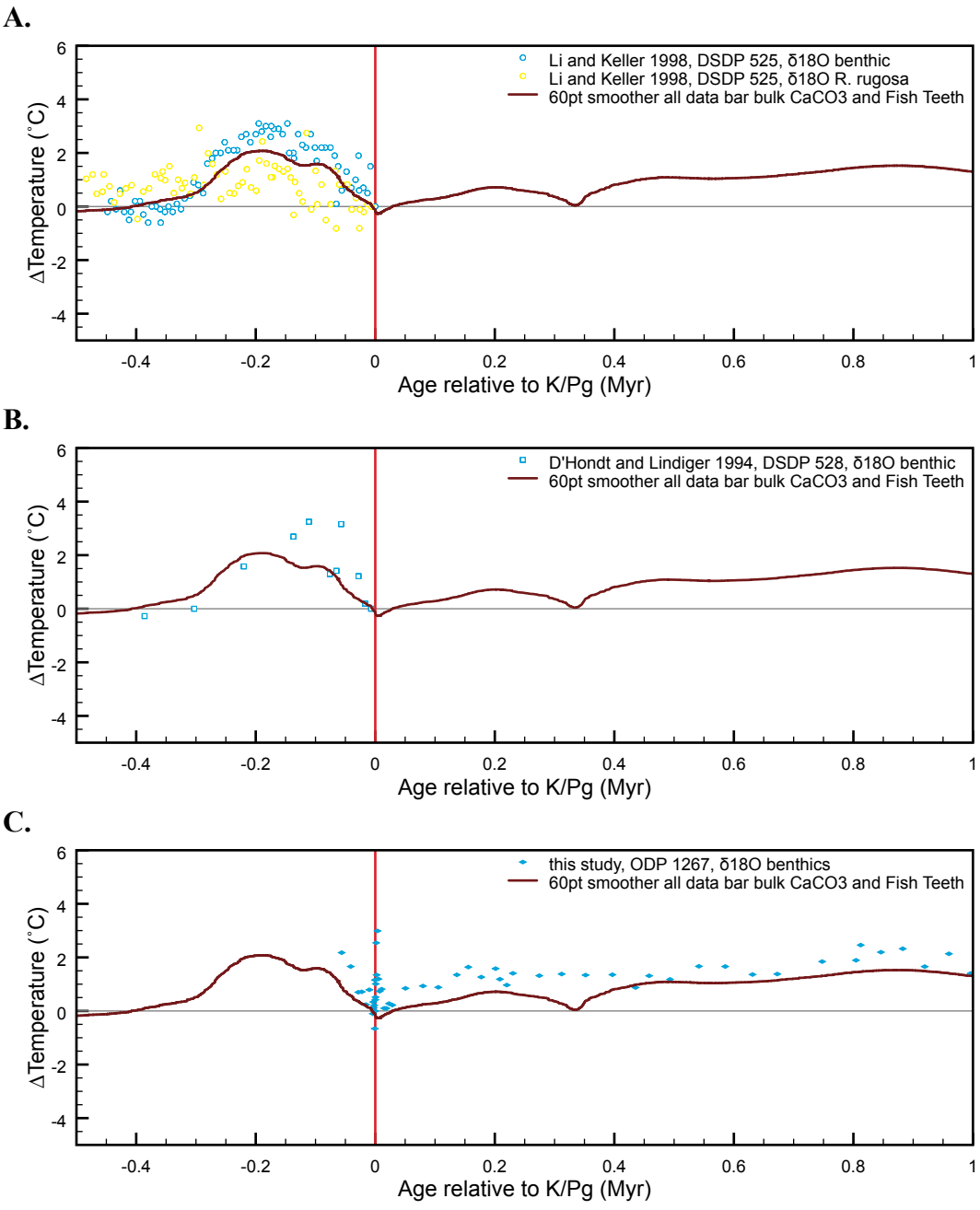

Fig. S1.
Temperature records from Walvis Ridge sites: (A) DSDP Site 525 (*44*), (B) DSDP Site 528 (*128*), and (C) ODP Site 1267 (*this study*), on unified age models and a common $\delta^{18}O$-temperature equation.

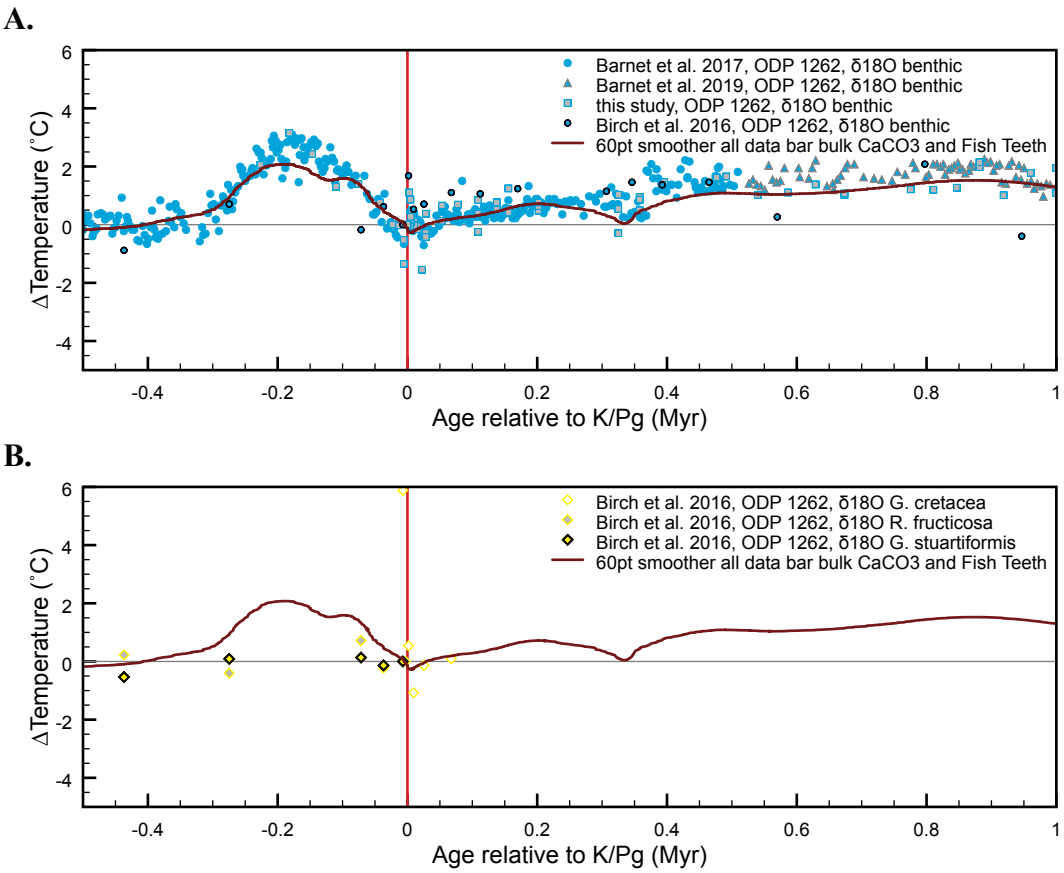

Fig. S2.
Temperature records from Walvis Ridge sites (cont.): ODP Site 1262 (A) benthic foraminiferal $\delta^{18}O$ ((*42, 43, 49*), *this study*) and (B) planktic foraminiferal (*49*), on unified age models and a common $\delta^{18}O$-temperature equation. Note that the study by ref. (*49*) includes more planktic foraminiferal $\delta^{18}O$ data, but those shown are only those species with overlap with the K/Pg boundary, that can thus be expressed in ΔTemperature relative to the boundary.

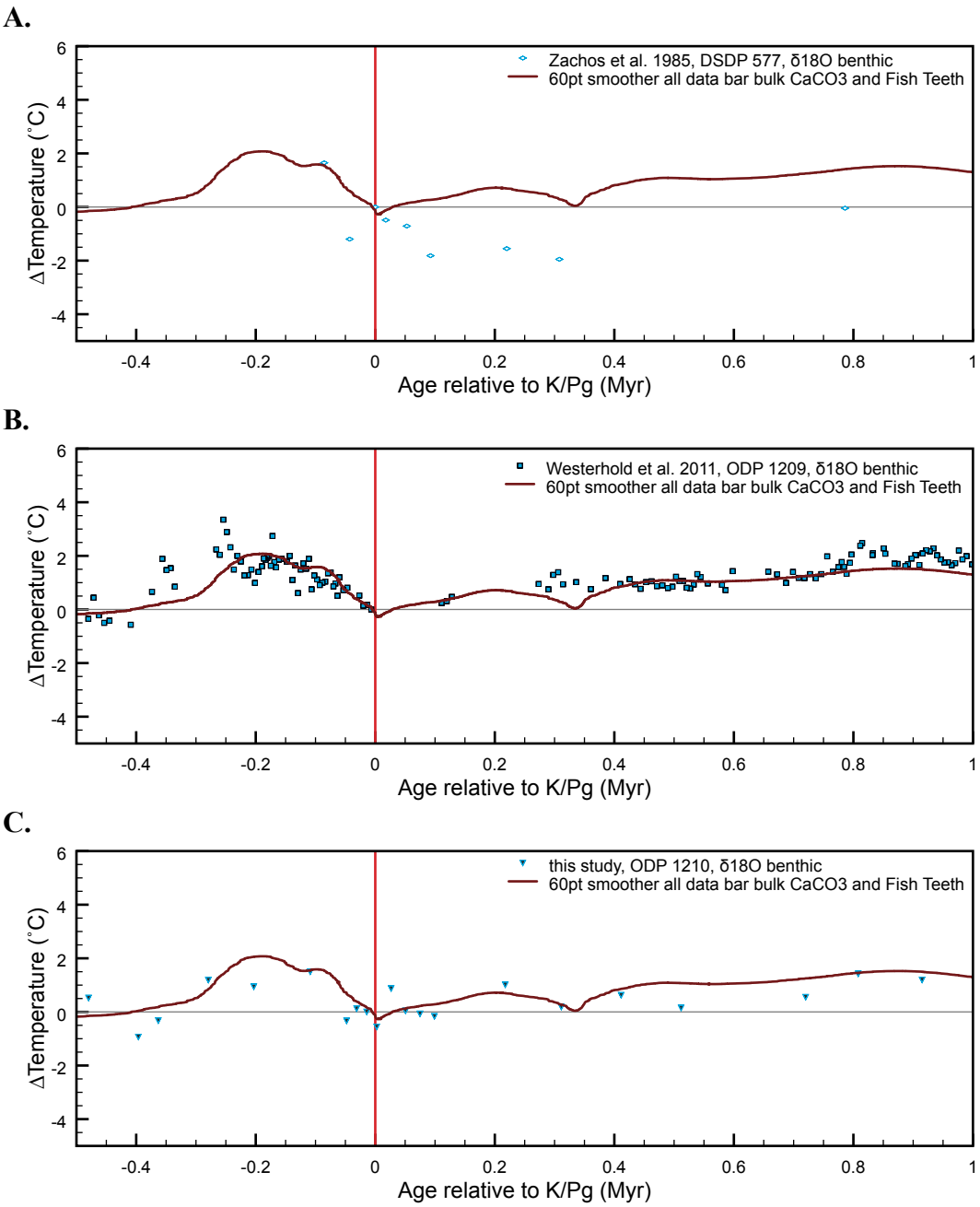

Fig. S3.
Temperature records from Shatsky Rise sites: (A) DSDP Site 577 (*90*), (B) ODP Site 1209 (*73*), and (C) ODP Site 1210 (*this study*), on unified age models and a common $\delta^{18}O$-temperature equation.

A.

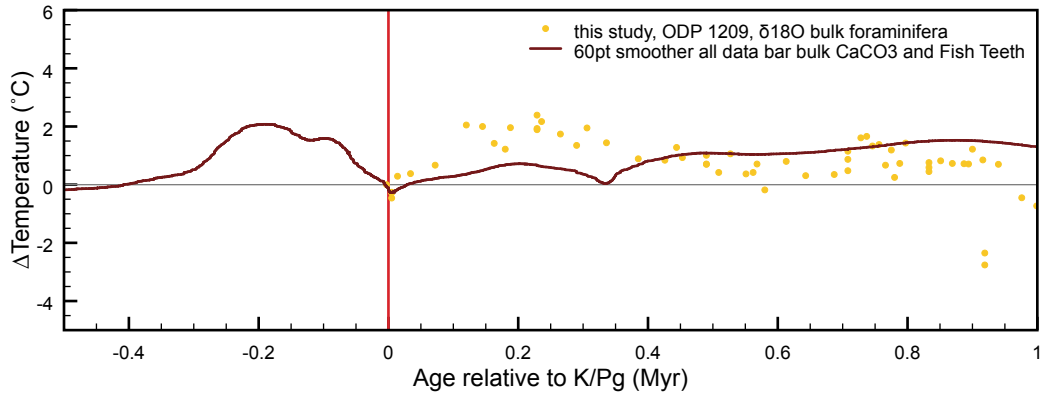

B.

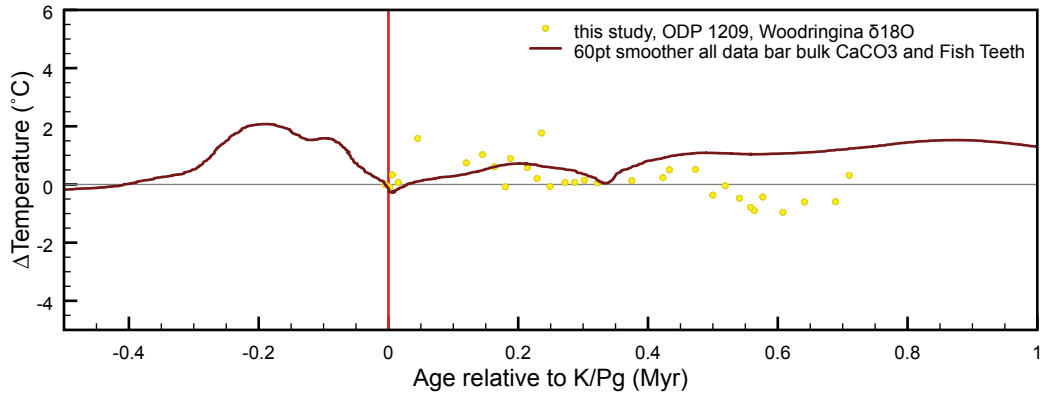

Fig. S4.
Temperature records from Shatsky Rise, ODP Site 1209 (A) bulk foraminifera, i.e., homogenized 38-125µm sieve size fraction material (*this study*), and (B) mixed *Woodringina* species (*this study*), on unified age models and a common $\delta^{18}O$-temperature equation.

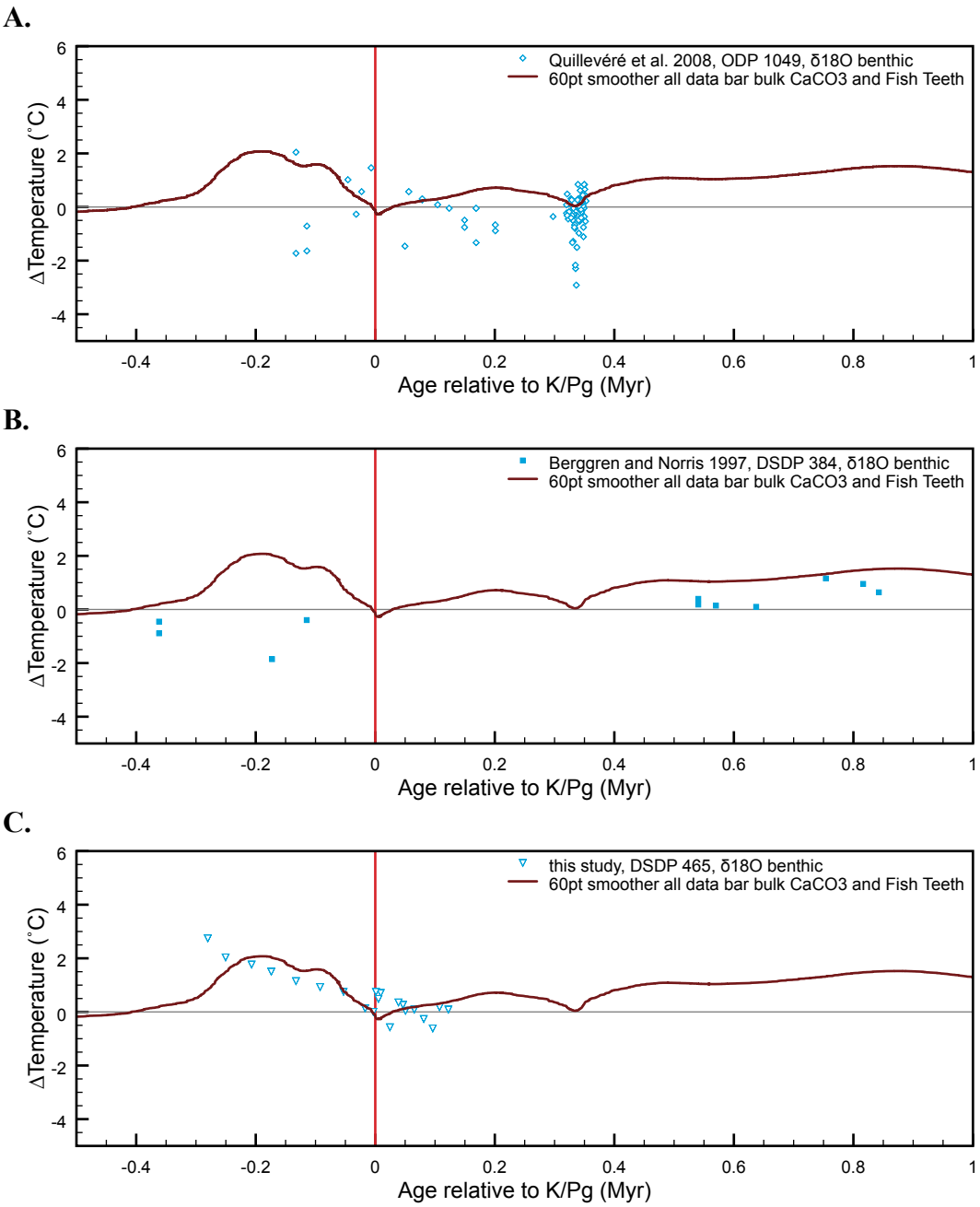

Fig. S5.
Temperature records from (A) Blake Nose, ODP Site 1049 (*130*), (B) J-Anomaly Ridge, DSDP Site 384 (*131*), and (C) Hess Rise, DSDP Site 465 (*this study*), on unified age models and a common $\delta^{18}O$-temperature equation.

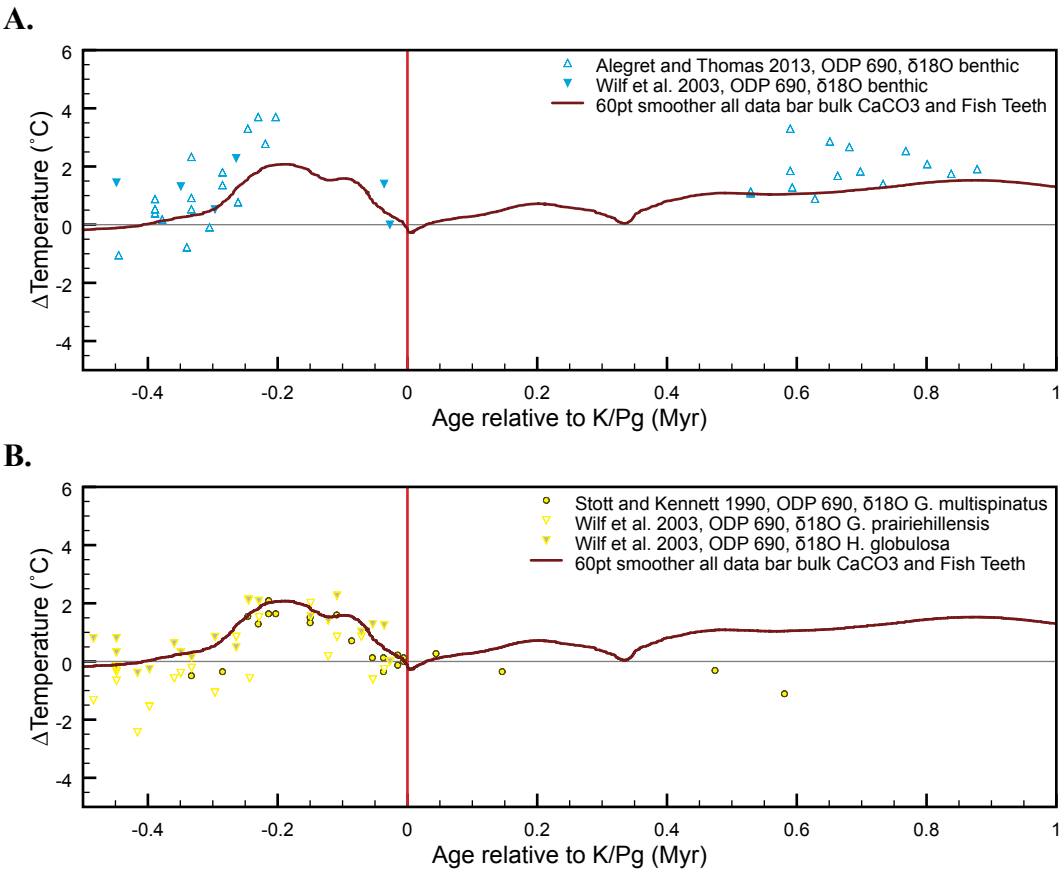

Fig. S6.
Temperature records from Maud Rise ODP Site 690: (A) benthic foraminiferal $\delta^{18}O$ ((*129*), (*136*)), (B) planktic foraminiferal $\delta^{18}O$ (*135, 136, 208*), on unified age models and using a common $\delta^{18}O$-temperature equation. Note for data in panel A, ΔTemperature is calculated relative to a measurement of *Nuttallides truempyi* at the K-Pg boundary from ref. (*136*).

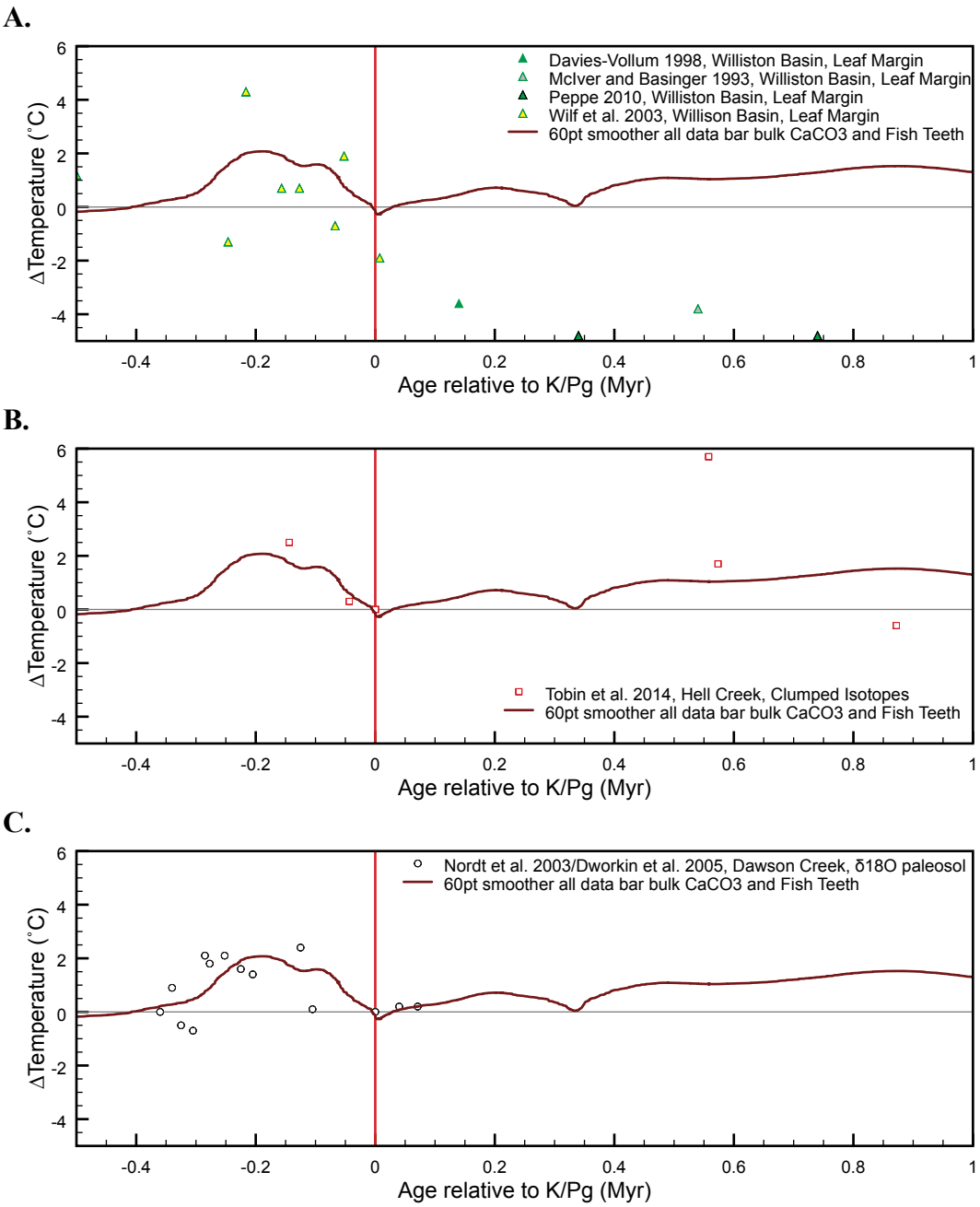

Fig. S7.
Temperature records from (A) the Williston Basin leaf margin data set (*136, 146-149*), (B) from Hell Creek, clumped isotopes of mollusks (*141*), and (C) Dawson Creek $\delta^{18}O$ of paleosols (*137, 138*), on unified age models.

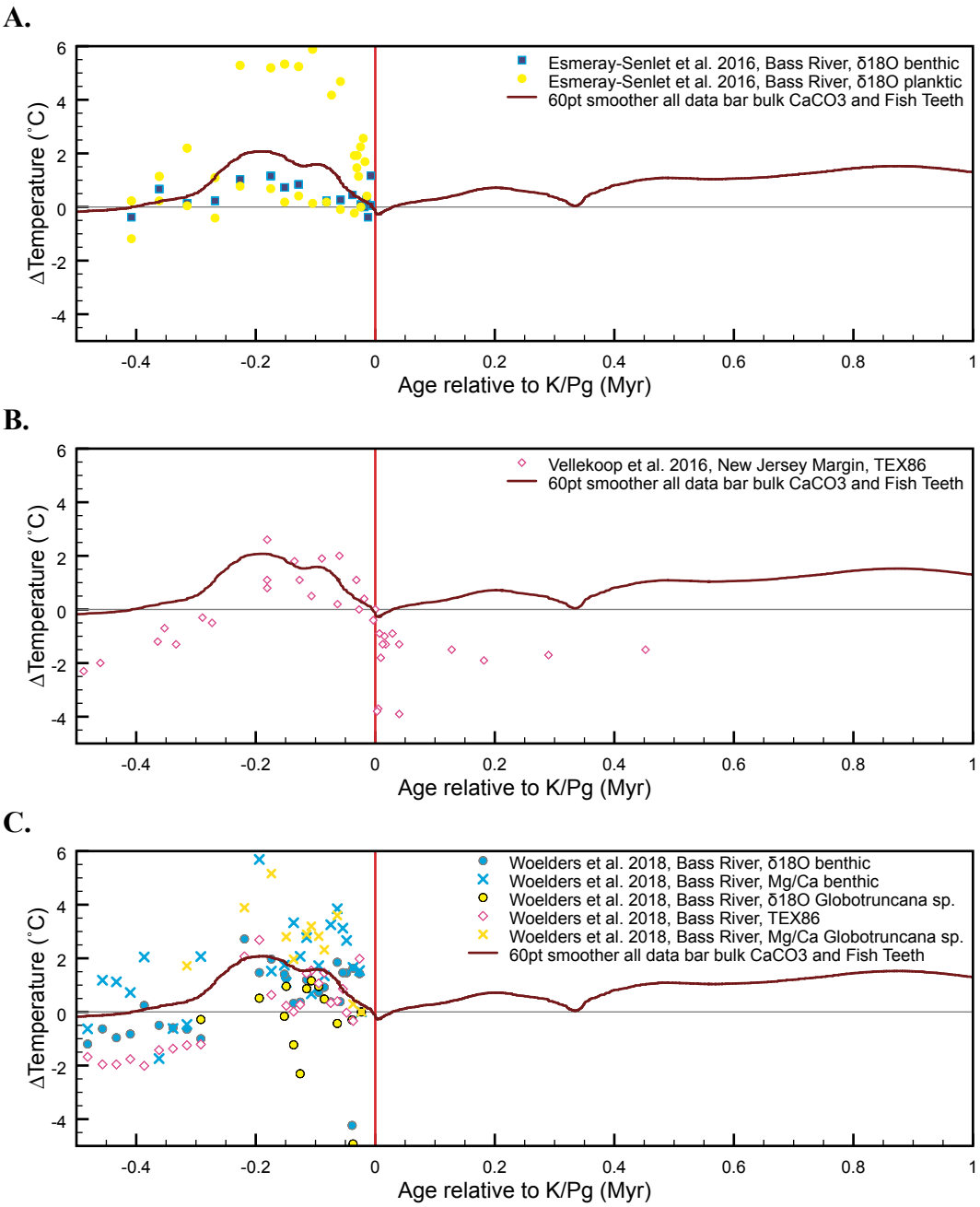

Fig. S8.
Temperature records from Bass River (A) $\delta^{18}O$ of foraminifera (*132*), (B)TEX_{86} (*144*), and (C) mixed proxies (*145*), on unified age models and a common $\delta^{18}O$-temperature equation.

A.

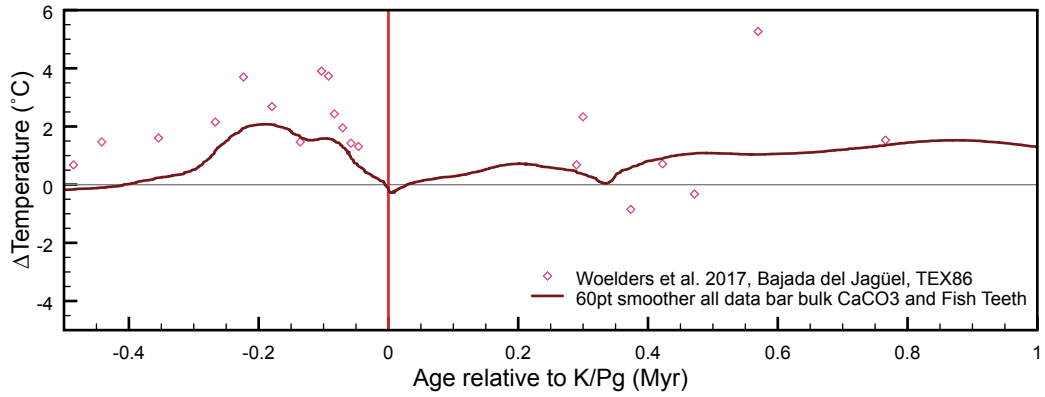

B.

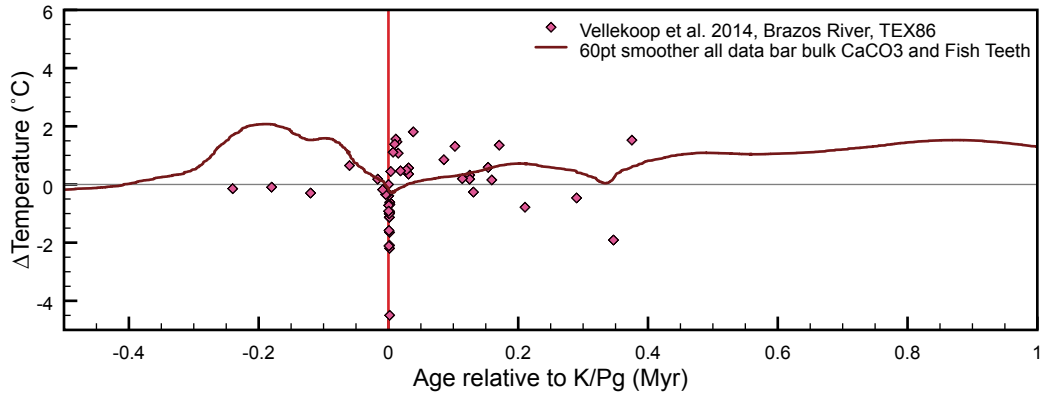

Fig. S9.
Temperature records from (A) Bajada del Jaguel (*97*), and (B) Brazos River (*24*), on unified age models.

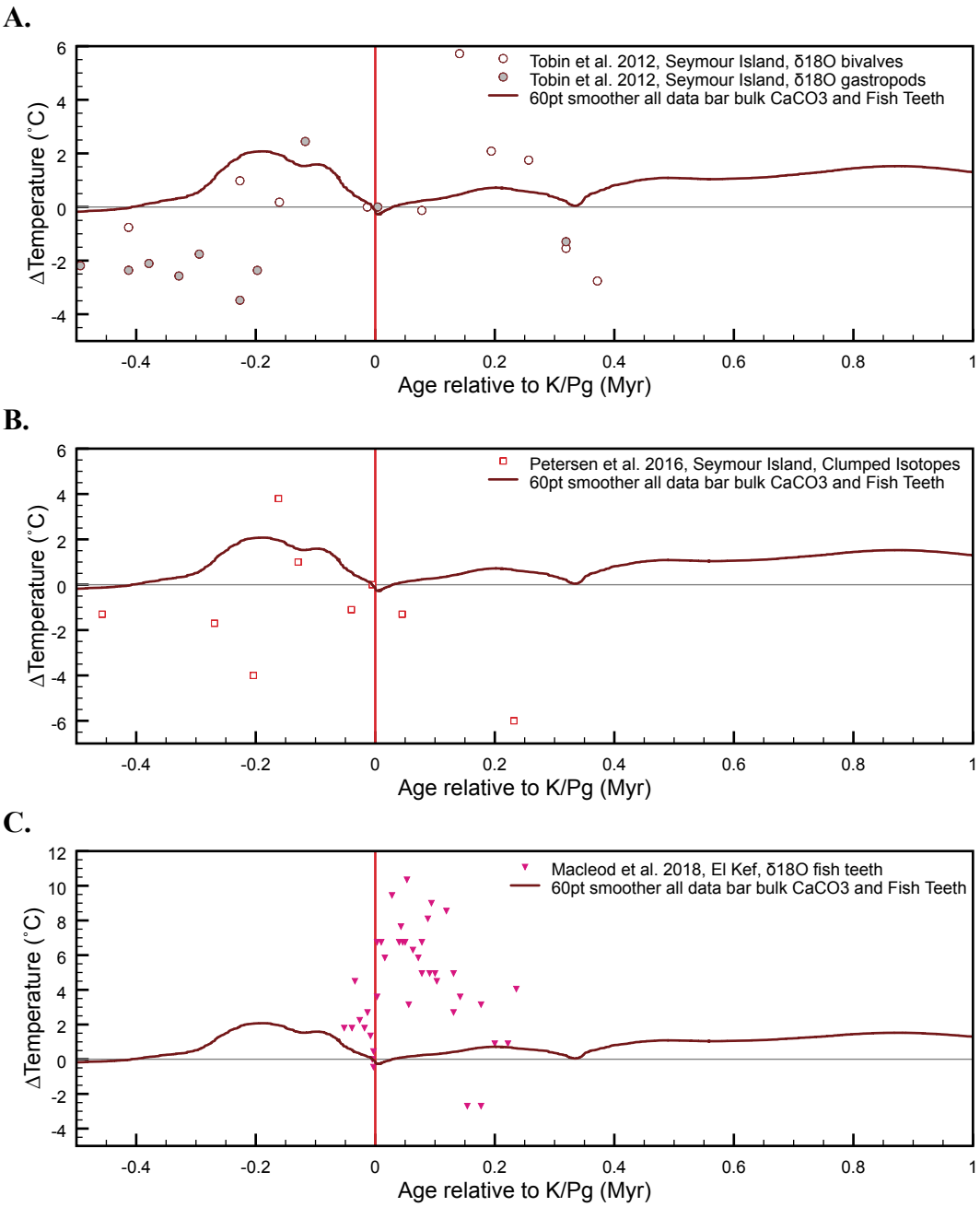

Fig. S10.
Temperature records from Seymour Island, Antarctica (A) $\delta^{18}O$ of mollusks (*140*) and (B) clumped isotopes of mollusks (*209*), and fish teeth at El Kef (*52*), on unified age models.

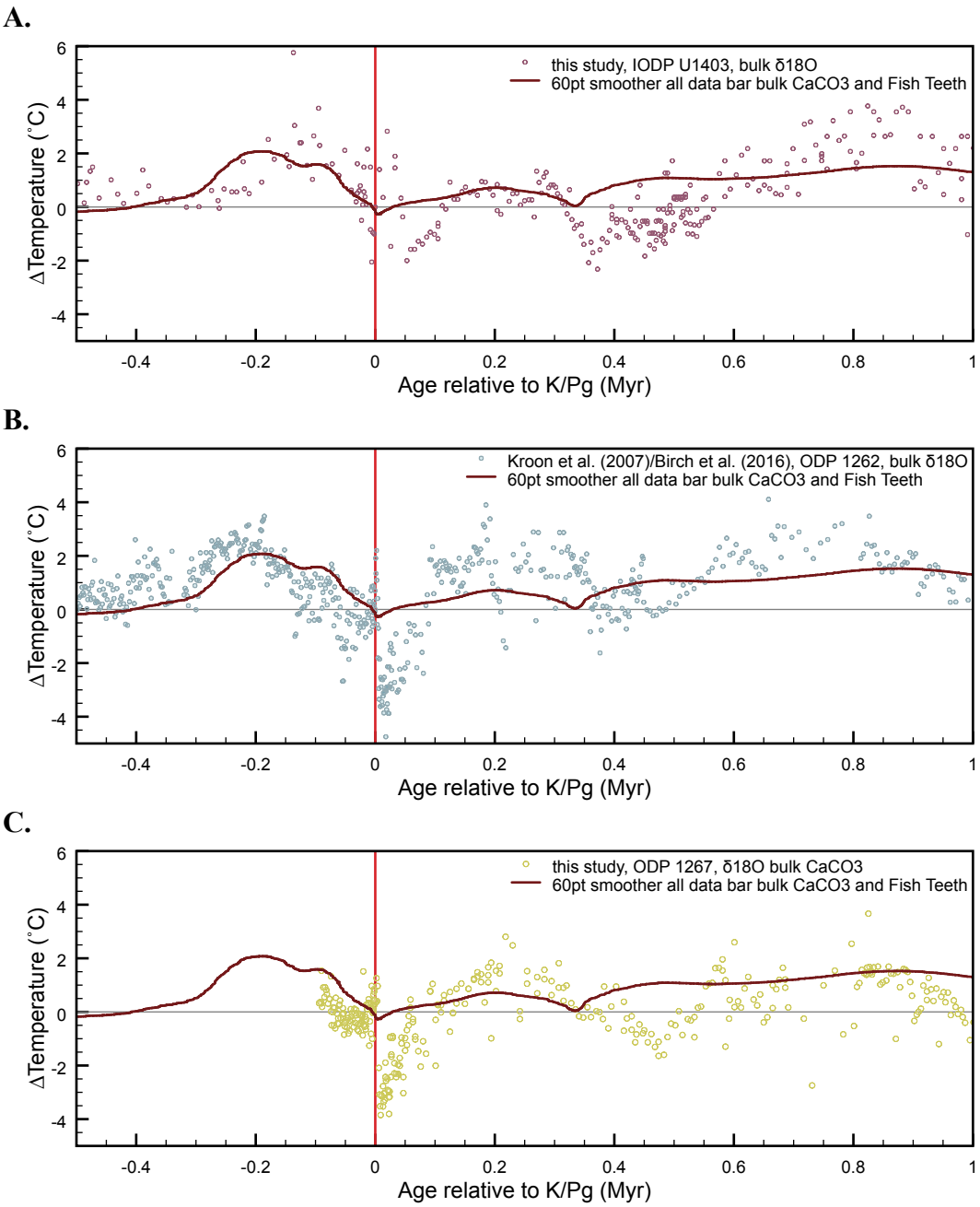

Fig. S11.
Temperature records from bulk carbonate at (A) IODP Site 1403 (*this study*), (B) IODP Site 1262 (*49, 96*), and (C) IODP Site 1267 (*this study*), on unified age models and a common $\delta^{18}O$-temperature equation.

A.

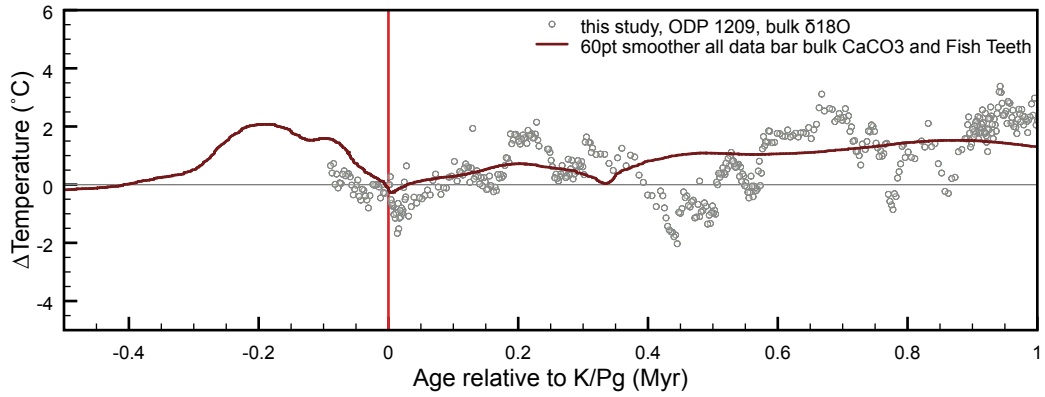

Fig. S12.
Temperature records from bulk carbonate at (A) ODP Site 1209 (*this study*), on unified age models and a common $\delta^{18}O$-temperature equation.

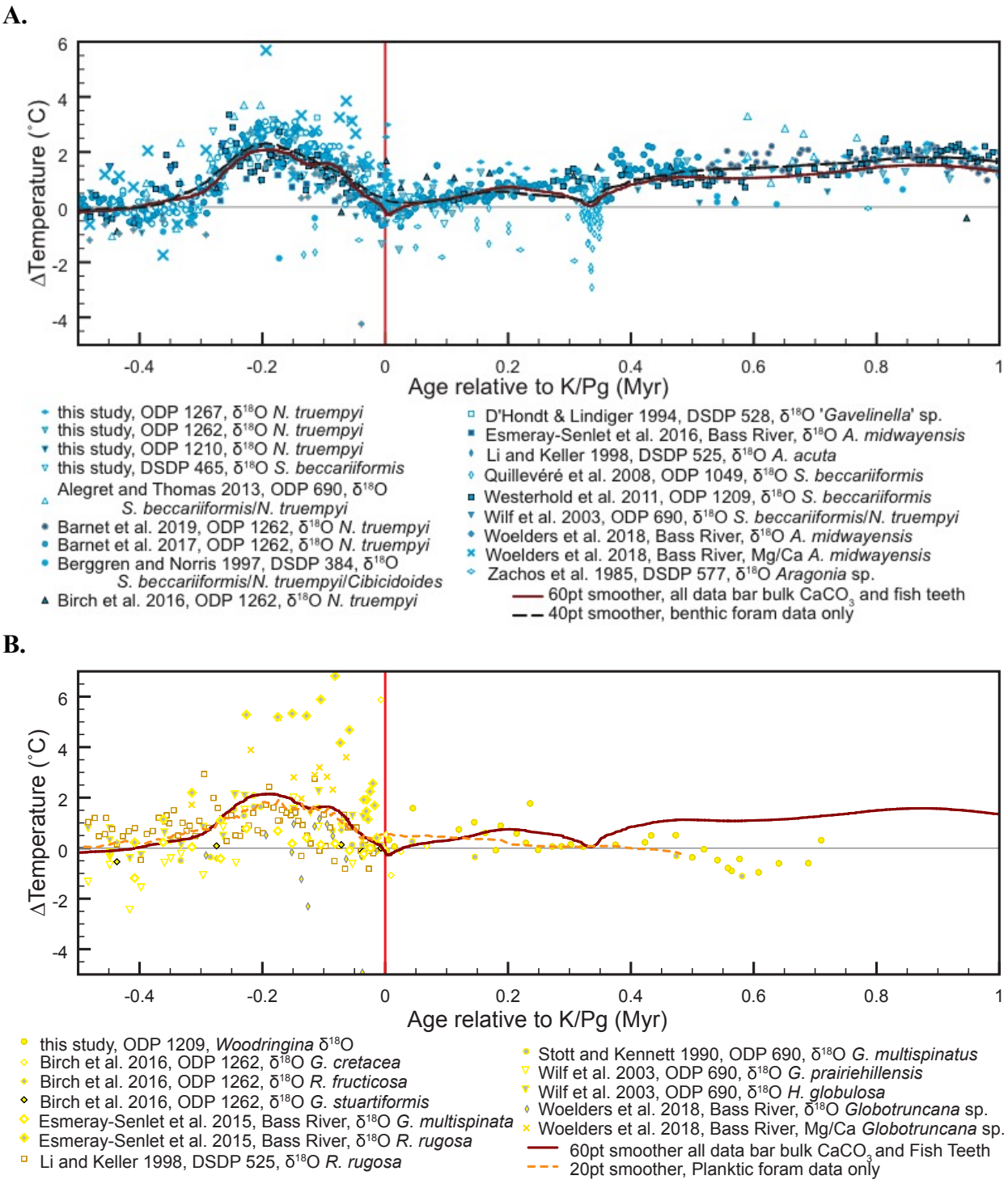

Fig. S13.
Comparison of all foraminiferal temperature datasets (shown individually in Figs. S1-S12) versus the global temperature composite, including (A) benthic foraminifera $\delta^{18}O$ based temperature estimates, and (B) planktonic foraminifera $\delta^{18}O$ based temperature estimates, on unified age models and a common $\delta^{18}O$-temperature equation.

A.

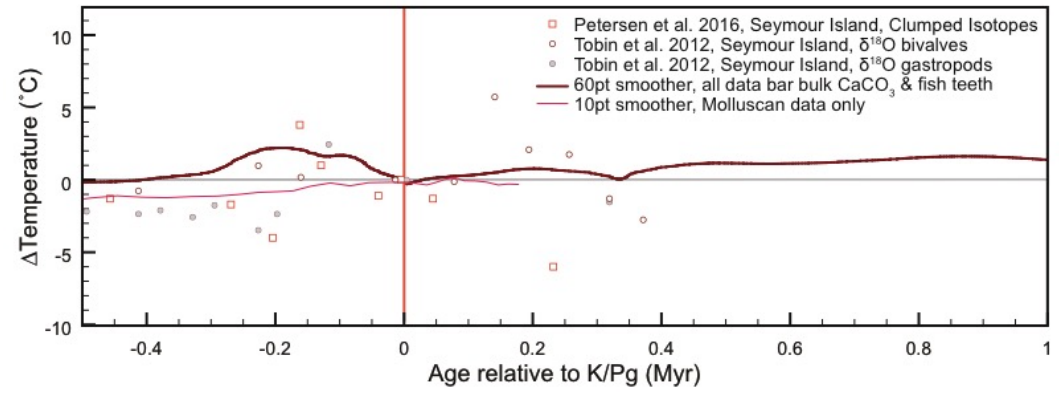

B.

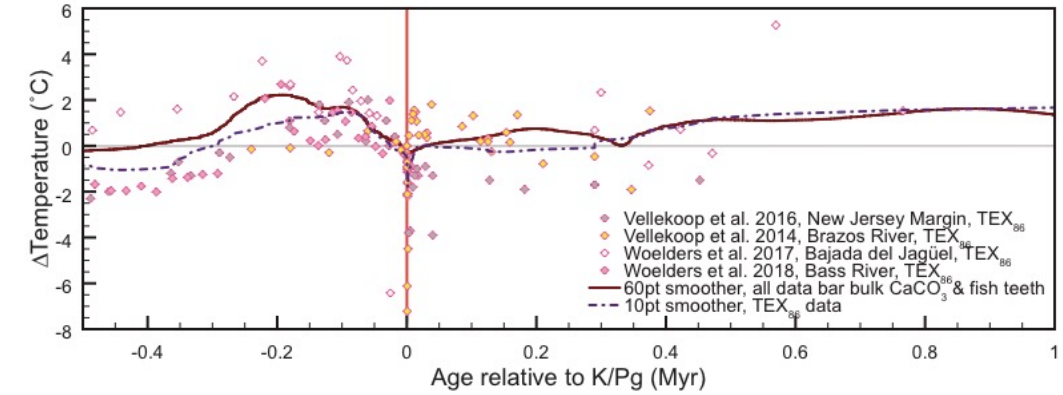

C.

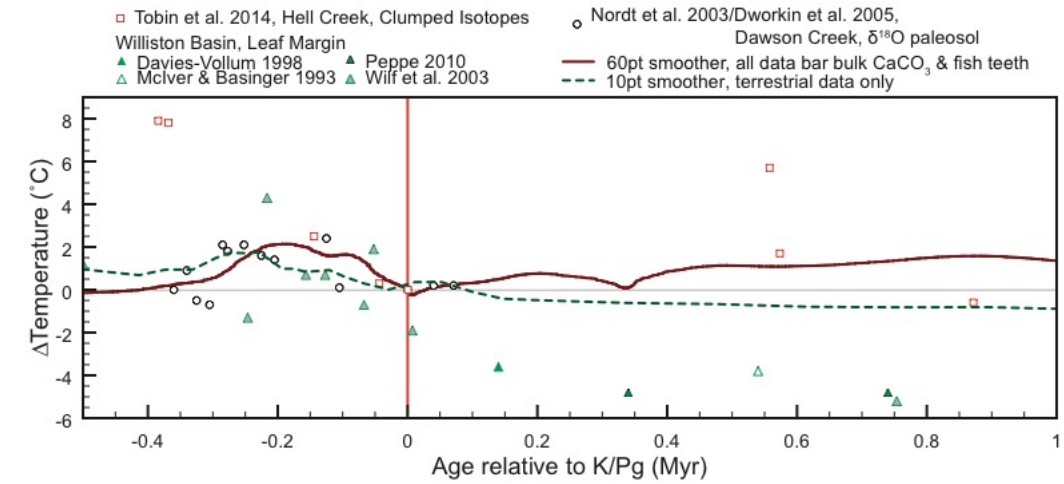

Fig. S14.
Comparison of all (A) mollusk temperature proxy data, (B) TEX_{86} temperature proxy data, and (C) terrestrial temperature estimates, versus the global temperature composite (as shown individually in Figs. S1-S12), on unified age models and a common $\delta^{18}O$-temperature equation.

A.

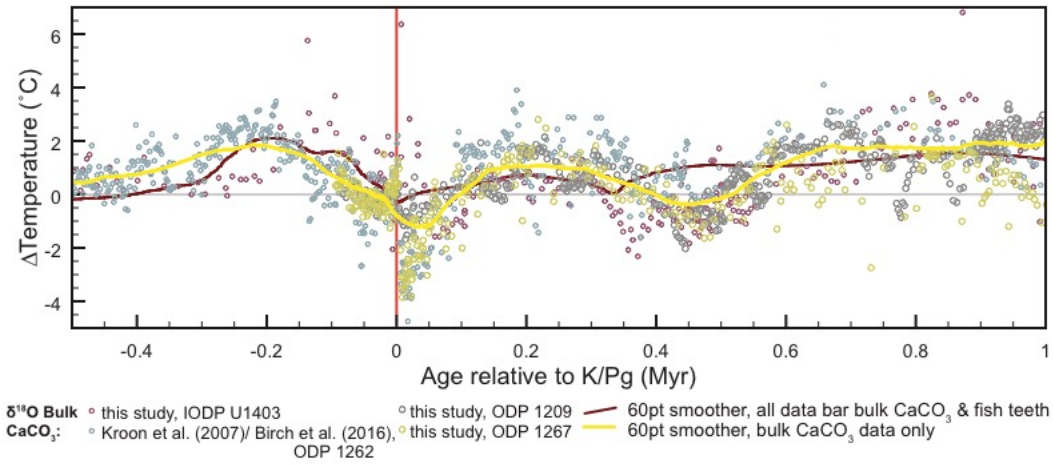

B.

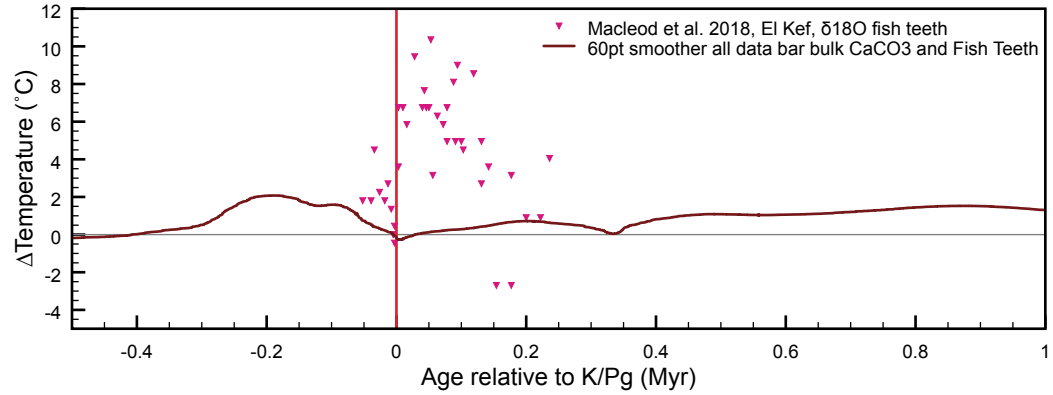

Fig. S15.
Examination of proxies likely not tracking temperature in the earliest Paleocene due to extinction related changes in communities including (A) bulk carbonate $\delta^{18}O$, and (B) fish tooth apatite $\delta^{18}O$ (*52*), on unified age models and a common $\delta^{18}O$-temperature equation.

A.

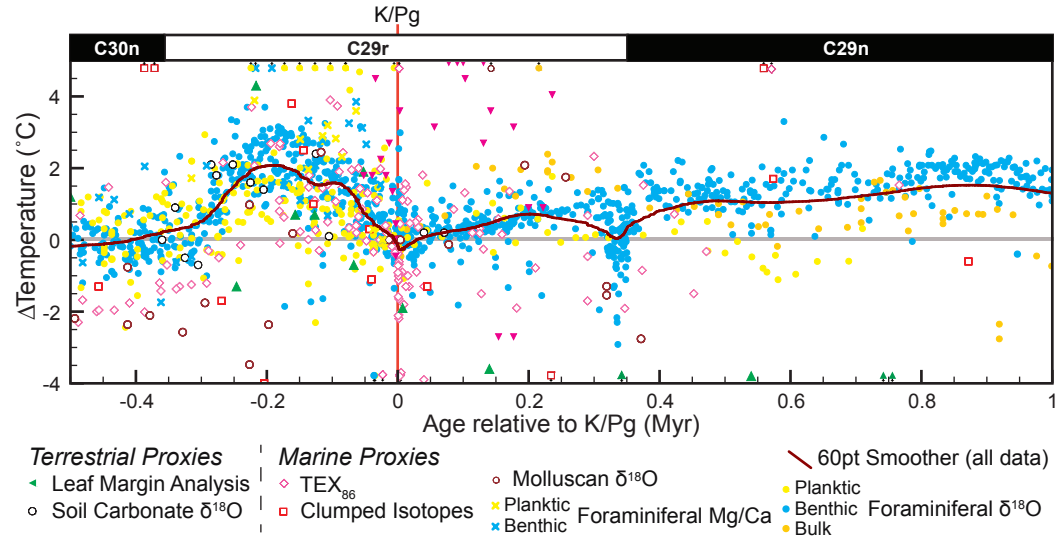

B.

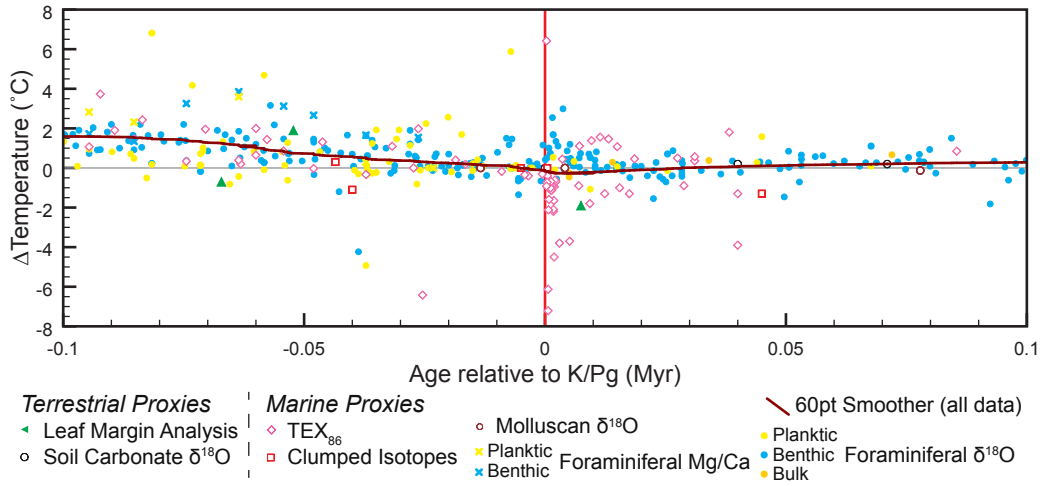

Fig. S16.
Global temperature composite across the K/Pg with a 60pt fast Fourier transform for (A) the full time window, and (B) the K/Pg boundary proper. Data as in Fig. S1-S12, but shown by dataset and proxy type, and excluding bulk carbonate $\delta^{18}O$ and fish teeth $\delta^{18}O$ which are unlikely to be tracking regional temperature change (as shown in Fig. S15). Note that the smoothing approach used naturally weights to the most data-dense records although most individual records of various proxy types do show the major features of the compilation (Figs S1-S12), and it does not account for differences in temporal or paleotemperature proxy uncertainty.

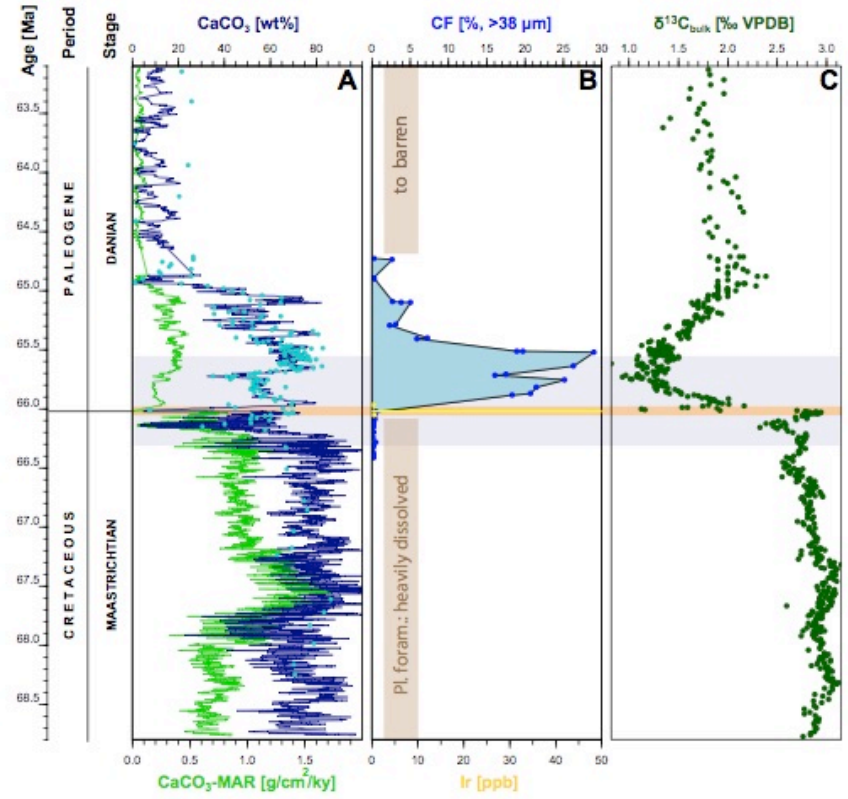

Fig. S17.

A long, high-resolution Cretaceous baseline at IODP Site U1403 evidences the unusually large perturbation of the Cretaceous-Paleogene impact. Multiproxy records from IODP Site U1403 provide the first expanded (~3 million year) Cretaceous paleoceanographic baseline with centimeter scale resolution from a site with an intact K/Pg boundary spherule layer include (a) $CaCO_3$ mass accumulation rate (green) and wt % $CaCO_3$ (blue) inferred from XRF core scanning of Ca and Fe and calibrated with shipboard and mass-spec based measurements of wt % $CaCO_3$ (light blue), (b) wt % course fraction record from washed core samples (blue) with the interval barren to intact planktonic foraminifera indicated in brown and iridium concentrations in yellow, and (c) $\delta^{13}C$ of bulk carbonate (green). The light orange band indicates the K/Pg boundary and the pale indigo bar indicates the interval of Deccan Trap emplacement. Data in Tables S12, S15, S19, S20, S21.

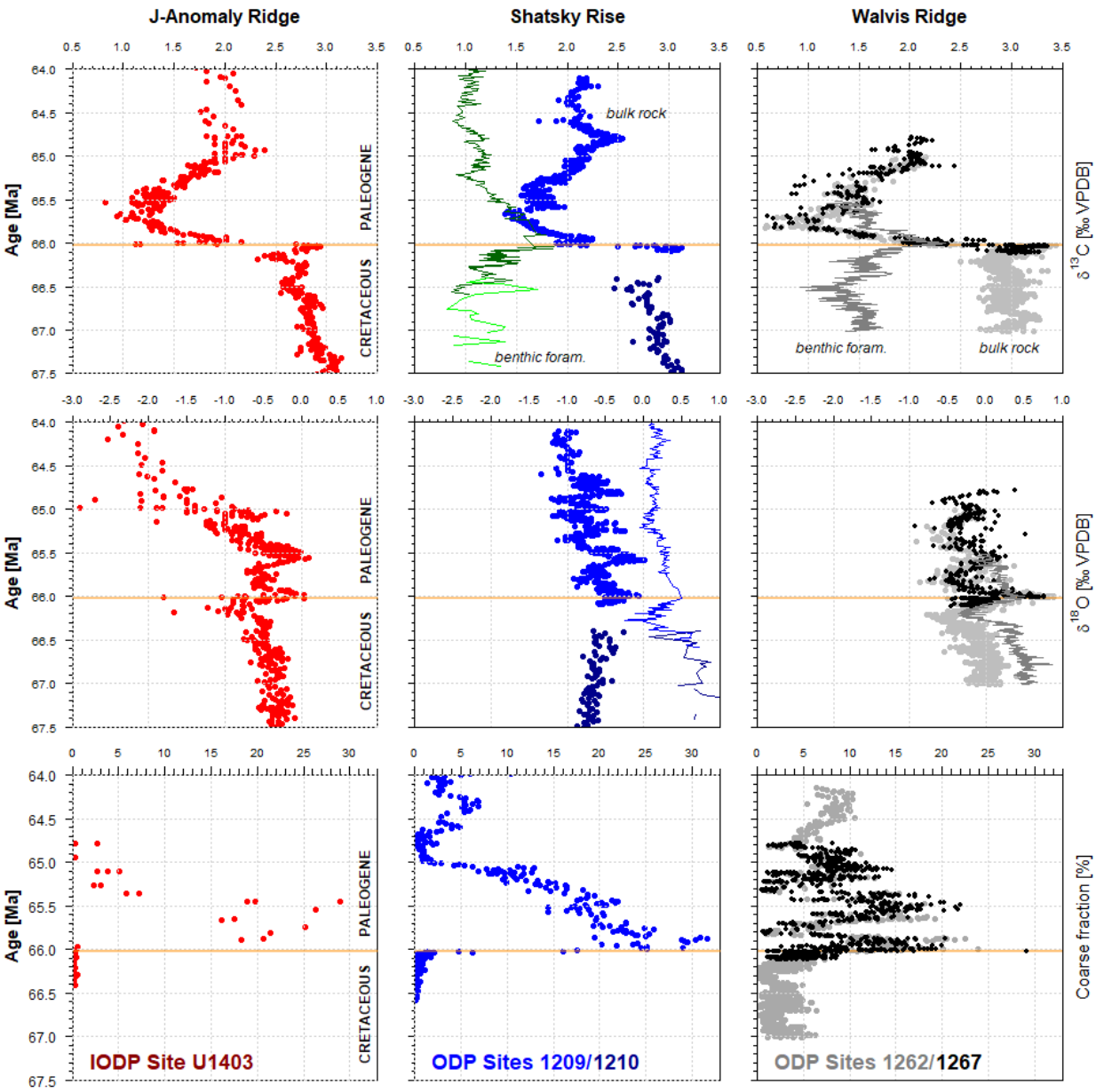

Fig. S18.

New and published (*42, 49, 73-75, 96*) high resolution bulk carbonate and benthic foraminiferal carbon and oxygen records and weight percent coarse fraction records across the K/Pg boundary at the three focal sites (J-Anomaly Ridge, Shatsky Rise, and Walvis Ridge), focused on the last 1.5 million years of the Cretaceous and first 2 million years of the Paleocene.

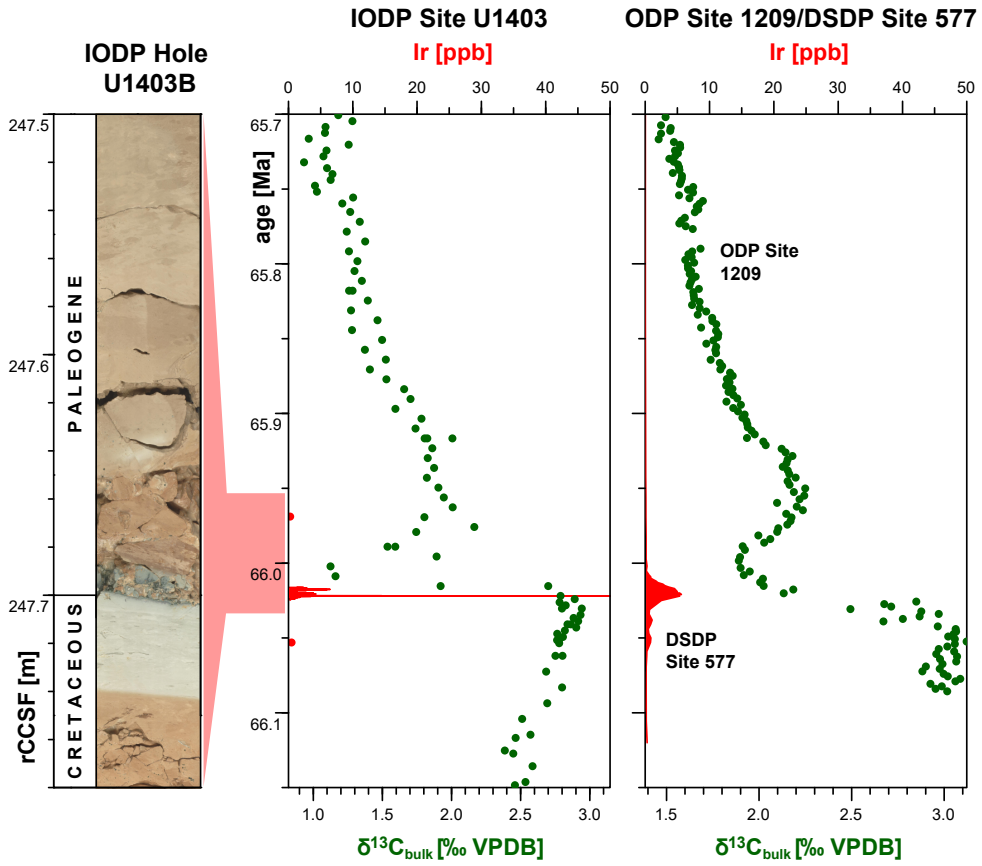

Fig. S19.

Iridium anomalies and the $\delta^{13}C$ gradient collapse in the North Atlantic and Central Pacific. Iridium anomaly (red) and $\delta^{13}C$ excursion (green) at (a) Site U1403, Newfoundland, aligned to core photo of the impact layer, and (b) Shatsky Rise in the North Pacific (iridum anomaly from DSDP Site 577; $\delta^{13}C$ from ODP Site 1209).

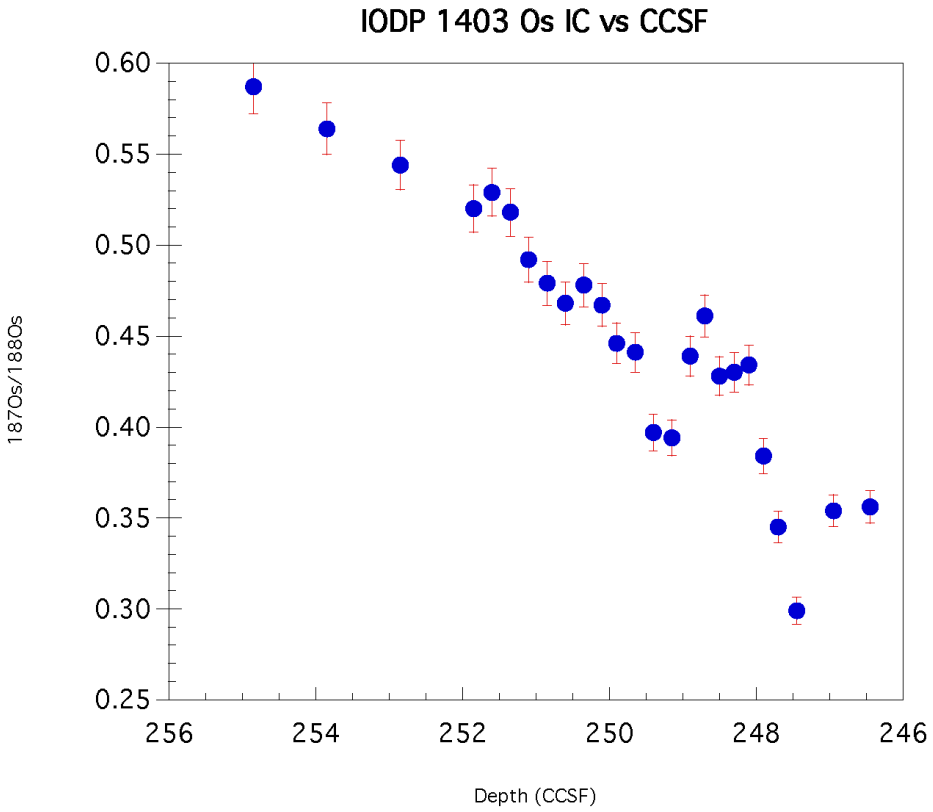

Fig. S20.
Osmium isotope record from IODP Site U1403, with 95% confidence intervals.

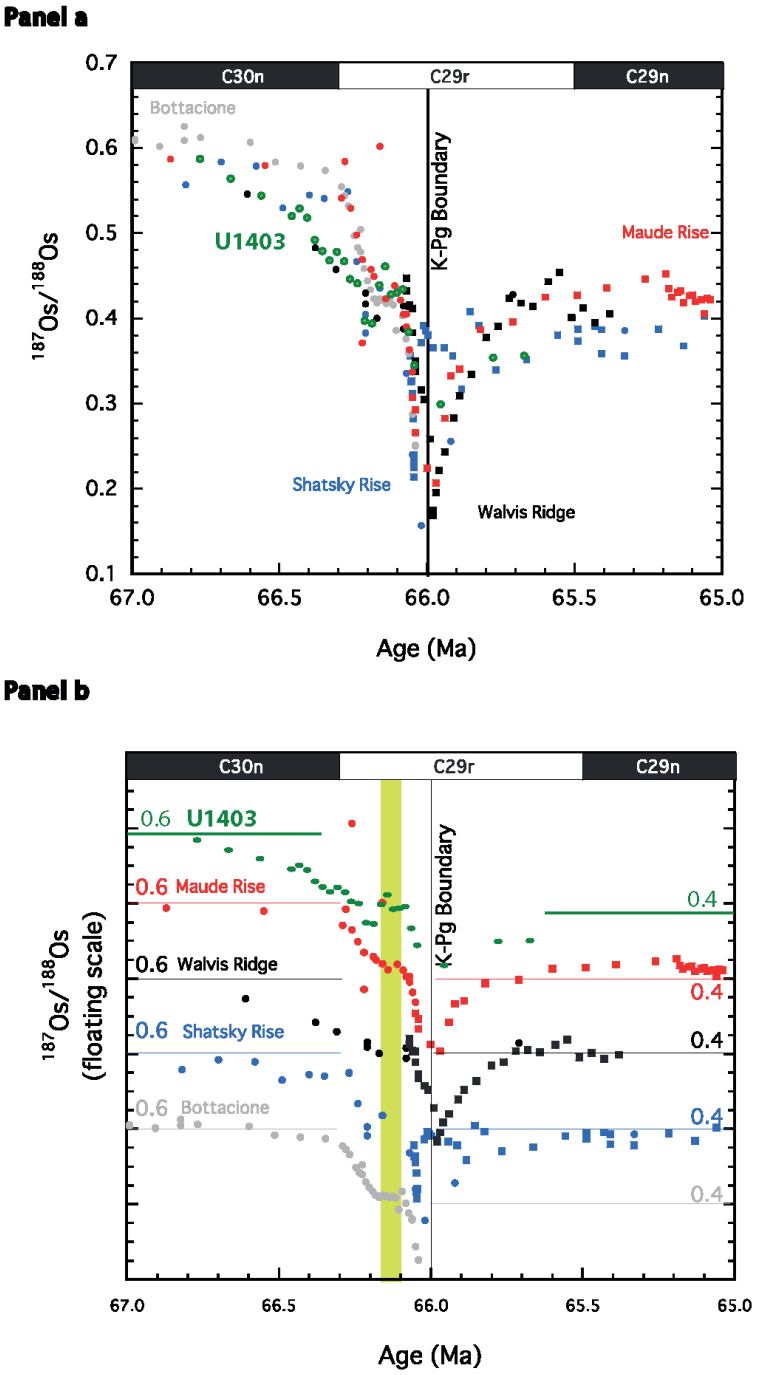

Fig. S21.
Osmium isotope record from Site U1403 relative to published records used for isotope stratigraphy (*6, 46, 117*), on absolute (a) and floating (b) scales.

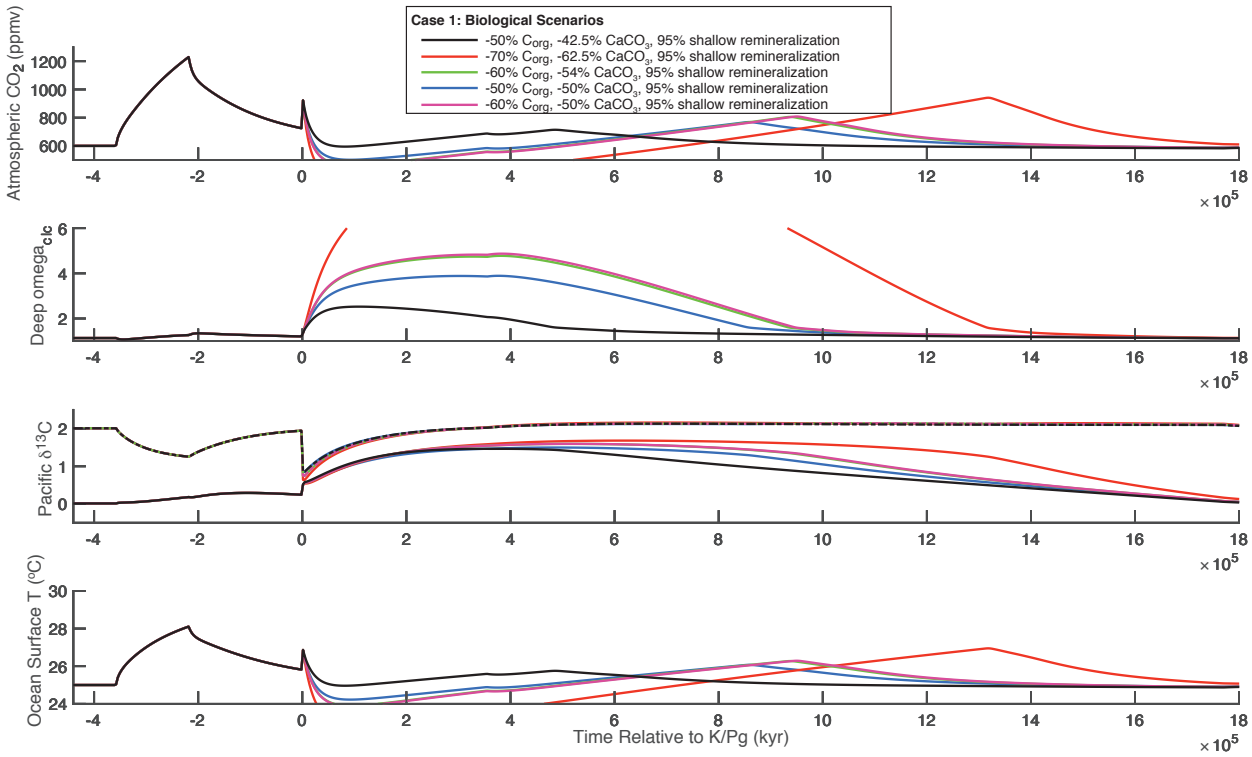

Fig. S22.

Biological scenarios explored for Case 1. All tests assume enhanced remineralization rates after the K/Pg (95% shallow water remineralization post-K/Pg and 75% prior to the K/Pg), impact degassing, and a Case 1 outgassing scenario with high Deccan emissions and a climate sensitivity of 3°C/doubling. Biological scenarios explored include a 50-70% reduction in organic carbon export and somewhere between no change and a 25% increase in the $CaCO_3$ to C_{org} export ratio. Even though we explored only increases in the $CaCO_3$ to C_{org} export ratio (to minimize the oversaturation of the deep ocean) these scenarios resulted in dramatic declines in the total export flux of carbonate to the deep sea due to the reduction of organic carbon (between 42.5% and 62.5% reduction in $CaCO_3$ export). The best scenario in terms of minimizing the increase in deep sea carbonate saturation and the decrease in earliest Paleocene temperatures was a 50% reduction in C_{org} with a 15% increase in the $CaCO_3$:C_{org} rain ratio (42.5% $CaCO_3$ export reduction).

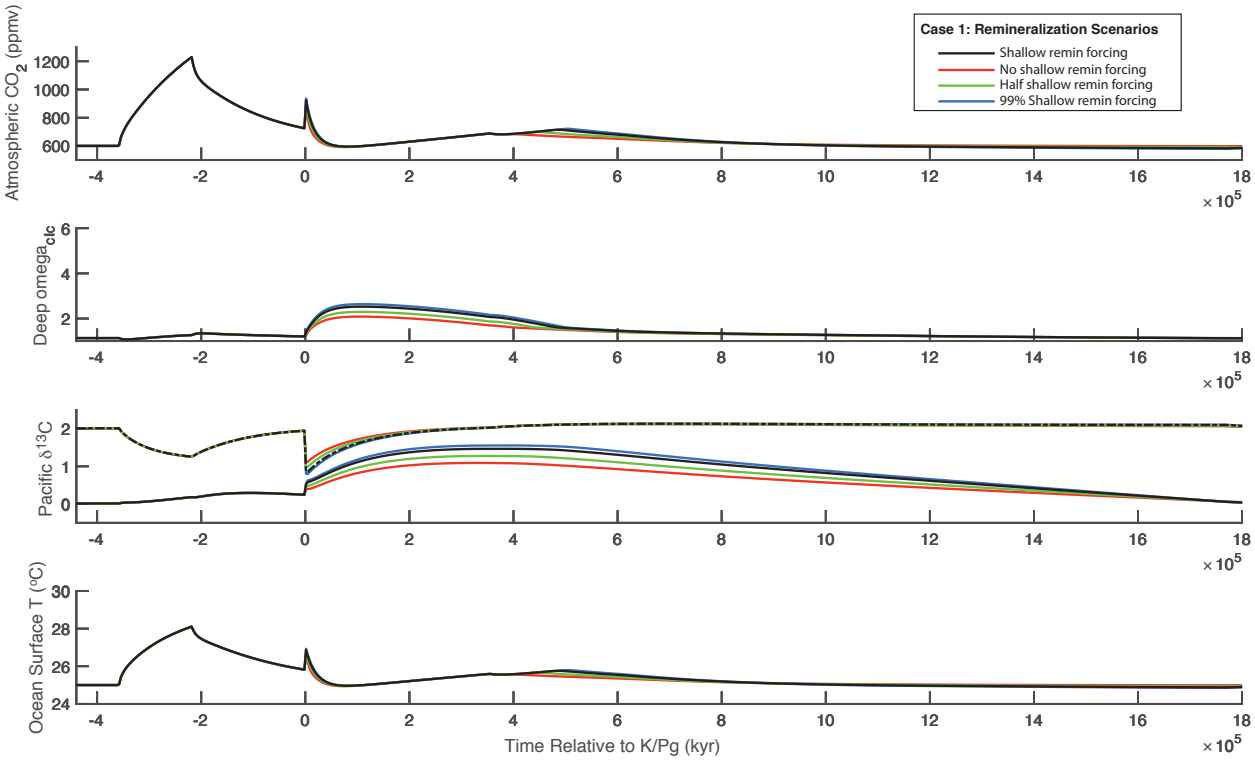

Fig. S23.

Exploration of the effect of changes in shallow water remineralization (the fraction of sinking organic carbon that is remineralized in the intermediate ocean reservoirs, as opposed to the deep) on Case 1. All tests assume impact degassing, a Case 1 outgassing scenario with high Deccan emissions and a climate sensitivity of 3°C/doubling, and a biological change scenario of a 50% reduction in C_{org} with a 15% increase in the $CaCO_3$:C_{org} rain ratio. The effect of shallow water remineralization on the early Paleocene marine carbon cycle in LOSCAR was explored by holding remineralization constant across the boundary at 78% ('No shallow remin. forcing'), increasing shallow water remineralization to 86% ('Half shallow remin. forcing'), 95% ('Shallow remin forcing'), and 99% ('99% Shallow remin forcing). Because of the relatively minimal effect of this factor, our initial scenario (and increase from 78% to 95% at the K/Pg) was used in all other modelling scenarios.

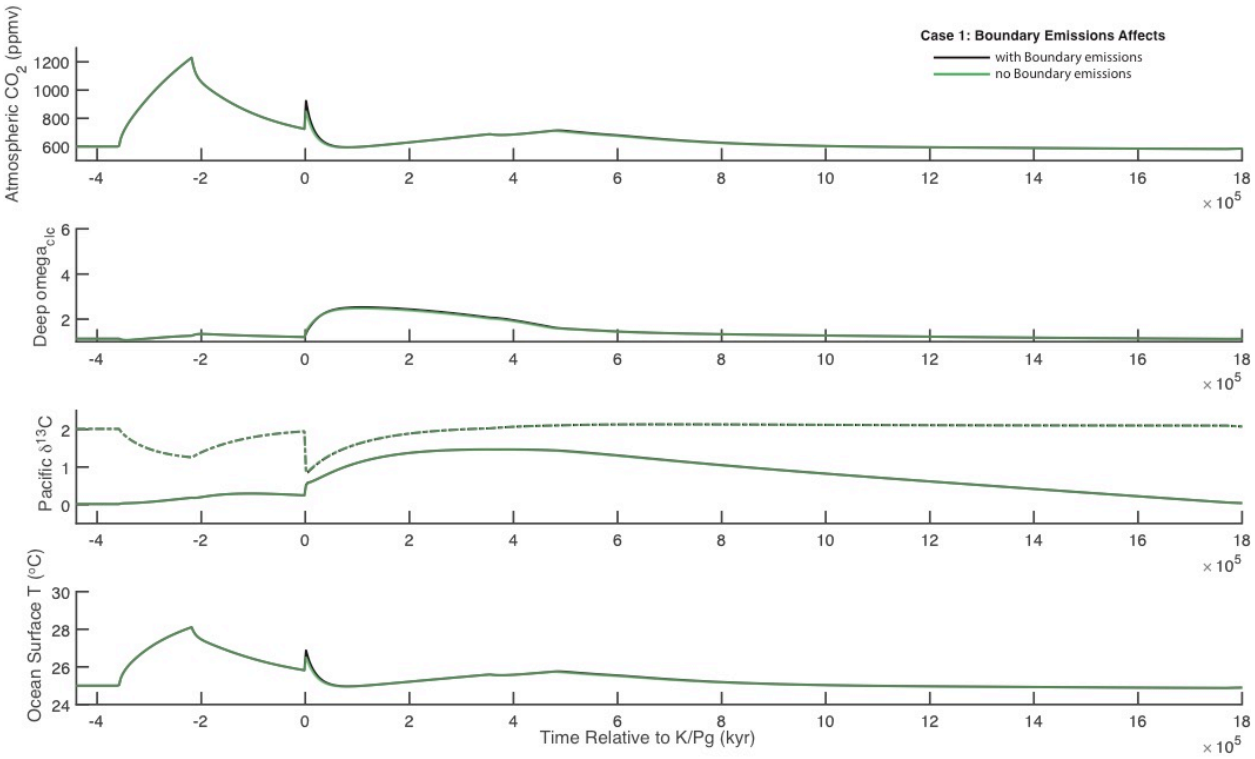

Fig. S24.

Effect on including or excluding K/Pg boundary emissions of 325 Gt S and 425 Gt CO_2 (*17*) from impact degassing on Case 1. Case 1 conditions shown here include a Case 1 outgassing scenario with high Deccan emissions and a climate sensitivity of 3°C/doubling, and a biological change scenario of a 50% reduction in C_{org}, a 15% increase in the $CaCO_3$:C_{org} rain ratio, and an increase in shallow water remineralization from 78% to 95% at the K/Pg. Impact degassing has a negligible effect on the simulation behavior, and is included in all other model simulations explored in this study.

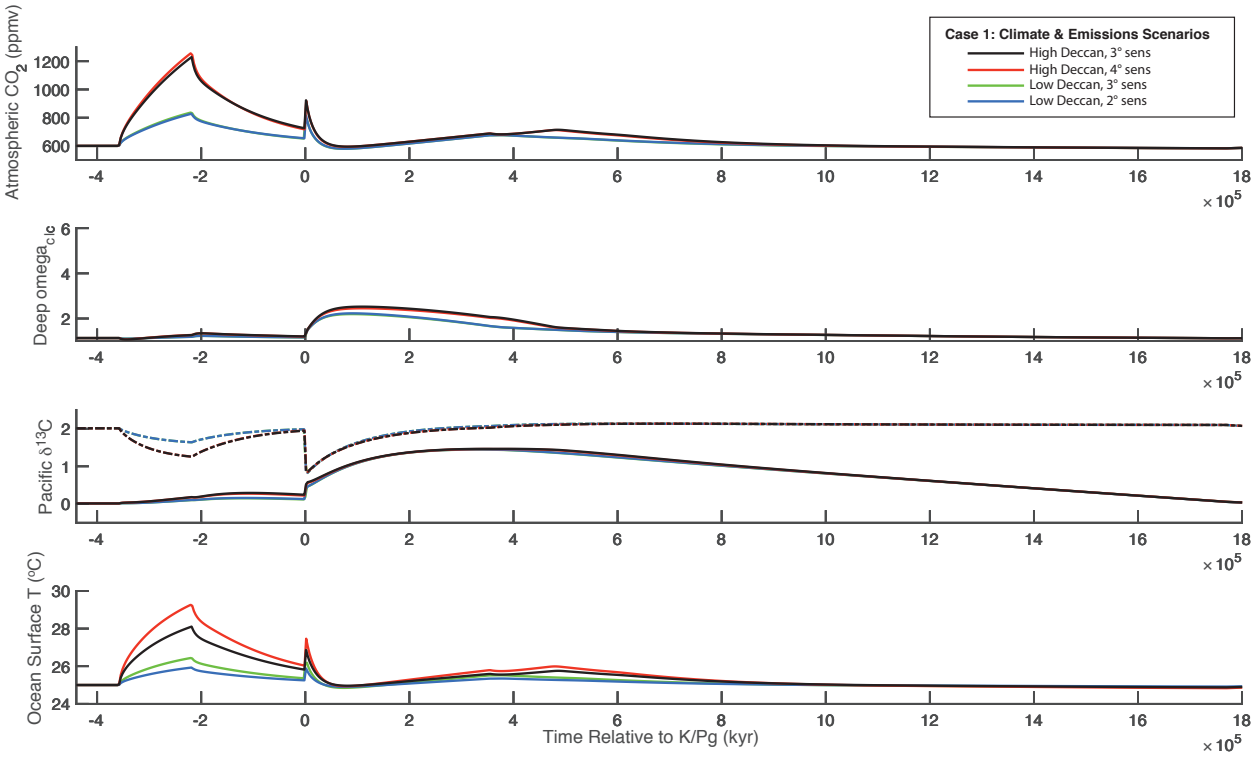

Fig. S25.

Effect of volcanic outgassing volume and climate sensitivity on Case 1 simulation behavior. Case 1 conditions shown here include a Case 1 outgassing scenario and a biological change scenario of a 50% reduction in C_{org}, a 15% increase in the $CaCO_3$:C_{org} rain ratio, and an increase in shallow water remineralization from 78% to 95% at the K/Pg. High and low Deccan outgassing scenarios assume upper and lower end-estimates for total volcanic outgassing volumes of 4090 (low) versus 9545 (high) Gt C and 3200 (low) and 8500 (high) Gt S (*10, 12*)), with climate sensitivities (°C/doubling) as described in the legend.

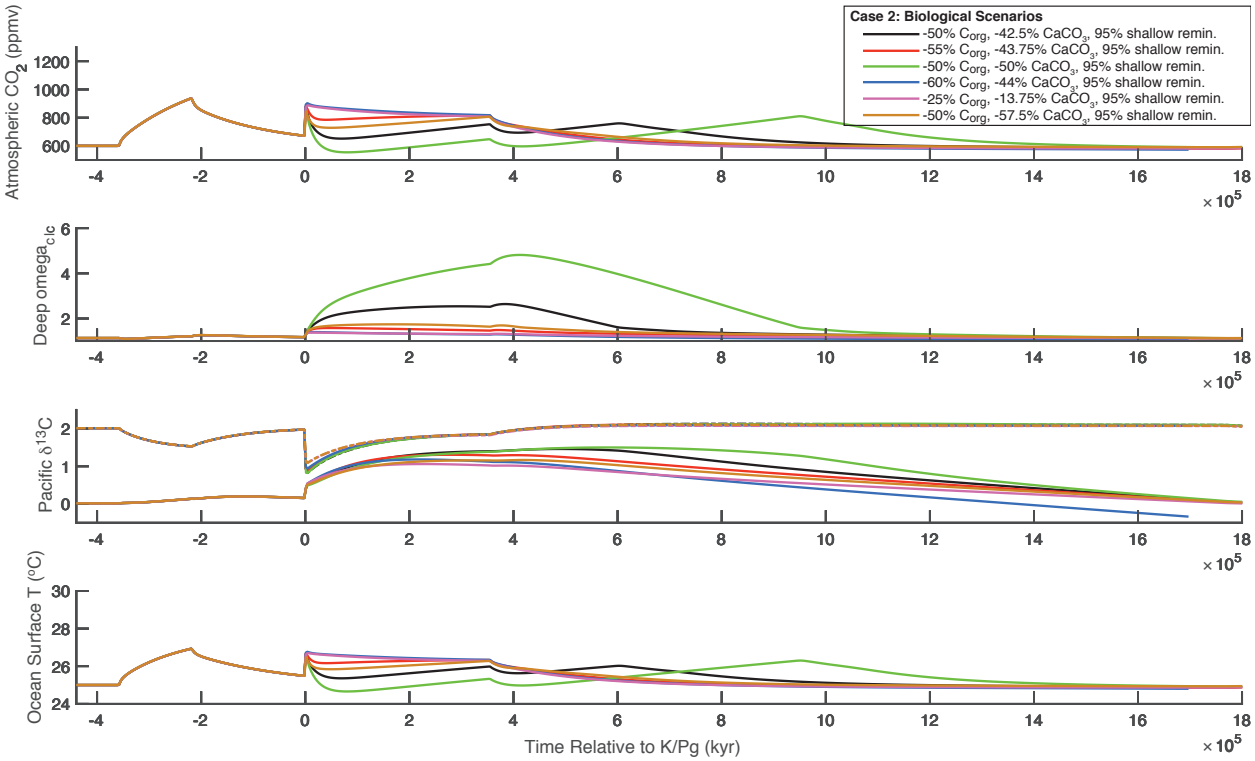

Fig. S26.

Biological scenarios explored for Case 2. All tests assume enhanced remineralization rates after the K/Pg (95% shallow water remineralization post-K/Pg and 75% prior to the K/Pg), impact degassing, and a Case 2 outgassing scenario with high Deccan emissions and a climate sensitivity of 3 ˚C/doubling. Biological scenarios explored include a 25-60% reduction in organic carbon export and somewhere between no change and a 25% increase in the $CaCO_3$ to C_{org} export ratio. Even though we explored only increases in the $CaCO_3$ to C_{org} export ratio (to minimize the oversaturation of the deep ocean) these scenarios resulted in dramatic declines in the total export flux of carbonate to the deep sea (between 13.75% and 57.5% reduction in the $CaCO_3$ export flux) due to the reduction of organic carbon. The best scenario in terms of minimizing the increase in deep sea carbonate saturation and the decrease in earliest Paleocene temperatures was a 50% reduction in C_{org} with a 15% increase in the $CaCO_3$:C_{org} rain ratio (42.5% reduction in $CaCO_3$ export flux).

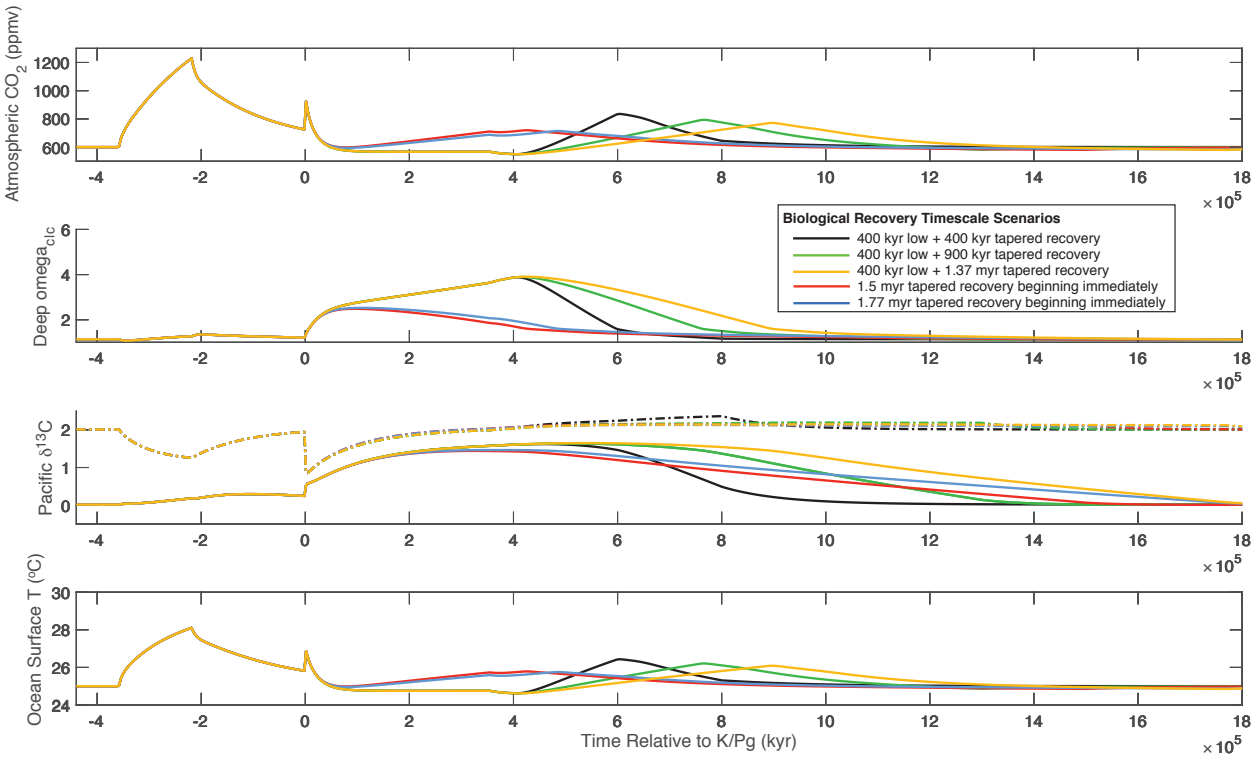

Fig. S27.

Biological recovery timescales explored as detailed in the plot legend. All tests assume enhanced remineralization rates after the K/Pg (95% shallow water remineralization post-K/Pg and 75% prior to the K/Pg), impact degassing, and a Case 1 outgassing scenario with high Deccan emissions, a climate sensitivity of 3°C/doubling, a 50% reduction in organic carbon export, and a 42.5% reduction in $CaCO_3$ export flux.

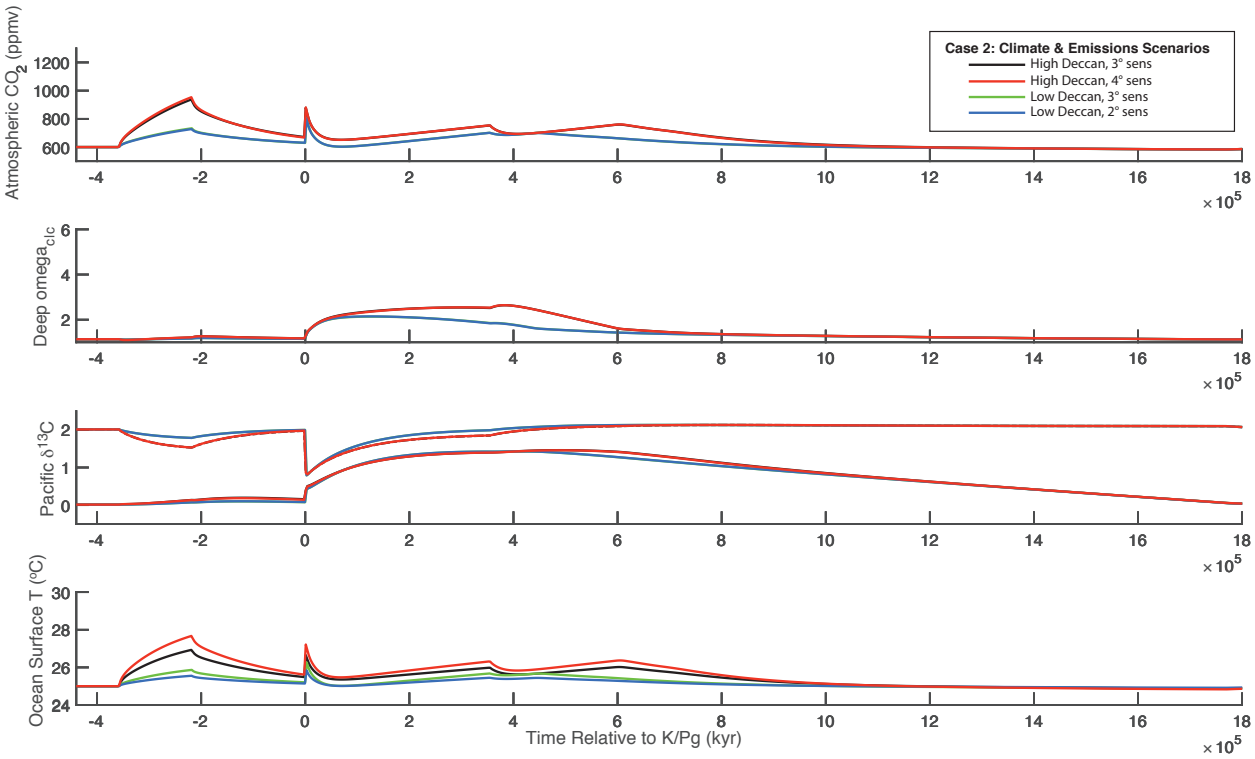

Fig. S28.

Effect of volcanic outgassing volume and climate sensitivity on Case 2 simulation behavior. Case 2 conditions shown here include a Case 2 outgassing scenario and a biological change scenario of a 50% reduction in C_{org}, a 15% increase in the $CaCO_3$:C_{org} rain ratio, and an increase in shallow water remineralization from 78% to 95% at the K/Pg. High and low Deccan outgassing scenarios assume upper and lower end-estimates for total volcanic outgassing volumes of 4090 (low) versus 9545 (high) Gt C and 3200 (low) and 8500 (high) Gt S (*10, 12*)), with climate sensitivities (°C/doubling) as described in the legend.

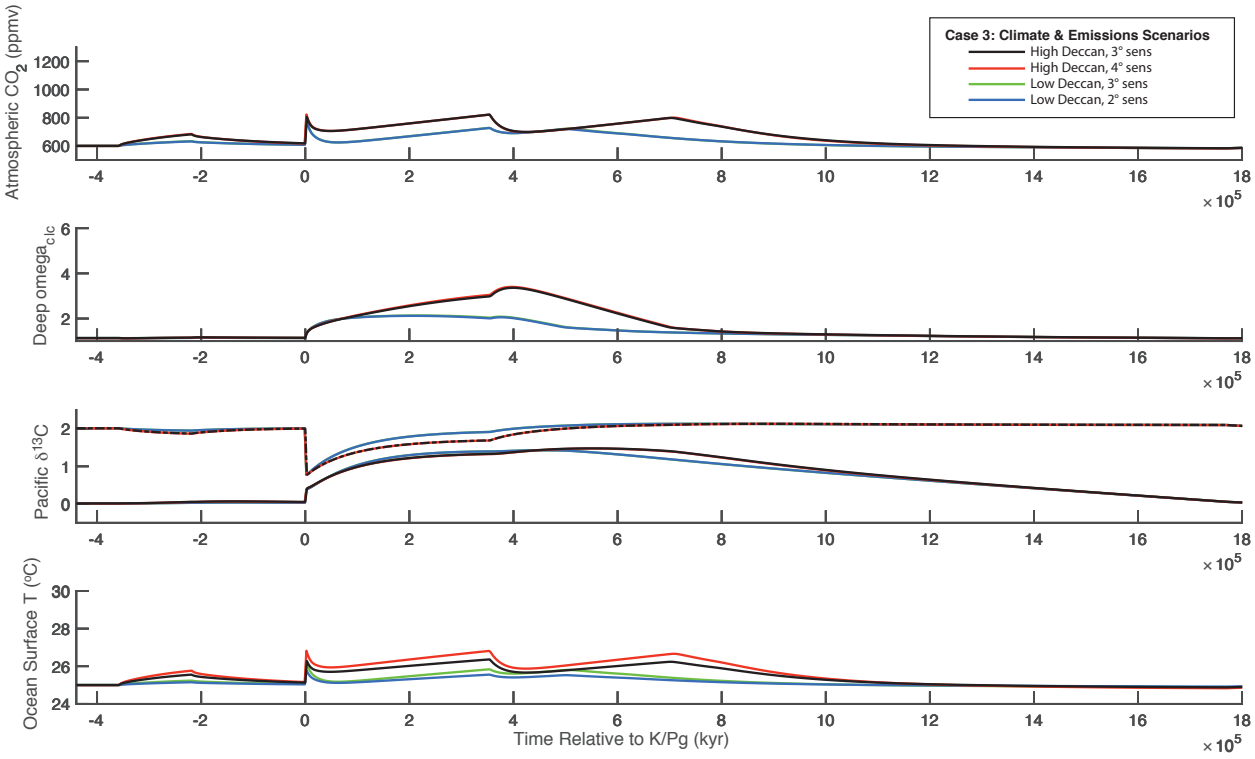

Fig. S29.

Effect of volcanic outgassing volume and climate sensitivity on Case 3 simulation behavior. Case 3 conditions shown here include a Case 3 outgassing scenario and a biological change scenario of a 50% reduction in C_{org}, a 15% increase in the $CaCO_3$:C_{org} rain ratio, and an increase in shallow water remineralization from 78% to 95% at the K/Pg. High and low Deccan outgassing scenarios assume upper and lower end-estimates for total volcanic outgassing volumes of 4090 (low) versus 9545 (high) Gt C and 3200 (low) and 8500 (high) Gt S (*10, 12*)), with climate sensitivities (°C/doubling) as described in the legend.

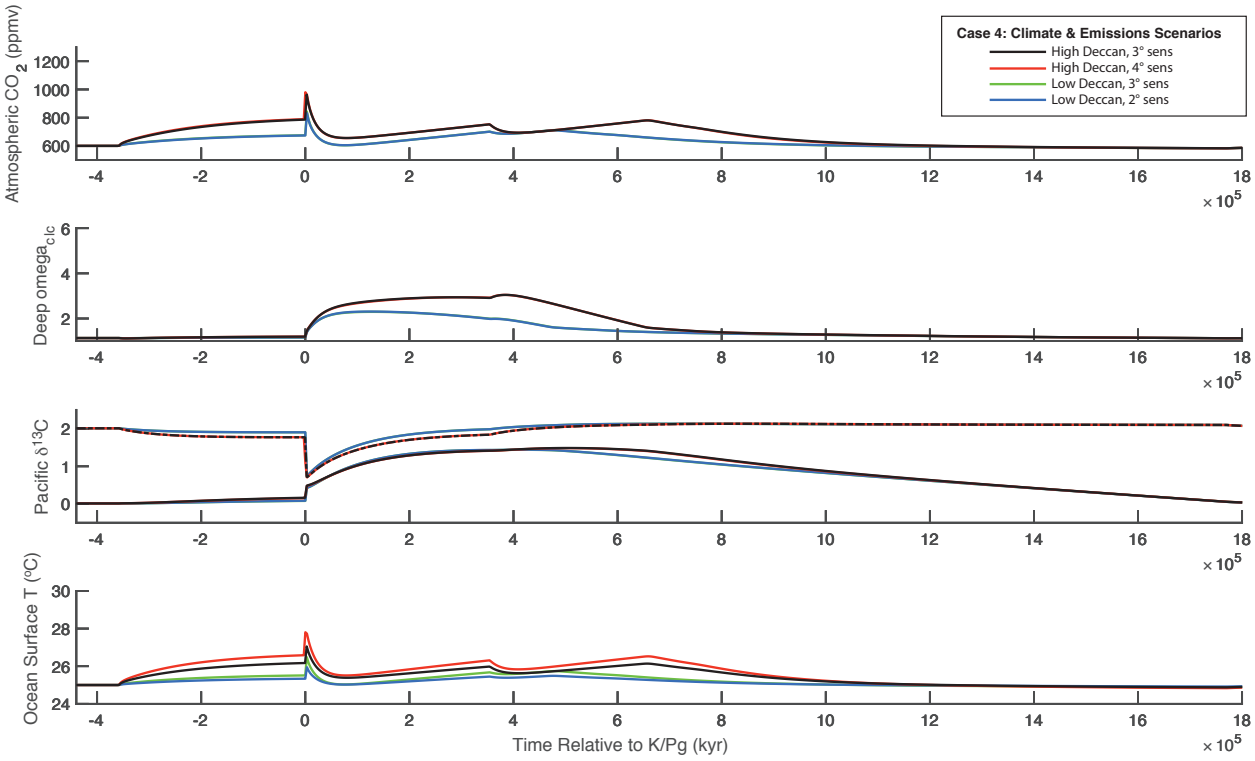

Fig. S30.

Effect of volcanic outgassing volume and climate sensitivity on Case 4 simulation behavior. Case 4 conditions shown here include a Case 4 outgassing scenario and a biological change scenario of a 50% reduction in C_{org}, a 15% increase in the $CaCO_3$:C_{org} rain ratio, and an increase in shallow water remineralization from 78% to 95% at the K/Pg. High and low Deccan outgassing scenarios assume upper and lower end-estimates for total volcanic outgassing volumes of 4090 (low) versus 9545 (high) Gt C and 3200 (low) and 8500 (high) Gt S (*10, 12*)), with climate sensitivities (°C/doubling) as described in the legend.

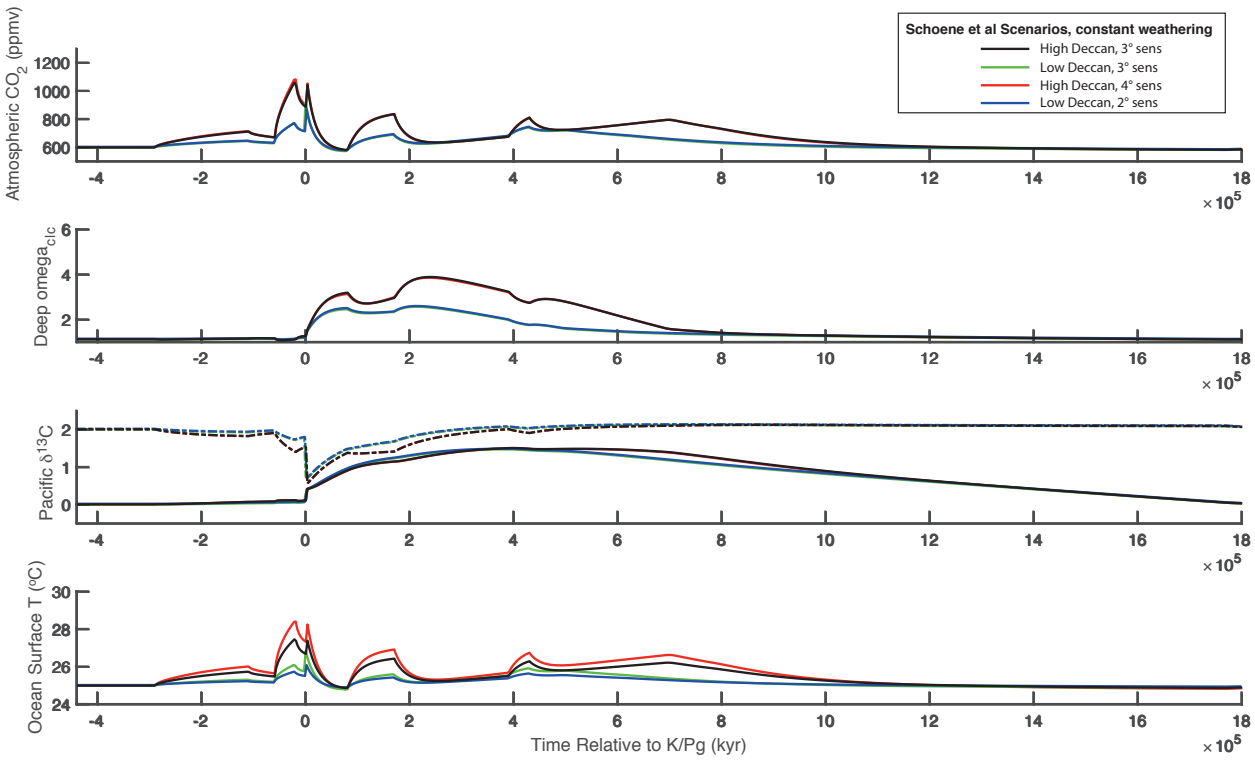

Fig. S31.

Effect of volcanic outgassing volume and climate sensitivity on outgassing scenarios following lava emplacement in Schoene et al. (*8*), using the same weathering feedback common to all other simulations. The Schoene degassing timing and volumes are as follows: 20% of emissions between 290 and 110kyr before the boundary, 35% of emissions between 60 and 20kyr before the boundary, 35% of emissions between 80 and 170 kyr after the boundary, and 10% of emissions between 390 and 430kyr after the boundary. All other factors are as in other simulations: a biological change scenario of a 50% reduction in C_{org}, a 15% increase in the $CaCO_3$:C_{org} rain ratio (a 42.5% $CaCO_3$ export flux reduction), an increase in shallow water remineralization from 78% to 95% at the K/Pg, and high and low Deccan outgassing scenarios assuming upper and lower end-estimates for total volcanic outgassing volumes of 4090 (low) versus 9545 (high) Gt C and 3200 (low) and 8500 (high) Gt S (*10, 12*)), with climate sensitivities (˚C/doubling) as described in the legend.

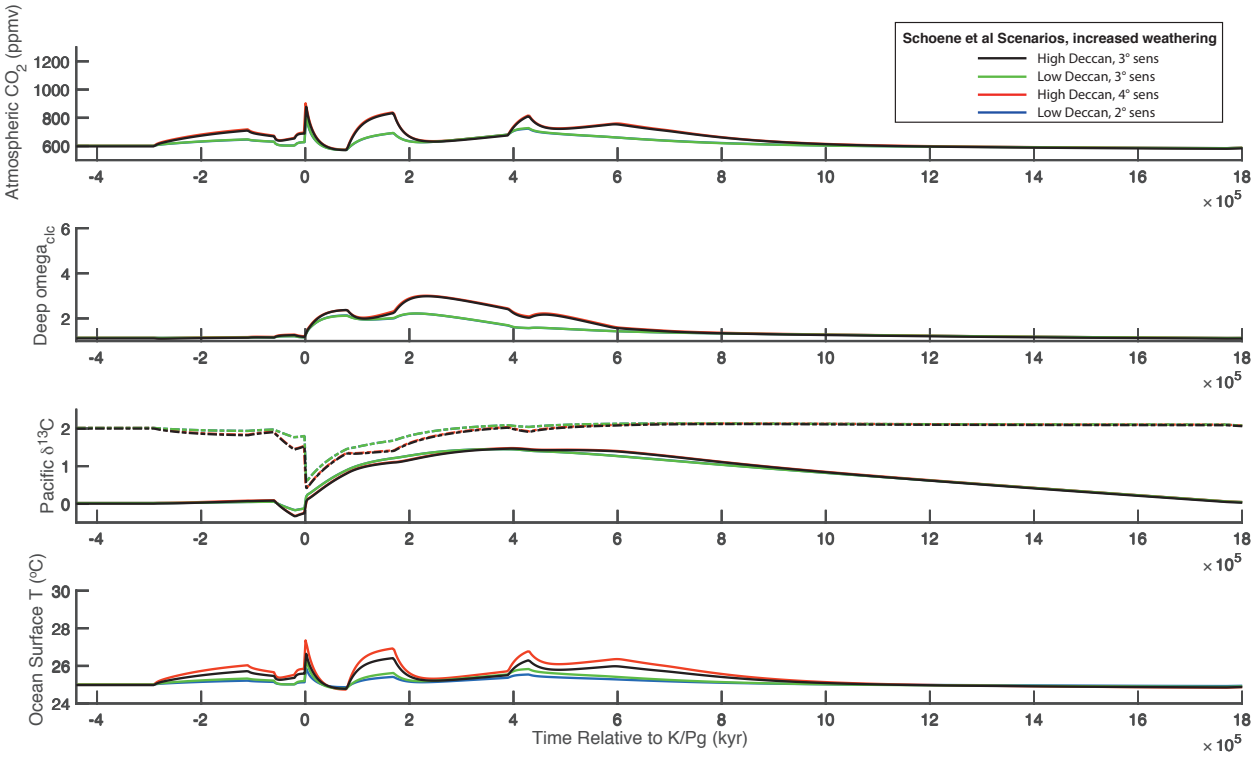

Fig. S32.

Effect of volcanic outgassing volume and climate sensitivity on outgassing scenarios following lava emplacement in Schoene et al. (*8*), with silicate weathering doubled during the latest-Cretaceous Deccan pulse to negate warming during that interval. The Schoene degassing timing and volumes are as follows: 20% of emissions between 290 and 110kyr before the boundary, 35% of emissions between 60 and 20kyr before the boundary, 35% of emissions between 80 and 170 kyr after the boundary, and 10% of emissions between 390 and 430kyr after the boundary. All other factors are as in other simulations: a biological change scenario of a 50% reduction in C_{org}, a 15% increase in the $CaCO_3$:C_{org} rain ratio (a 42.5% $CaCO_3$ export flux reduction), an increase in shallow water remineralization from 78% to 95% at the K/Pg, and high and low Deccan outgassing scenarios assuming upper and lower end-estimates for total volcanic outgassing volumes of 4091 (low) versus 9545 (high) Gt C and 3200 (low) and 8500 (high) Gt S (*10, 12*)), with climate sensitivities (˚C/doubling) as described in the legend.

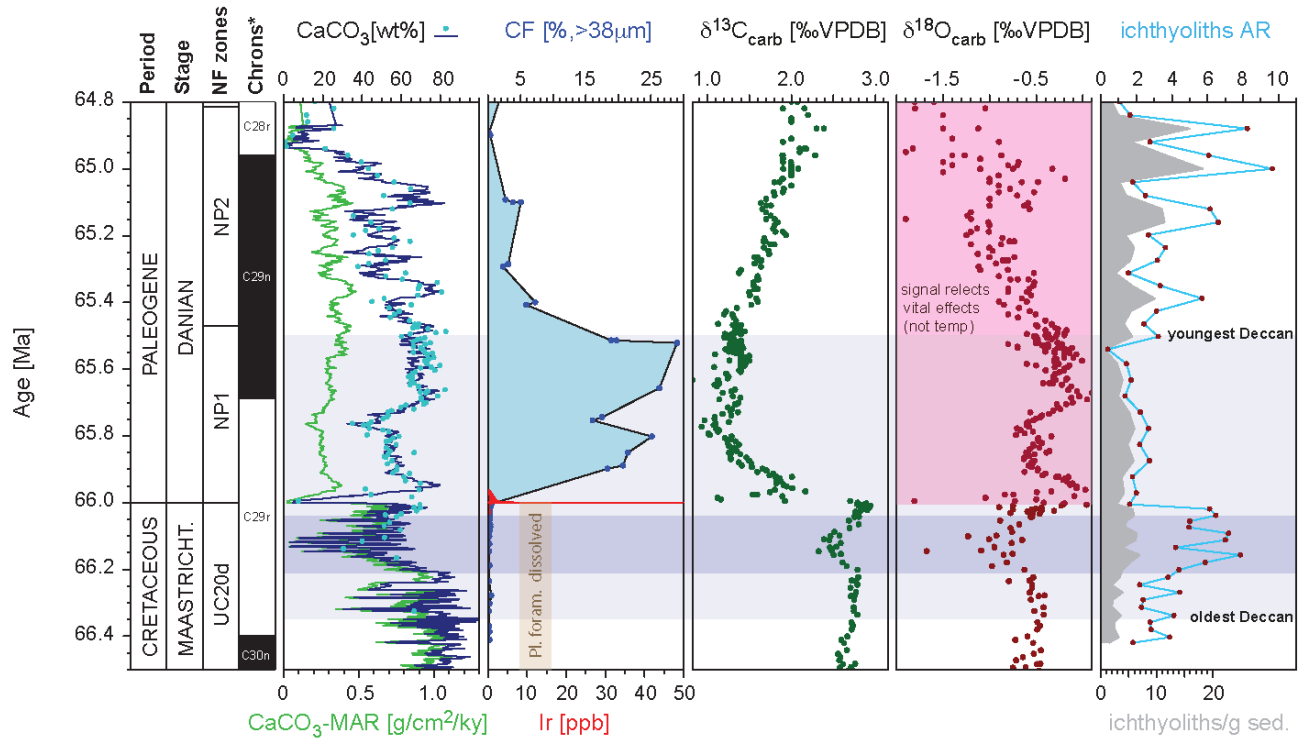

Fig. S33.

IODP Site U1403 K/Pg boundary records from Figs 2,3 with ichthyolith accumulation rate records (far right).

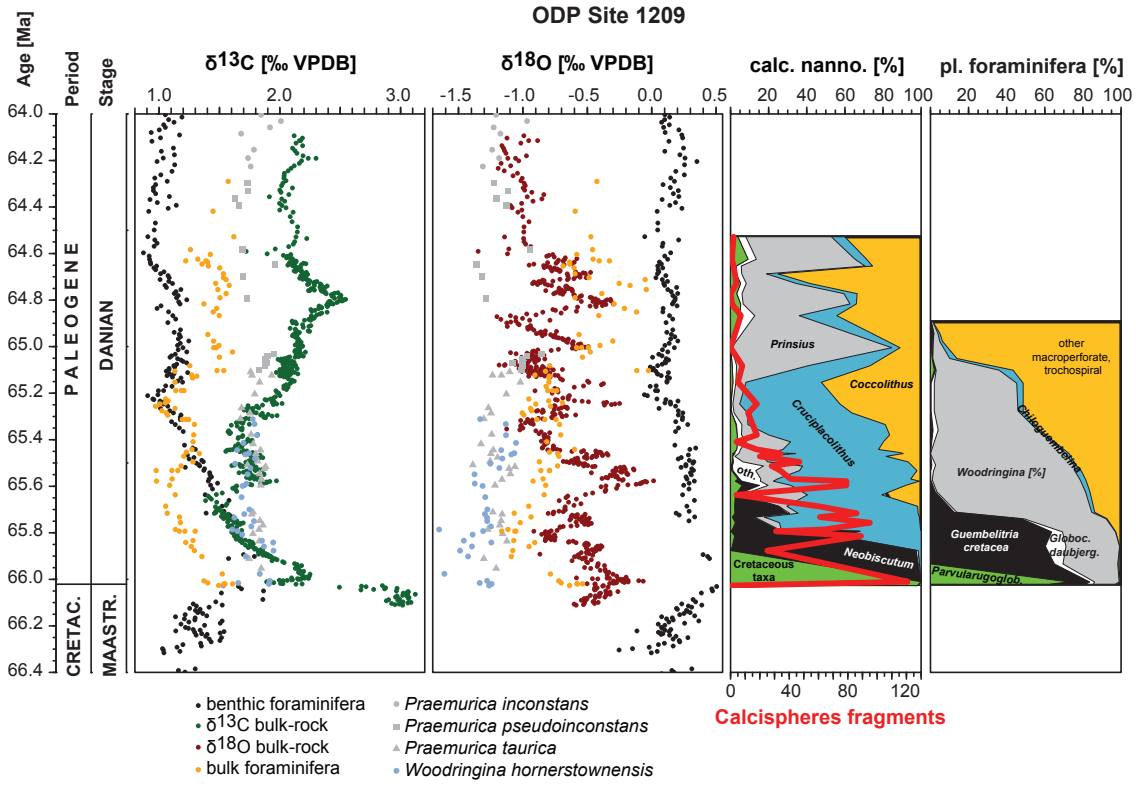

Fig. S34.

Early Paleocene carbon and oxygen isotopes in carbonates versus community turnover in nannoplankton and planktonic foraminifera at IODP Site 1209. Planktonic foraminifera data from Hull et al. (*56*).

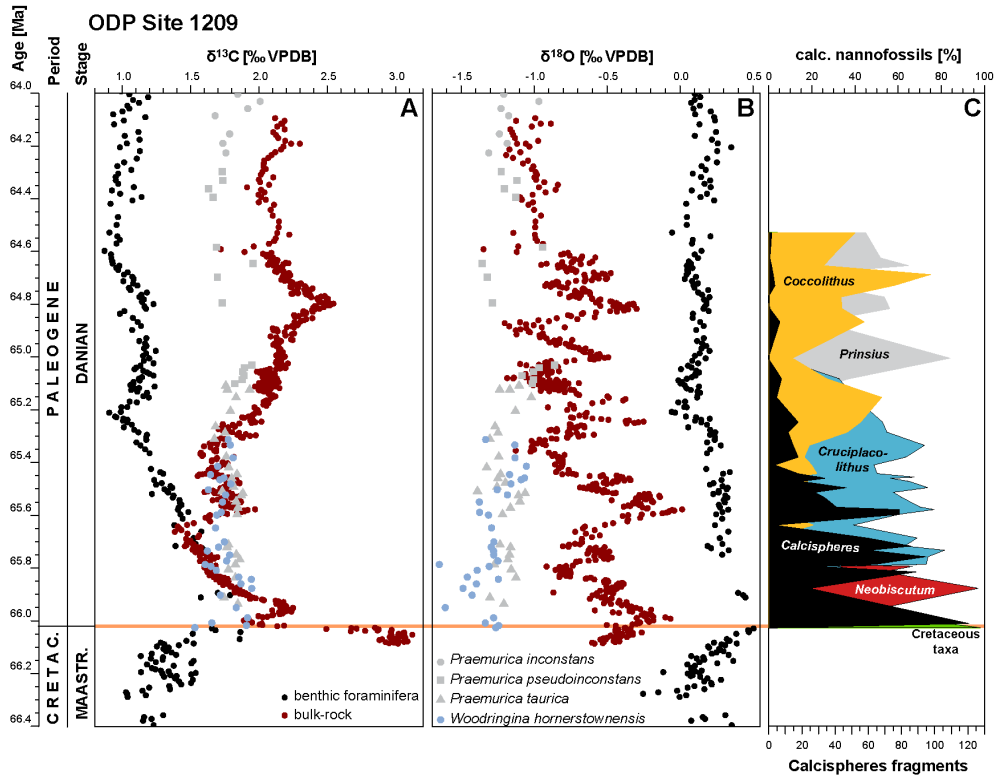

Fig. S35.

Records from ODP Site 1209, Central Pacific support patterns and inferences from IODP Site 1403. The K/Pg boundary coincides with a collapse (to inversion) in (a) the carbon isotopes of bulk carbonate (red) and planktonic foraminifera (grey, blue) relative to benthic foraminifera (black), a $\delta^{13}C$ gradient typically maintained by the biological pump. In (b) the relative stability of benthic foraminiferal (black) and planktonic foraminiferal (grey and blue) $\delta^{18}O$ (b) support the inference that earliest Paleocene of bulk carbonate (red) $\delta^{18}O$ values are strongly influenced by vital effects reflecting the rapid turnover in dominate nannofossil taxa (c) Data from Tables S11, S18 and refs. (*56, 73*).

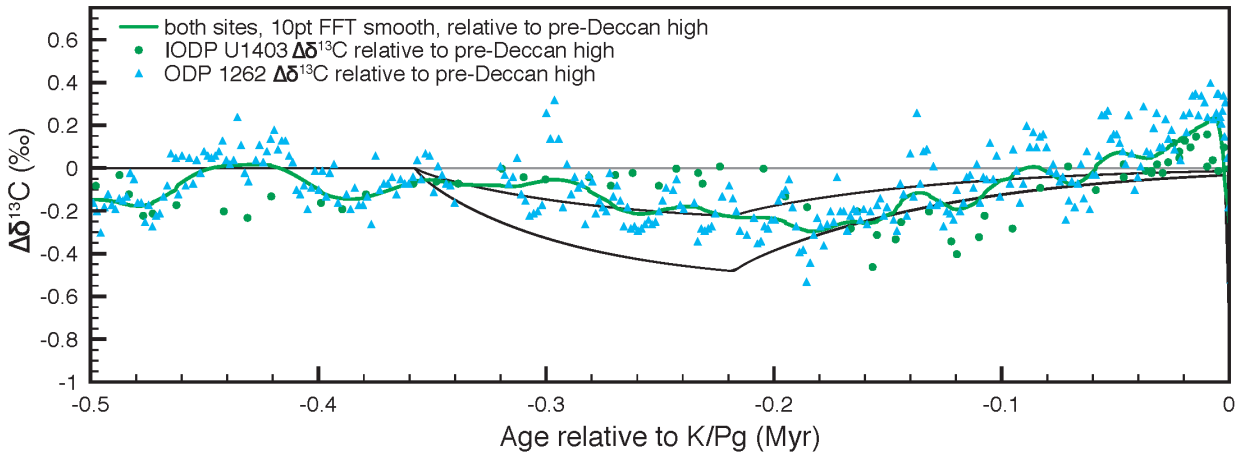

Fig. S36.

Case 2 (black lines) of surface ocean $\delta^{13}C$ (high and low emission parameterizations) compared against the bulk carbonate $\delta^{13}C$ from IODP U1403 and ODP 1262. Models and data shown relative to $\delta^{13}C$ at -0.42 Myr, in order to compare the anomaly size across the late Maastrichtian warming event.

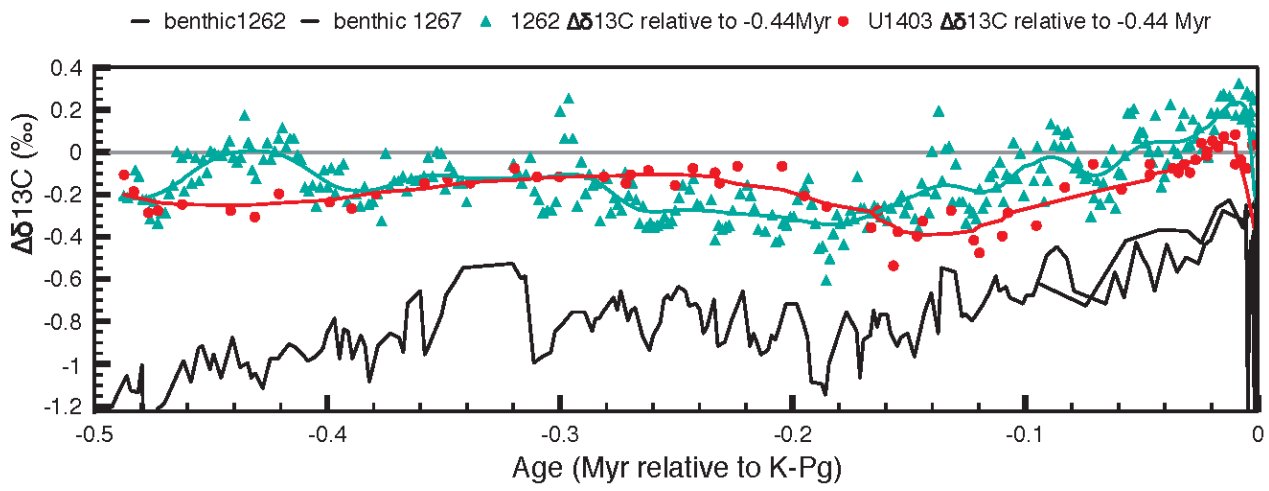

Fig. S37.

Bulk carbonate $\delta^{13}C$ from IODP U1403 and ODP 1262 and benthic foraminiferal $\delta^{13}C$ from ODP 1262 shown relative to $\delta^{13}C$ at -0.42 Myr.

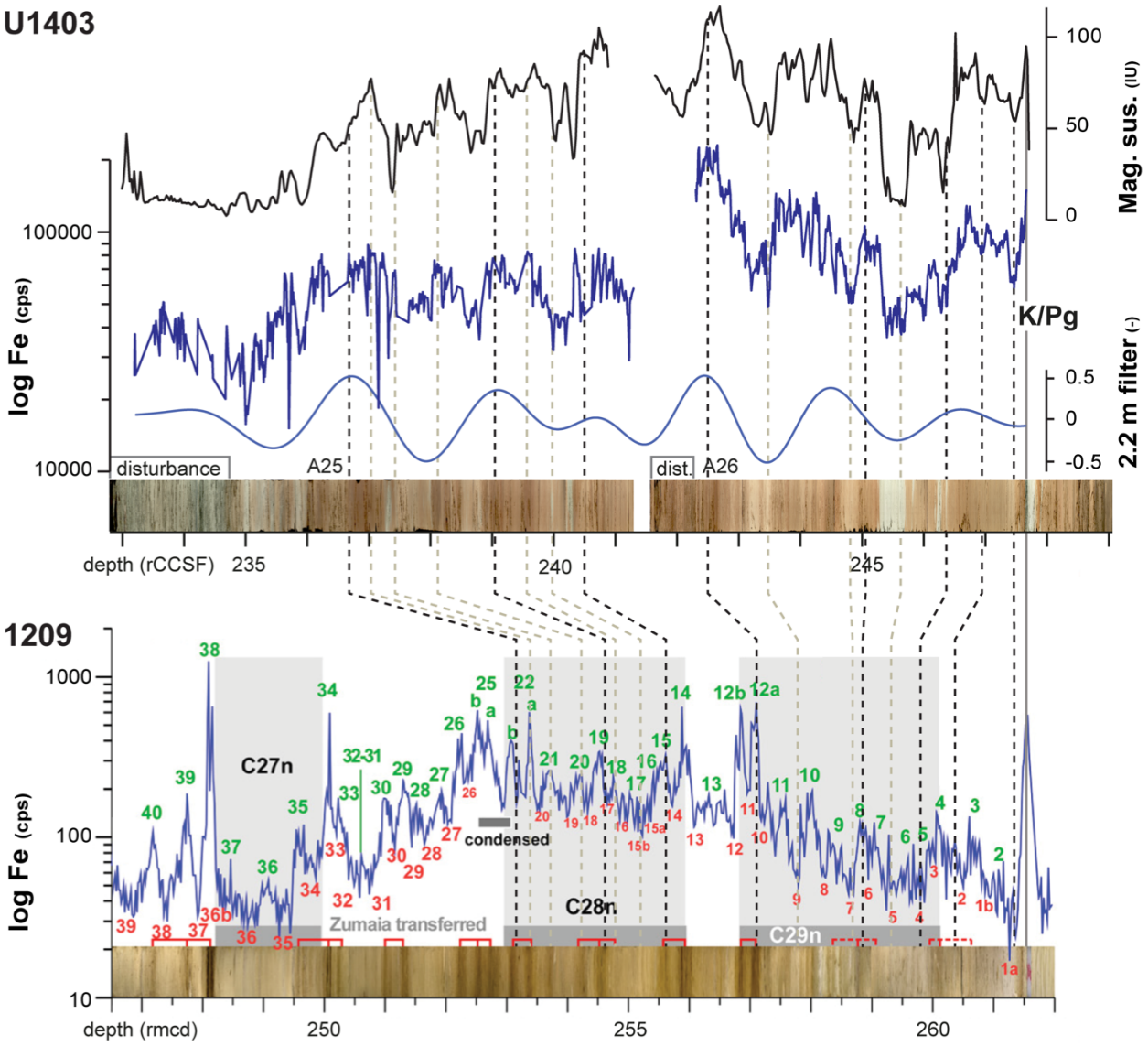

Fig. S38.

Correlation of Site U1403 to Site 1209, based on iron counts from XRF scanning (depicted as log Fe) and sedimentary banding patters, supported by magnetic susceptibility (Mag. sus.) variations. In the lower panel, red bars indicate strongly expressed bands interpreted as long-eccentricity maxima and green and red numbers mark interpreted short-eccentricity (~100 kyr) extremes (*72*). Black dashed lines indicate the tie-points used for the construction of the age model, grey dashed lines indicate additional correlation features. K/Pg: Cretaceous-Paleogene boundary.

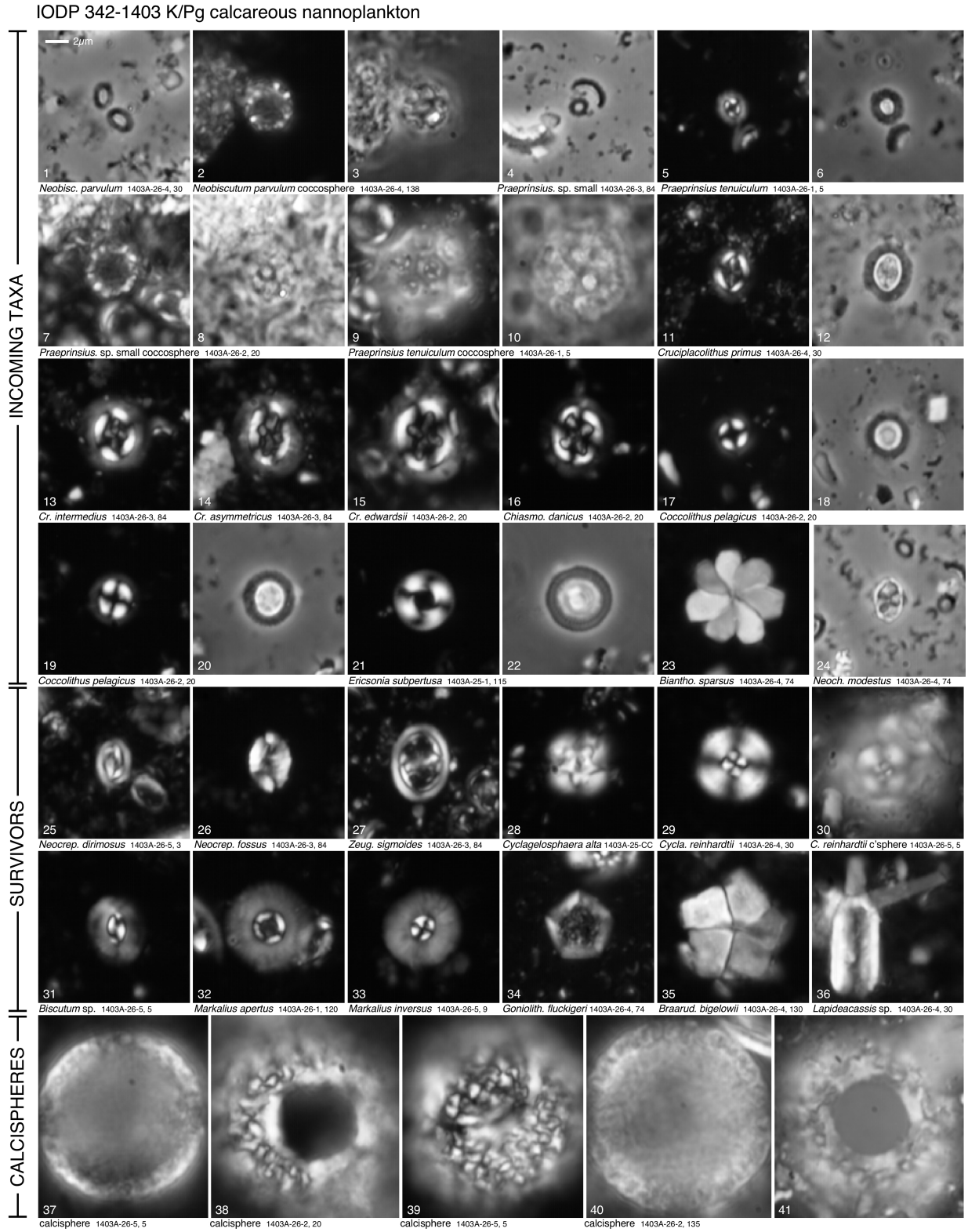

Fig. S39.

Calcareous nannofossils from IODP Site U1403.

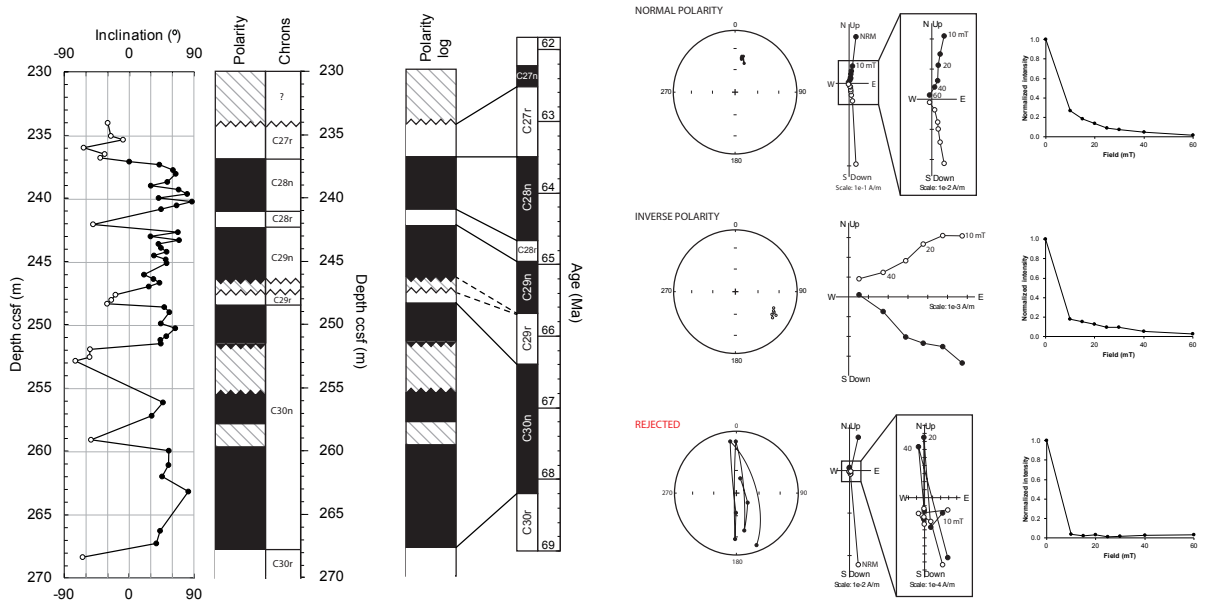

Fig. S40.

Magnetostratigraphy defined for the late Cretaceous to early Paleogene period, covering the K/Pg boundary. All three main types of data obtained to define the magnetostratigraphy are represented, for each one the Zijderveld plot, the stereographic projection and the magnetization versus alternating field are given.

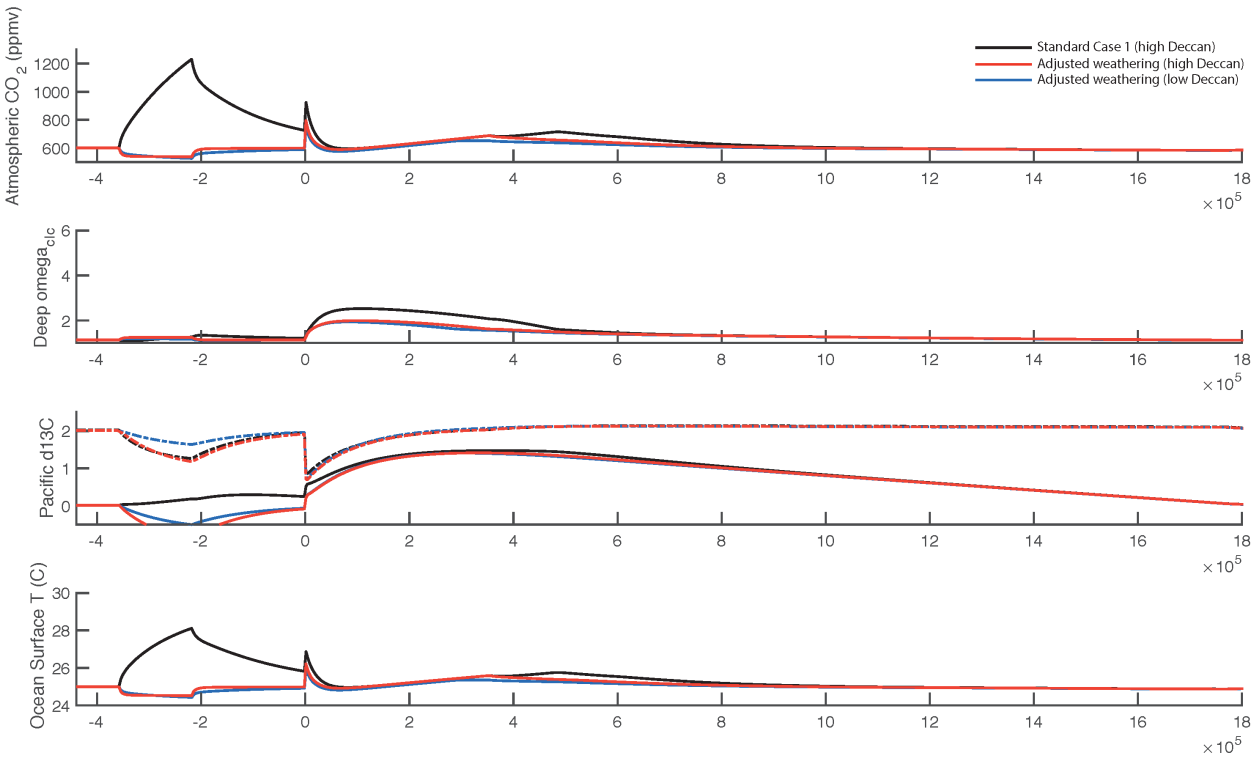

Fig. S41.

Case 1 (black line) run with the high silicate weathering hypothesized by Schoene et al. 2019 (ref. (*8*) and effects explored in Fig. S32) in red (high Deccan outgassing parameterization) and blue (low Deccan outgassing parameterization). The weathering response is so marked that it results in lower atmospheric CO_2 levels during the outgassing event (rather than higher).

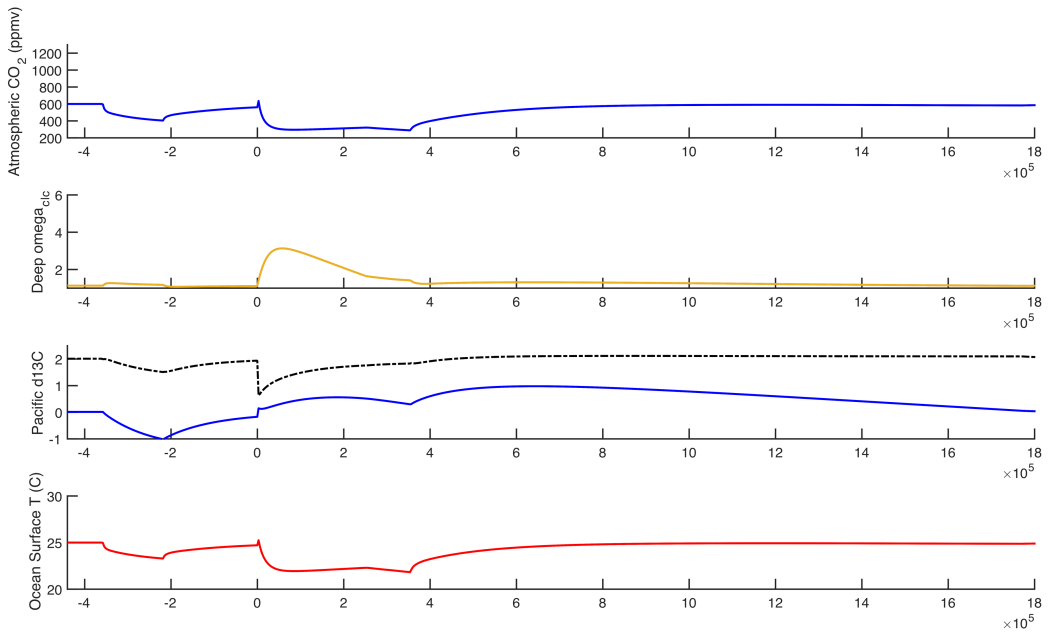

Fig. S42.

The high silicate weathering parameterization could not be fully tested for Case 2 because it crashed the model in the low Deccan outgassing scenario, presumably because atmospheric CO_2 was reduced to zero. Shown above is Case 2 run with the high silicate weathering hypothesized by Schoene et al. 2019 (ref. (58) and effects explored in Fig. S32) for the high Deccan outgassing parameterization.

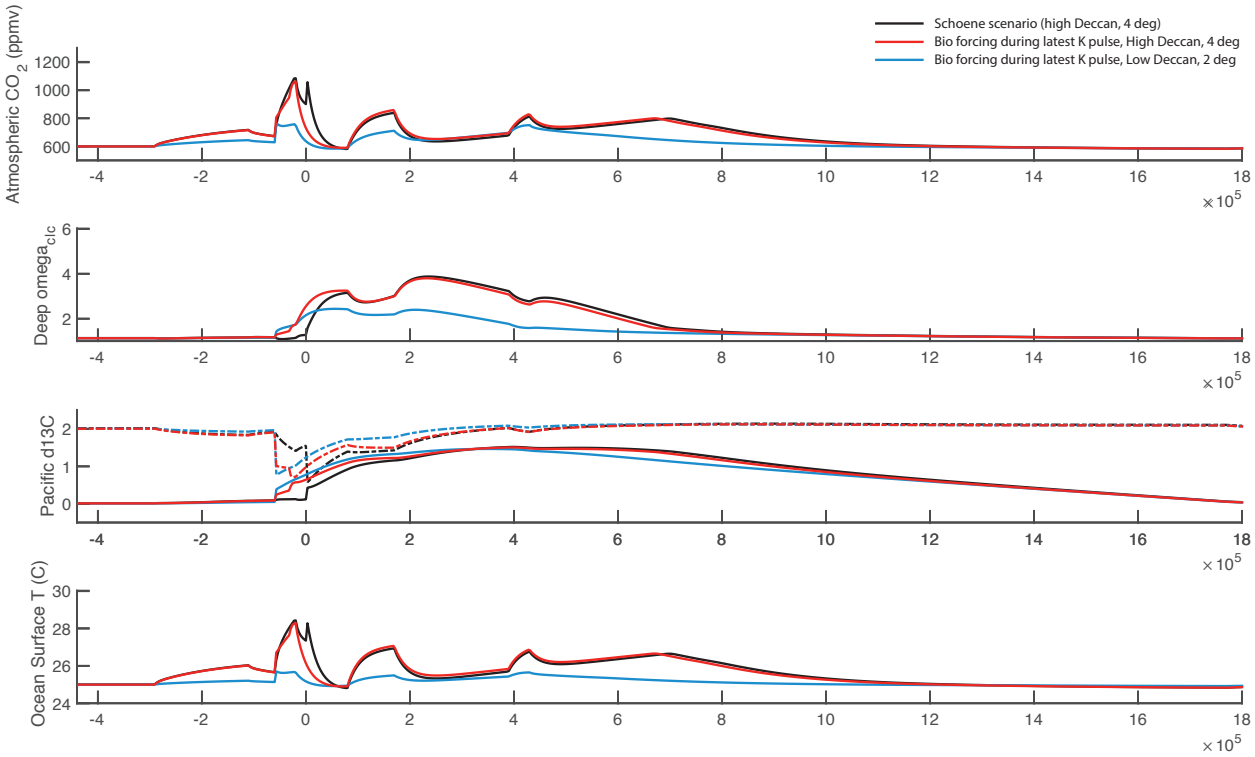

Fig. S43.

Here we impose the biotic changes of the K/Pg mass extinction (a biological change scenario of a 50% reduction in C_{org}, 42.5% $CaCO_3$ export flux reduction, an increase in shallow water remineralization from 78% to 95%) during the latest Cretaceous pulse of Deccan Trap emplacement hypothesized by Schoene et al. (*8*). The standard high emissions Case 3 is shown in black, and the high and low outgassing parameterizations of Case 3 with this early biotic change is shown in red and green respectively. These model runs show that this scenario (a biotic crash in response to outgassing, well-prior to impact) would be readily apparent in the fossil record as it would result in the collapse of surface to deep ocean $\delta^{13}C$ gradients prior to the deposition of impact ejecta.

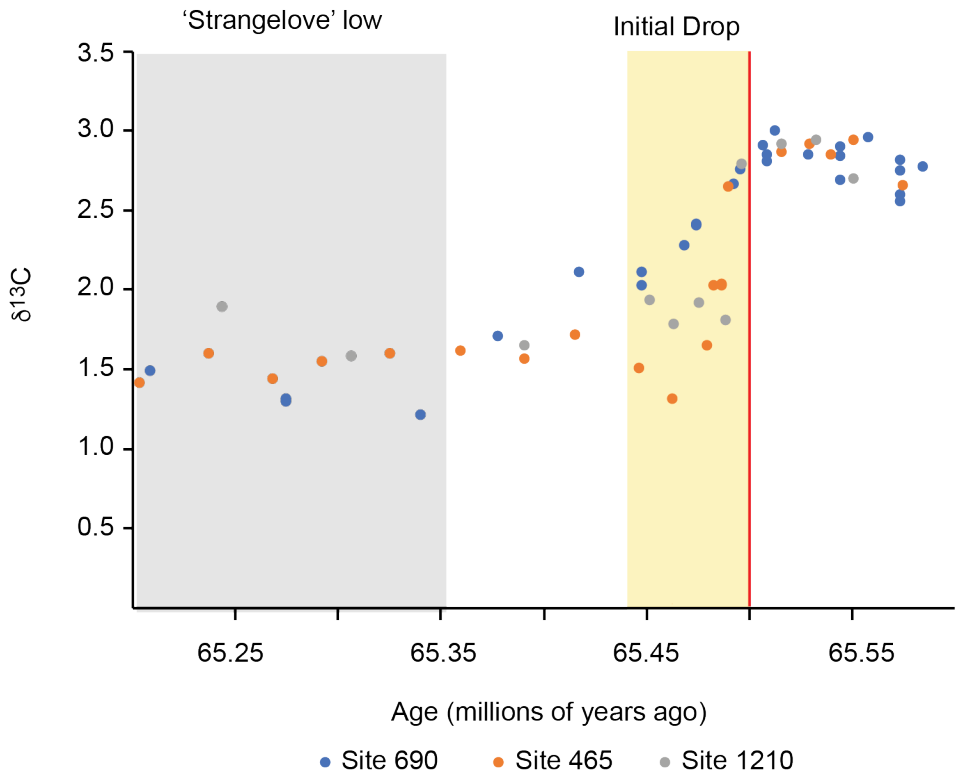

Fig. S44
Evidence for the double drop in $\delta^{13}C$ in the earliest Paleocene is apparent in the published bulk carbonate records of Alegret et al (*28*), shown above on the age scale used in that paper (K/Pg age=65.5 Myr, red line).

Table S1.

Diagnosing a mass extinction requires identifying an exogenous trigger, linking that trigger to a (set of) environmental effects, and linking those environmental effects to extinction. Here we provide an overview of some of the relevant literature regarding the timing, environmental effects, biotic effects of Deccan volcanism and the Chicxulub impact, and the ties between these events and the K/Pg mass extinction. This is not an exhaustive review of all literature published on the latest Maastrichtian and earliest Paleocene.

Topic	Evidence for…	Relevant Findings…	Citation	Ref.
Eruptions	**Deccan:** Volcanism	Vast majority of Deccan flows dated to magnetochron C29R using U-Pb dating (Schoene et al 2015, 2019), K-Ar dating (Chenet et al. 2007), and Ar-Ar dating (Renne et al. 2015; Sprain et al. 2019). Early estimates of a <1Myr duration coinciding with C29R based on paleomagnetism, palynology and K-Ar dating (Courtillot et al. 1986), were subsequently debated (Duncan & Pyle 1988, Courtillot et al. 1988, and many others) and only recently confirmed with advanced absolute dating techniques in Schoene et al. 2015, 2019, Renne et al. 2015, and Sprain et al. 2019. Notably, earlier idea of three pulses of volcanism (i.e., Chenet et al. 2007) is not supported by recent U-Pb and Ar-Ar work.	Duncan & Pyle 1988; Chenet et al. 2007; Courtillot et al. 1986, 1988; Renne et al. 2015; Schoene et al. 2015, 2019; Sprain et al. 2019	(*8, 9, 11-13, 210-212*)
		Magnetochron C29r dated to last ~587 ka (Sprain et al. 2018) using Ar-Ar dating, revising the shorter estimates of Sprain et al. (2014), but within error of the GTS 2012 estimate. Key ages from Sprain et al. (2018) include C30n/C29r reversal ~66.311 Ma, K/Pg ~66.052 Ma, C29r/C29n ~65.724 Ma. Accordingly, the C29R Cretaceous duration is ~259+/-52 kyr and Paleocene duration is ~328+/-15kyr (Sprain et al. 2018)	Sprain et al. 2014, 2018; Gradstein et al. 2012	(*7, 50, 213*)
		Paleomagnetic secular variation shows short duration of individual flows, increasing potential for environmental effects	Chenet et al. 2008	(*214*)
		Outgassing potential calculations of Deccan traps for SO_2, CO_2, Cl	Chenet et al. 2009; Self et al. 2006, 2008	(*10, 171*) (*39*)
		Hypothesized link between impact and major Deccan eruptions based on eruptive volumes; new eruptive volume estimates provided.	Richards et al. 2015	(*15*)
		Constrains majority of Deccan volcanism to post-K/Pg using Ar-Ar dating	Renne et al. 2015; Sprain et al. 2019	(*9, 13*)
		Constrains majority of Deccan volcanism to two pulses (one ~30kyr pre-K/Pg, the second ~100 post-K/Pg) using U-Pb dates and lava volume estimates	Schoene et al. 2019	(*8*)
Weathering	**Deccan:** Volcanism	Decrease in Sr isotope ratios ($^{87}Sr/^{86}Sr$) coincident with $\delta^{18}O$ anomaly in the Cretaceous interval of C29R; attributed to Deccan related increase in weathering	Vonhof & Smit 1997; Olsson et 2002	(*154, 215*)

		Declines in osmium isotope ratios in magnetochron C29r in sites globally suggestion large scale change in terrestrial weathering with Deccan flood basalt volcanism	Ravizza & Peucker-Ehrenbrink 2003; Paquay et al. 2008; Robinson et al. 2009	(*46, 117, 118*)
		Erosional history of Deccan Traps from structure of Western Ghats	Widdowson & Cox 1996	(*216*)
		Mercury anomaly in Bidart, France, coincides w/pre-K/Pg cooling interval (w/evidence for dissolution of foraminifera); and see subsequent discussions	Font et al. 2016a,b; Smit et al. 2016	(*217-219*)
		Increased Sr/Ca ratios in latest Maastrichtian (last 200 kyr) perhaps due to increased chemical weathering during Late Maastrichtian warming and cooling in Elles, Tunisia	Stüben et al. 2003	(*220*)
Pre-K/Pg	**Deccan:** Inferred Environment effect	8°C summer temp decrease (Montana)	Tobin et al. 2014	(*141*)
		7°C temp rise and fall (North Dakota)	Wilf et al. 2003	(*136*)
		Clay mineralogical evidence for aridity and alkaline conditions (Deccan volcanic sediments)	Samant et al. 2014	(*221*)
		'Mock aridity' due to volcanically influence local climate (Deccan sedimentary sequence)	Khadkikar et al. 1999	(*222*)
		Intense precipitation inferred from geochemistry of inter-basaltic bole beds (Deccan Traps)	Ghosh et al. 2006	(*223*)
		Longer warm interval (>2 Myr span) pre-K/Pg suggested by Seymour Island flora; cool early Paleocene suggested by flora directly countered by evidence of no K/Pg temperature change in organic geochemical proxies	Bowman et al. 2014; Kemp et al. 2014	(*224, 225*)
		High latitude warming (Southern Ocean) coincident with Cretaceous interval of C29r	Tobin et al. 2012	(*140*)
		Antarctic sea ice indicator (dinoflagellate species) present in Maastrichtian is significantly reduced during last ~2 Myr before the K/Pg (indicative of significant climatic warming; matches longer interval of warmth in Seymour Island plants as well)	Bowman et al. 2013; Bowman et al. 2014	(*224, 226*)
		Warming (or low oxygen) in Nye Kløv, Denmark inferred from bryozoan colonial morphology; matches stable carbon and oxygen records. In both cases the warming occurs right up to boundary (no subsequent cooling)	O'Dea et al. 2011; Barrera and Keller 1994	(*227, 228*)
		Regional evidence (biomarker, geochemical and benthic foraminiferal assemblage) towards anoxia in NW Pacific, New Zealand, and a few Tethyan sections	Kajiwara & Kaiho 1992; Kaiho et al. 1999; Alegret & Thomas 2005; Mizukami et al. 2013	(*229-232*)
		Late Cretaceous warming in magnetochron C29r of ~2-3°C (also called the 'late Maastrichtian warming event')	Henehan et al. 2016; Westerhold et al. 2011; Li &	(*41-44, 73*)

			Keller 1998; Barnet et al. 2018, 2019	
		Increased oligotrophy suggested by nannoplankton assemblage structure (North Pacific and other sites)	Thibault & Gardin 2010	(*177*)
		Deep sea carbonate undersaturation; minor surface ocean acidification based on fragmentation and wt % $CaCO_3$ records coincident with warming in open ocean sites (Henehan et al. 2016); dissolution in Dameron et al. 2017 at Shatsky Ruse begins far earlier (~68-66 Ma) due to local changes in water masses	Henehan et al. 2016; Dameron et al. 2017	(*41*)
		Surface ocean acidification based on relative abundance of robust tests and fragmentation during pre-K/Pg cooling at two Tethyian sites (Punekar et al. 2016) (i.e., opposite signal as in Henehan et al. 2016; Dameron et al. 2017)	Punekar et al. 2016	(*233*)
		Decrease in detrital magnetite in Bidart, France section hypothesized to be consequence of acid rain during Deccan volcanism Phase 2 (i.e., the Late Cretaceous warming interval)	Font et al. 2014	(*234*)
		Late Cretaceous warming of similar scale to Paleocene warming events; all (including Late Cretaceous warming) hypothesized to be linked to LIPs	Barnet et al. 2019	(*43*)
Post-K/Pg	**Deccan:** Hypoth. Environment effect	No warming or cooling detected with timing of lava emplacement (discussed in Sprain et al. 2019; shown here) in global compilation (but see fish teeth in MacLeod et al. 2018; leaf margins in Lyson et al. 2019)	This study; Sprain et al. 2019; MacLeod et al. 2019; Lyson et al. 2019	(*9, 52, 235*)
Pre-K/Pg	**Deccan:** Inferred Biotic effect	Plant immigration and increased diversity (North Dakota) in response to climate change	Wilf et al. 2003; Wilf & Johnson 2004	(*136, 150*)
		Minor mammalian changes with climate (body size, relative abundance, evenness) (Montana)	Wilson 2005, 2014	(*180, 236*)
		Declining evenness and diversity in salamander and salamander-like species, Hell Creek Formations (Montana)	Wilson et al. 2014	(*179*)
		Palynoflora community turnover (Deccan volcanic sediments; pre- vs. intertraps)	Samant & Mohabey 2009; Samant & Bajpai 2005	(*237, 238*)
		Molluscan diversity may have declined in the late Maastrichtian (Bay of Biscay)	Marshal & Ward 1996	(*239*)
		Local extinction in Antarctic Seymour Island Section of marine macro-invertebrates coincident with C29R warming; but subsequently debated (Witts et al. 2016; Tobin 2017)	Tobin et al. 2012; Zinsmeister et al. 1989; Witts et al. 2016; Tobin 2017	(*54, 55, 140, 240*)
		Pole-ward migration of warm water planktic foraminifera into shelf setting at Bass River section coincident with C29r warming, followed by subsequent return to approximately pre-event conditions	Olsson et al. 2001	(*176*)

		Morphological changes in bryozoans at Nye Kløv; inferred link to environmental change	O'Dea et al 2011	(*227*)
		Uppermost Maastrichtian temporary very low diversity shark faunas at Stevns Klint (not extinction, species reappear in the Danian) attributed to regional environmental change (sea level postulated)	Adolfssen & Ward 2014	(*241*)
		Calcareous nannoplankton assemblage change (North Pacific and other sites); peaked with temperature anomaly and recovered before K/Pg boundary	Thibault & Gardin 2010; Thibault & Husson 2016	(*177, 242*)
		Geographic range extensions (poleward migration) in planktonic foraminifera; recovers before K/Pg boundary	Olsson et al. 2001; Kucera & Malmgren 1998	(*175, 176*)
		Increased ichthyolith (fish teeth and scale) accumulation rates at one site (Site U1403) and possibly Gubbio but not others (Sites 596, 886, 1209)	this study; Sibert et al. 2014	(*84*)
		Reduced population abundance of deep dwelling planktonic foraminifera in coastal sites; widespread dwarfing of planktonic foraminifera during warming event	Abramovich & Keller 2003; Keller & Abramovich 2009; Abramovich et al. 2010	(*181-183*)
		Coastal assemblages of planktonic foraminifera dominated by species thought to be opportunistic and/or tolerant of low oxygen during warming event; reduced diversity in Tethys	Abramovich & Keller 2002, Keller 2003, Keller & Pardo 2004; Pardo & Keller 2008; Abramovich et al. 2010	(*183-185, 243, 244*)
		Low diversity in Tethys but for longer interval (>1 million years of latest Maastrichtian)	Keller 2004	(*245*)
Post-K/Pg	**Deccan:** Inferred Biotic effect	The immediate aftermath of the K/Pg mass extinction is similar to that of many extinctions, with low diversity (e.g., Coxall et al. 1998), high dominance and high turnover communities (e.g., Hull et al. 2011; Bown 2005; Alvarez et al. 2019), unusually functioning ecosystems (D'Hondt et al. 1998, Henehan et al. 2016; Alvarez et al. 2019) persisting for hundreds of thousands to millions of years (e.g., Hull 2015). Although this interval is often attributed to the loss of species and the time to re-evolve species and functional communities (Hull 2015), the duration could be paced by volcanic outgassing (as is hypothesized for the P/T). At present, there is not clear tie (or mechanism) for this in the early Paleocene but few studies have looked.	Alvarez et al. 2019; Coxall et al. 2006; Hull et al. 2011; Bown et al. 2005; D'Hondt et al. 1998; Henehan et al. 2016; Hull 2015	(*94*) (*56, 80*) (*53*) (*41*) (*200, 246*)
Pre-K/Pg	**Deccan:** Elevated extinction?	Not elevated in mammals (Montana)	Wilson 2005, 2014	(*180, 236*)
		Not elevated in plants (North Dakota)	Wilf et al. 2003; Wilf & Johnson 2004	(*136, 150*)

		Not elevated in turtles	Holroyd et al. 2015	(*247*)
		Not elevated (nor gradually declining in the Late Cretaceous) in dinosaurs	Pearson et al. 2002; Fastovsky et al. 2004; Wang & Dodson 2006; Sheehan et al. 1996; 2000	(*248-252*)
		Gradual decline in dinosaur richness (in the last several million years in Barrett et al. 2009; so longer than Deccan volcanism); disputed and countered by analysis of Brusatte et al. (2015) and Chiarenza et al. 2019	Archibald 2012; Barrett et al. 2009; Brusatte et al. 2015; Chiarenza et al. 2019	(*253-256*)
		No evidence from rudists; counters earlier interpretations based on different stratigraphic interpretations and patterns in the mostly incomplete carbonate platform sequences	Steuber et al. 2002; Schlüter et al. 2008; Steuber & Schlüter 2012	(*257-259*)
		No evidence in nannoplankton	Bown 2005; Pospichal 1994, 1996; Thibault & Husson 2016	(*57, 194, 242, 260*)
		No evidence in foraminifera	this study; Arenillas et al. 2000a,b, 2002; Norris et al. 1999; Huber et al. 2002; MacLeod et al. 2007	(*261-266*)
		Various single site studies of planktonic foraminifera have reported elevated extinctions prior to the impact (Tunisia: Keller 1988; Keller & MacLeod 1996; Keller 1998; Site 525: Li & Keller). The local nature of these patterns (regardless of whether they reflect local extinctions or local stratigraphic biases) have subsequently been revealed by other studies by the same set of authors (Punekar et al. 2014) that show survivorship up to the K/Pg boundary of the same species at other sites; and by studies of sample biasing by other authors on the same site (Arenillas et al. 2000a,b; Tunisia) showing sudden and catastrophic extinction. Keller et al. (2018) discuss local extinctions (and large scale faunal changes) but not global extinctions prior to the K/Pg boundary; in line with the discussion provided here.	Keller 1988; Keller and MacLeod 1996; Keller et al. 2018; Punekar et al. 2014	(*178, 267-271*)
Impact	**Chicxulub:** Impact	Reviews of K/Pg impact tracers (many hundreds of sites)	Smit 1999; Claeys et al.	(*5, 106,*

	2002; Schulte et al. 2010; Hull et al. 2011	*172, 272*)
Iridium and osmium anomalies at the K/Pg boundary (North Dakota, Hell Creek and Fort Union formations); reviewed in Nichols and Johnson (2008)	Johnson et al. 1989; Nichols & Johnson 2008; Moore et al. 2014	(*273*) (*274, 275*)
Mineralogical evidence (shocked quartz & stishovite) for impact at the K/Pg boundary (Western Interior, US)	Bohor et al. 1984; McHone et al. 1989	(*276, 277*)
Hiatuses common across shallow water K/Pg boundary sections (attributed to tsunami, slumping, and others)	Smith et al. 1996; Olsson et al 2002; Meyers & Peters 2011	(*104, 154, 278*)
Tsunami deposits around Caribbean, Gulf Coast, and possibly in Western Interior	Bourgeois et al. 1988; Smit et al. 1996, Tada et al. 2002; DePalma et al. 2019	(*103-105, 279*)
Iridium layers in multiple sections coincident with K/Pg boundary	Bourgeois et al. 1988; Miller et al. 2010	(*105, 280*)
Mineralogical evidence (shocked quartz) for impact at the K/Pg boundary (global)	Bohor et al. 1987; Alegret et al., 2005	(*281, 282*)
Mass wasting deposits in the Caribbean and along the Gulf Coastal Plain, triggered by impact associated ground motion (i.e., earthquakes) at the K/Pg boundary	Bralower et al. 1998; Norris et al. 2000; Soria et al. 2001; Alegret et al. 2002, 2005; Denne et al. 2013	(*100, 102, 282-285*)
Impact ejecta (a few examples) at the K/Pg boundary	Schulte et al. 2010; Sigurdsson et al. 1997; Norris et al. 1999; Alegret et al. 2005; MacLeod et al. 2007	(*5, 264, 266, 282, 286*)
Osmium anomalies at the K/Pg boundary	Ravizza et al. 2003; Paquay et al. 2008; Robinson et al. 2009	(*46, 117, 118*)

		Iridium anomalies (a few examples) at the K/Pg boundary	Alvarez et al. 1980; Michel et al. 1981; Alvarez et al. 1990	(*1, 287, 288*)
		K/Pg boundary ashes and impact markers (tektites) dated via Ar-Ar dating to be synchronous within error	Renne et al. 2013	(*14*)
K/Pg (& Post)	**Chicxulub:** Infer. Environment effect	Possible paleobotanical evidence for impact winter (Wyoming) (disputed by Nichols 1992, Hickey and McWeeny 1992, and McIver 1999 among others)	Wolfe 1991; Nichols 1992, Hickey & McWeeny 1992; McIver 1999	(*289-292*)
		Paleobotanical evidence for ecosystem turnover coincident with boundary (regionally: Saskatchewan, Canada; North Dakota, Montana, Wyoming US), including fern spike, and globally	Tschudy et al. 1984; Nichols 1990; Johnson & Hickey 1990; Nichols & Fleming 1990; Nichols et al. 1992; McIver 1999; Johnson 2002; Nichols 2002; Wilf & Johnson 2004; Nichols & Johnson 2008; Vadja & Bercovici 2014	(*150, 275, 292-300*)
		All lower Danian deposits in the Western Interior in 'coal-bearing, fluvial or paludal deposition settings'(Nichols 1990), with evidence for increased 'wetness' (Sweet & Braman 1992) across the boundary	Nichols 1990; Sweet & Braman 1992	(*294, 301*)
		Impact winter suggested by TEX_{86}, with sea surface cooling of as much as 7°C in Brazos River, Texas	Vellekoop et al. 2014	(*24*)
		Decrease in export productivity suggested along New Jersey margin	Esmeray-Senlet et al. 2015	(*132*)
		Decreased oxygenation in northwestern Pacific (sulfur isotopic evidence) and some localities in the Tethys	Kajiwara & Kaiho 1992; Coccioni & Galeotti 1994	(*230, 302*)
		Biological selectivity suggestive of impact-associated ocean acidification (Alegret et al. 2012); boron isotope evidence of ocean acidification (Henehan et al. 2019	Alegret et al. 2012; Henehan et al. 2019	(*23, 28*)
		Multiple lines of evidence (carbonate geochemistry, other productivity proxies, boron isotopes, and biomarkers) for a decline in productivity or the efficiency of the biological pump (estimates of the magnitude, geography, and timing vary)	Zachos et al. 1989; D'Hondt et al. 1998; Sepulveda et al. 2009, 2019; Hull &	(*23, 48, 53, 85, 123, 303*)

			Norris 2011; Henehan et al. 2019	
		Prolonged (>500,000 yr) alkalinity pulse; benthic foraminiferal effects of increased alkalinity	Henehan et al. 2016; Alegret & Thomas 2013	(*41, 129*)
		Conflicting estimates of atmospheric CO_2 and CO_2 change at boundary from boron isotopes and leaf stomata. Most recent leaf stomata research (Milligan et al. 2019) estimates atmospheric CO_2 of ~875 ppm during post-impact fern spike interval (~10^3 years after impact) and increase of ~250 ppm from the late Cretaceous. Boron isotopes suggest up to ~1,600ppm within 102 years of the impact, but from a latest Cretaceous baseline of ~900ppm (Henehan et al. 2019).	Henehan et al. 2019; Milligan et al. 2019	(*23, 304*)
K/Pg (& Post)	**Chicxulub:** Inferred Biotic change	Extinction selectivity in mammals (against large carnivores and herbivores) suggest loss of primary productivity; recovery fueled by immigration	Sheehan & Hanson 1986; Robertson et al. 2013; Wilson 2013	(*31, 305, 306*)
		Wide-spread evidence for floral turnover at the boundary, including a fern spike throughout the Western Interior and globally	Tschudy et al. 1984; Nichols 1990; Johnson & Hickey 1990; Fleming & Nichols 1990; Nichols & Fleming 1990; Nichols et al. 1992; Sweet & Braman 1992; McIver 1999; Johnson 2002; Nichols 2002; Wilf & Johnson 2004; Nichols & Johnson 2008; Vadja & Bercovici 2014	(*293, 294, 301, 307*) (*150, 275, 292-300*)
		Persistent (>2 million year) shift in floral ecological strategies (North Dakota)	Blonder et al. 2014	(*308*)
		Drastic turnover in leaf miners (insect trace fossils) and decoupling of leaf and miner diversity (Western Interior N. America)	Donovan et al. 2014; Wilf et al. 2006	(*309, 310*)
		Recovery of plant community structure in phases. Initial communities of opportunistic 'bloom' taxa (i.e., fern/spore spike) replaced by pioneer communities, and then by diverse communities including new taxa.	Vajda & Bercovici 2014; Nichols & Johnson 2008	(*275, 300*)

Note: temporal resolution is too low to distinguish late Maastrichtian warming from impact at boundary. As summarized in Kiessling & Baron-Szabo (2004): corals dominate reefs in Paleocene in contrast to Late Cretaceous (Kiessling et al. 1999); greater percentage of corals are reef associated in Paleocene; K/Pg mass extinction event is only mass extinction with a major drop in reefal carbonate at the stage level (Fluegel & Kiessling 2002); geography and timing of earliest Paleocene reefs indicates latest first appearance in Caribbean (although data is sparse) closer to impact site (Kiessling & Claeys 2001); numerous survivor clades through early Danian (i.e., prolonged turnover).	Fluegel & Kiessling 2002; Kiessling et al. 1999; Kiessling & Claeys 2001; Kiessling & Baron-Szabo 2004	(*311-314*)
Increase in epifaunal echinoderm fecal pellet abundance in New Jersey and Turkey	Miller et al. 2010	(*280, 315*)
Mollusk ecological trait change suggestive of low-productivity driven extinction and uncoordinated recovery of functional diversity (Western Argentina)	Aberhan et al. 2007	(*30*)
Dwarfing in Danian echinoderms (sister taxa comparison)	Smith & Jeffery 1998	(*316*)
Persistent shift in molluscan community functional ecology across the K/Pg: increase in deposit feeding & increase in predators and predator-resistance post-K/Pg (Aberhan & Kiessling 2015); basic patterns of functional turnover reflected in high southern latitudes as well (Stilwell 2003)	Aberhan & Kiessling 2015; Stilwell 2003	(*317, 318*)
No change in the proportion of the two main clades of incrusting bryozoans in US and Danish sections suggesting no long-term crash in productivity or inadequate understanding of the inter-clade differences; also, no dwarfing in zooids or colonies	Sogot et al. 2013; Sogot et al. 2014	(*319, 320*)
Regional benthic 'dead zones' with low abundance and/or benthic impoverished faunas. Known from Danish and Caribbean sections.	Hakansson & Thomsen 1999; Hansen et al. 2004	(*321, 322*)
Calcareous red algae in Pyrenean Basin show prolonged/delayed recovery of species richness extending until the early Thanetian; shallow water (tropical affinity) species had greatest extinction rates and the clades dominating immediately post-K/Pg in reef assemblages typically occur in deep water/cryptic habitats today. Depth selectivity of extinctions observed across sites (i.e., Aguirre et al. 2000).	Aguirre et al. 2007; Aguirre et al. 2000	(*323, 324*)
Changed pelagic community structure (relative abundance amongst microfossil taxa)	Hull et al. 2011; Sibert et al. 2014	(*56, 84*)
Blooms of aberrant planktonic foraminifera in Tunisia in early Danian	Arenillas et al. 2018	(*325*)
Low richness, short-lived successive communities in planktonic foraminifera and nannoplankton (global, early Danian)	Gerstel & Thunell 1986; Gerstel et al. 1987; Jiang et al. 2010; Fuqua et al. 2008,	(*57, 76, 77, 89, 95*)

			Pospichal 1996	
		Dominance of 'disaster' or 'opportunistic' taxa in the earliest Paleocene (global)	Jiang et al. 2010	(*77*)
		Turnover in benthic community structure suggesting regional heterogeneity in detrital flux to the benthos (increased in some regions, declined in others)	Alegret & Thomas 2005, 2007, 2009; Alegret 2007; Alegret et al. 2012	(*28, 83, 232, 326, 327*)
		Siliceous plankton bloom (New Zealand)	Hollis et al. 1995	(*328*)
		Low latitude incursions of high latitude dinoflagellates; dinoflagellate community turnover	Brinkhuis & Zachariasse 1988; Vellekoop et al. 2015	(*157, 329*)
		Short (~1,000-10,000 years) reduction in primary productivity (Sepúllveda et al. 2009, 2019), with longer term (>1 Myr) changes to the biological pump (D'Hondt et al. 1998, Zachos et al. 1989, Hull et al. 2011; Alegret et al. 2012; Esmerary-Senlet et al. 2015; Birch et al. 2016)	Zachos et al. 1989; D'Hondt et al. 1998; Sepulveda et al. 2009, 2019; Hull et al. 2011; Alegret et al. 2012; Esmeray-Senlet et al. 2015; Birch et al. 2016	(*48, 49, 53, 85, 123, 132, 303*)
K/Pg (& Post)	**Chicxulub Impact:** Elevated extinction?	Review: dinosaur extinction coincident with impact (no support for Cretaceous decline in diversity)	Brusatte et al 2015	(*255*)
		Dinosaur extinction coincident with K/Pg impact	Sheehan et al. 1991; Sheehan et al. 2000	(*330, 331*)
		Mass bird extinction at K/Pg boundary (western N. America)	Longrich et al. 2011	(*332*)
		Mass snake and lizard extinction at the K/Pg (N. America)	Longrich et al. 2012	(*333*)
		75% Mammalian extinction in Hell Creek Formations across the K/Pg (Montana)	Wilson 2014	(*180*)
		22% species-level extinction in salamander & salamander-like species across the K/Pg, Hell Creek Formations (Montana)	Wilson et al. 2014	(*179*)
		30% (palynological) to 57% (megafloral types) floral extinction across the KPg (North Dakota)	Johnson & Hickey 1990; Wilf & Johnson 2004; Johnson 1992	(*150, 295, 334*)
		Elevated extinction of specialized and moderately specialized insect trace fossils across the KPg	Labandeira et al. 2002; Donovan et al. 2014	(*309, 335*)

~75% species extinction in shelly marine invertebrates	Jablonski 1991; Barnosky et al. 2011	(*336, 337*)
45% extinction in scleractinian corals, with particularly high extinction levels in photosymbiotic, colonial (particularly with high corallites), and narrow ranged taxa	Kiessling & Baron-Szabo 2004	(*311*)
36% generic-level extinction in sea urchins, with selectivity by clade, feeding strategy, and endemic regionality (in narrow-ranging clades)	Smith & Jeffery 1998	(*316*)
63% generic-level bivalve extinction; with molluscan extinction intensity declines with latitude if rudists are considered (high latitudes have less extinction)	Raup & Jablonski 1993; Vilhena et al. 2013	(*338, 339*)
Rudist bivalve extinction (100%) consistent with catastrophic extinction coincident with K/Pg boundary in stratigraphically complete sections.	Steuber et al. 2002; Schlüter et al. 2008; Steuber & Schlüter 2012	(*257-259*)
34% generic/45% species-level extinction in Neoselachian sharks with greater losses in shallow water species. Greater extinction amongst skates and rays.	Kriwet & Benton 2004	(*160*)
Mass extinction (100%) of all ammonites at, or just above, the K/Pg impact layer (global)	Ward & Kennedy 1993; Landman et al. 2014; Miller et al. 2010	(*192, 280, 340*)
~90% extinction in calcareous nannoplankton coincident with impact ejecta at the K/Pg boundary (global), with reworking (evidence by burrow counts and coeval iridium spread) spreading extinct taxa up-section	Bramlette & Martini 1964; Bown et al. 2004; Bown 2005; Pospichal 1990, 1994, 1996, Hull et al. 2011	(*57, 80, 172, 194, 195, 341, 342*)
~90% extinction in planktonic foraminifera coincident with impact ejecta at the K/Pg boundary (global)	Premoli-Silva & Luterbacher 1966; Smit & Hertogen 1980; D'Hondt et al. 1996; Arenillas et al. 2000	(*196, 262, 343, 344*)
Estimated 45% extinction of coral species; greater extinction amongst photosymbiotic species & colonial species; large number of failed survivors	Kiessling & Baron-Szabo 2004	(*311*)
70% species-level extinction in red calcareous algae	Aguirre et al. 2000	(*345*)
No elevation in extinction rates of fish teeth in open ocean sediments (Sibert et al. 2014), but major	Friedman 2009, 2010;	(*84, 159,*

turnover in fish community structure (Sibert & Norris 2015; and morphological radiation amongst spiny finned teleosts (Friedman 2010) following ecomorphologically selective neritic extinctions (Friedman 2009)	Sibert et al. 2014; Sibert & Norris 2015;	*346, 347*)
No elevation in extinction rates in benthic foraminifera	Culver 2003; Thomas 1990; 2007; Alegret & Thomas 2001, 2009	(*83, 348-351*)
No elevation in extinction rates in ostracods	Elwa 2002	(*352*)
No elevation in extinction rates in radiolarians	Hollis et al. 2003	(*353*)
No elevation in extinction rates in dinoflagellates	Brinkhuis & Zachariasse 1988; Brinkhuis et al. 1998	(*329, 354*)

Table S2.
Details of age models used for foraminiferal data in global compilation (Fig. 1) from deep-sea drill cores.

Site	Reference for data	Type of data	Age Model Details
ODP 1209, Shatsky Rise	(*73*), this study	Planktonic and benthic $\delta^{18}O$	In the Danian, ages are interpolated between positions of short eccentricity cycles from ref. (*72*). In the Maastrichtian, we use the age model of Westerhold et al. (*73*), Age option 3, adjusted by -0.028 Ma to fit Dinarès-Turell et al. *(72)* K/Pg boundary of 66.022 Ma.
ODP 1210, Shatsky Rise	This study	Benthic $\delta^{18}O$	In the Danian, ages are interpolated between positions of short eccentricity cycles from ref. (*72*). In the Maastrichtian, beyond the age model of ref. (*72*), ages are tuned to long eccentricity in Westerhold et al. (*73*)'s Age Option 3 at Site 1209. These were then transposed to 1210 using tie points from ref. (*68*), and adjusted by -0.0028 Ma to fit Dinarès-Turell et al.*(72)* K/Pg boundary of 66.022 Ma.
DSDP 577	(*90*)	Benthic $\delta^{18}O$	Uses linear interpolation between magnetochrons from ref. (*355*), noting the updated composite splice of ref. (*356*).
DSDP 465, Hess Rise	This study	Benthic $\delta^{18}O$	Interpolation between foraminiferal and nannofossil biostratigraphic markers from (*357, 358*), with absolute ages for datums from (*128*).
DSDP 528, Walvis Ridge	(*128*)	Benthic $\delta^{18}O$	Sedimentation rate based on thickness of Cretaceous portion of magnetochron C29r, reported by refs. (*359, 360*), and length of time in Cretaceous C29r from (*7*).
ODP 1262, Walvis Ridge	This study, (*42, 49*)	Planktonic and benthic $\delta^{18}O$	Age model from Dinarès-Turell et al. (*72*), with the Cretaceous extension of Woelders et al. (*97*).
ODP 1267, Walvis Ridge	This study	Benthic $\delta^{18}O$	Age model from Dinarès-Turell et al. (*72*).
DSDP 525, Walvis Ridge	(*44*)	Planktonic and benthic $\delta^{18}O$	Sedimentation rate based on thickness of Cretaceous portion of magnetochron C29r, reported by ref. (*359*), and length of time in Cretaceous C29r from (*7*).
ODP 690, Maud Rise	(*129, 135, 136*)	Planktonic and benthic $\delta^{18}O$	Linearly interpolated between published magnetochron boundaries (*361*), nannofossil biozones (*195*), and the K-Pg Ir spike (*362*) using updated ages for each event from GTS2012 (*7*).
ODP 1049, Blake Nose	(*130*)	Benthic $\delta^{18}O$	Linearly interpolated between magnetochrons and planktonic foraminiferal biozones from (*363*). C30n/C29r boundary from ref. (*363*), with C29r/C29n boundary placed at Dan-C2 event by analogy with other Dan-C2 sections elsewhere (*130*).
DSDP 384, J-Anomaly Ridge	(*131*)	Benthic $\delta^{18}O$	Integrated magneto-biostratigraphy of ref. (*364*), updating age tie points to GTS2012 (*7*).
ODP 174AX, Bass River	(*132, 145*)	Planktonic and benthic $\delta^{18}O$ and Mg/Ca	Age model from Esmeray-Senlet et al. (*132*).

Tables S3-S30 are found in a separate file

Table S3.
Age tie points and dates used to create new age models (via linear interpolation) for published deep-sea isotope data for the global compilation. Five deep-sea sites are tuned in (or to) the latest astronomical age model of Dinarès-Turell et al. (2014): Sites U1403, 1209, 1210, 1262, and 1267, which has a K/Pg boundary age of 66.022 Ma. Age models for all other sites (deep sea and otherwise) were generated using bio- and magnetostratigraphic tie points with ages from the Geological Timescale 2012, with a K/Pg boundary age of 66.04 Ma. To plot these data together, we use ages relative to the K/Pg boundary.

Table S4.
Global compilation of temperatures across the K/Pg boundary, with updated age models and ΔTemperatures for comparisons across realms and latitudes. Six major data types were mined to compile the first global temperature compilation spanning magnetochron C29r, and the events of the K/Pg boundary. These data types are listed adjacent to one another, as slightly different column headers are needed to describe the data. They are, from left to right: Foraminiferal $\delta^{18}O$ data, TEX_{86} data, Paleosol $\delta^{18}O$ data, Leaf margin data, Clumped isotope data, $\delta^{18}O$ shell data, Bulk Carbonate $\delta^{18}O$, Mg/Ca, and $\delta^{18}O$ teeth data. Although some temperature data is freely available from the primary sources listed, we provide the data here on updated age models (with tie points relative to GTS 2012, or, where possible, D-T et al. 2014) and as ΔTemperature (see Methods), in order to examine the change in temperature across the late Cretaceous warming event and the K/Pg boundary. Also note that in 'Foraminiferal data: Sample Type', 'benthic' refers to benthic foraminifera and 'Planktonic' refers to planktonic foraminifera. For the 'Leaf margin data', note that the relative temperatures are calculated relative to the mean of 66.03 and 66.09 Ma data points. Since not all stratigraphic tie points lend themselves to conversion to Dinares-Turrel et al. (2014)'s age model, age is also given relative to the K/Pg, and temperatures calculated using Erez and Luz (1983) and a +0.35‰ vital effect for *N. truempyi*. Biostratigraphic markers for TEX_{86} data come from the original papers. In calculating global average temperature, we excluded data from bulk carbonate $\delta^{18}O$ and the $\delta^{18}O$ of fish apatite because these values did not appear to track temperature in the extinction aftermath, likely due to the biotic discussion (see supplementary text). We have included them here for completeness.

Table S5.
Stable oxygen isotopes from ODP Site 1210 analyzed by L.A. and E.T. at the University of California Santa Cruz, Yale University and the University of Michigan. Matching carbon isotope data published in Alegret et al. (2012).

Table S6.
Stable oxygen isotopes from ODP Site 1262 analyzed by L.A. and E.T. at the University of California Santa Cruz, Yale University and the University of Michigan. Matching carbon isotope data published in Alegret et al. (2012).

Table S7.
Stable oxygen isotopes from DSDP Site 465 analyzed by L.A. and E.T. at the University of California Santa Cruz, Yale University and the University of Michigan. Matching carbon isotope data published in Alegret et al. (2012).

Table S8.
Stable oxygen isotopes from ODP Site 1267 analyzed by L.A. and E.T. at the University of California Santa Cruz.

Table S9.
Stable carbon and oxygen isotopes from bulk carbonate at ODP Site 1267 analyzed E.T. at the University of California Santa Cruz.

Table S10.
Stable carbon and oxygen isotopes from benthic foraminifera and bulk carbonate at ODP Site 1262 generated by Kroon et al (2007) and previously figured in part in Kroon et al. 2007, Barnet et al. 2017, 2019, and Birch et al. 2016, and published in part by Woelders et al. 2017.

Table S11.
Stable carbon and oxygen isotopes from ODP Site 1209 analyzed across three laboratories (Bremen=MARUM, Universitaet Bremen; SIO=Scripps Institution of Oceanography; UCSC=University of California, Santa Cruz). Four types of sample material were processed: bulk foraminifera (i.e., homogenized 38-125μm sieve size fraction), bulk (i.e., homogenized bulk sediment sample), genus-level (i.e., *Woodringina*), and species-level (species include *Praemurica taurica*, *P. pseudoinconstans*, *P. inconstans*, *P. uncinata*, and *Morozovella angulata*). Bulk and species-level data was originally collected by P.M.H. under the supervision of R.D.N. during her PhD (with UCSC samples run in the lab of J.C.Z.) and additional bulk foraminifera and *Woodringina* samples were added in collaboration with B.D., U.R., and T.W. to investigate the bulk carbonate dynamics. Source indicates the lead during these two phases of sample collection. Note that sample rmcd and rmcd adj is from Westerhold and Röhl 2006 and the age model is from Dinarès-Turell et al. (2014).

Table S12.
Bulk carbonate stable carbon and oxygen isotope analyses from Site U1403 collected by A.B. at Friedrich-Alexander Universität Erlangen-Nürnberg (AB), P.M.H. at Yale University (PMH), O.F. at the Goethe-University Frankfurt (OF), and K.M. at Kanazawa-University. Carbon and oxygen stable isotopes are reported relative to the Vienna Peedee belemnite standard (VPDB). Depths at Site U1403 are reported relative to one (or more) of three scales: the primary sample ID, the meters below seafloor of the sample (historically called msbf but known as CSF-A at Site U1403), or the revised meter composite depth scale (historically called rmcd but known as rCCSF at Site U1403) from Batenburg et al. 2017. The column 'A/W' denotes samples from the archive (A) versus working (W) half of the core. Samples listed with an age of 'NA' fell outside the applicable range of the age model, and of the figures, but are provided here without an age model for others to use in future work.

Table S13.
Weight percent coarse fraction (>38 μm sieve size fraction) of ODP Site 1267 samples prepared at Wesleyan University by E. T.

Table S14.
Weight percent coarse fraction (>63 μm sieve size fraction) of ODP Site 1262 samples generated by Kroon et al. (2007) and previously figured therein.

Table S15.
Weight percent coarse fraction (>38 μm sieve size fraction) of Site U1403 samples prepared at Yale University. Depths at Site U1403 are reported relative to one (or more) of three scales: the primary sample ID, the meters below seafloor of the sample (historically called msbf but known as CSF-A at Site U1403), or the revised meter composite depth scale (historically called rmcd but known as rCCSF at Site U1403) from Batenburg et al. 2017 as described in the methods section.

Table S16.
Osmium isotope data from Site U1403 generated by G.E.R. at the University of Hawaii at Mānoa. Depths at Site U1403 are reported relative to one (or more) of three scales: the primary sample ID, the meters below seafloor of the sample (historically called msbf but known as CSF-A at Site U1403), or the revised meter composite depth scale (historically called rmcd but known as rCCSF at Site U1403) from Batenburg et al. 2017. The column 'A/W' denotes samples from the archive (A) versus working (W) half of the core.

Table S17.
Resolved nannoplankton assemblage counts at IODP Site U1403, carried out by HK and PB at the University College London.

Table S18.
Resolved nannoplankton assemblage counts at ODP Site 1209, carried out by J.S. and T.B. at Penn State.

Table S19.
Weight % carbonate as calculated from mass spectrometer voltage intensity for the Site U1403 bulk carbonate samples measured at Yale University. In house standards were used to calibrate the relationship between the absolute mass of calcium carbonate and the intensity of the signal measured in mV. For a pure carbonate, intensity scaled as the mass (μg) * 22.683. With the relationship, we predicted the intensity for each sample ('Predicted Intensity (mV) as equal to the 'Weight (ug)' * 22.683). The difference between the actual intensity measured by the mass spectrometer ('Measured Intensity (mV')) and the predicted intensity was used to calculate the weight % carbonate of the bulk sediment. Depths at Site U1403 are reported relative to one (or more) of three scales: the primary sample ID, the meters below seafloor of the sample (historically called msbf but known as CSF-A at Site U1403), or the revised meter composite depth scale (historically called rmcd but now known as rCCSF at Site U1403) from Batenburg et al. 2017.

Table S20.
XRF-based weight % carbonate (calc. wt % $CaCO_3$) and $CaCO_3$ mass accumulation rates for IODP Site U1403. XRF counts of Ca were linearly correlated to mass spectrometry inferred measurements of weight % carbonate (from Table S12) and discrete shipboard measurements (Norris et al. 2014). This correlation was used to calculate the 'calc. wt % $CaCO_3$' shown below for all XRF measurements of Ca. This calculated wt % carbonate was used in combination with linear sedimentation rates and linearly interpolated dry bulk density measurements (interpolated from shipboard measurements in Norris et al. 2014) to calculate the carbonate mass accumulation rates below.

Table S21.
XRF data for Danian of IODP Site U1403 collected by O.F., A.B., S.J., and I.M. at the IODP Bremen Core Repository. Depths at Site U1403 are reported relative to one (or more) of three scales: the primary sample ID, the meters below seafloor of the sample (historically called msbf but known as CSF-A at Site U1403), or the revised meter composite depth scale (historically called rmcd but known as rCCSF at Site U1403) from Batenburg et al. 2017.

Table S22.
Visualization of the adjustment to the off-splice boundary core (Core U1403B-28) relative to the CCSF used to calculate an appropriate relative depth for the sample sets collected off-splice in this section (coarse fraction, fish teeth and iridium records).

Table S23.
Cyclostratigraphic age model for Danian to Maastrichtian of Site U1403 generated by S.B. Age model combines new tie-points in the Danian with the Maastrichtian tie-points of Batenburg et al. 2017. Depths at Site U1403 are reported relative to one (or more) of three scales: the primary sample ID, the meters below seafloor of the sample (historically called msbf but known as CSF-A at Site U1403), or the revised meter composite depth scale (historically called rmcd but known as rCCSF at Site U1403) from Batenburg et al. 2017.

Table S24.
Updated nannofossil biostratigraphy from Hole U1403A of Paleocene species, revised by P.B. In 'Nanno event' B=bottom and T=top; in 'Preservation' G=good, M=moderate,P=poor (after Norris et al. 2014); in 'Nannofossil abundance' A=abundant, C=common, R=rare, F=frequent, SA=somewhat abundant, and numbers indicate absolute numbers observed (after Norris et al. 2014); in species counts '?' indicates uncertainty in an absence (-) or abundance (A, C, F, R, SA). Depths at Site U1403 are reported relative to one (or more) of three scales: the primary sample ID, the meters below seafloor of the sample (historically called msbf but known as CSF-A at Site U1403), or the revised meter composite depth scale (historically called rmcd but known as rCCSF at Site U1403) from Batenburg et al. 2017.

Table S25.
Updated nannofossil biostratigraphic tiepoints from Hole U1403A, revised by P.B. Depths at Site U1403 are reported relative to one (or more) of three scales: the primary sample ID, the meters below seafloor of the sample (historically called msbf but known as CSF-A at Site

U1403), or the revised meter composite depth scale (historically called rmcd but known as rCCSF at Site U1403) from Batenburg et al. 2017.

Table S26.
Samples from Site U1403 checked for organic-walled fossils by K.K.S. Samples were barren with the exception of a single dinocyst and two questionable palynomorphs. Depths at Site U1403 are reported relative to one (or more) of three scales: the primary sample ID, the meters below seafloor of the sample (historically called msbf but known as CSF-A at Site U1403), or the revised meter composite depth scale (historically called rmcd but known as rCCSF at Site U1403) from Batenburg et al. 2017.

Table S27.
Paleomagnetic data used for the final interpretation of the magnetozones at site U1403. Sample ID, rCCSF(m), mean declination, mean inclination of the ChRM and its corresponding 95% confidence angle are given. Samples collected by C.C. and P.L. and analyzed by C.C. at CEREGE (Aix-en-Provence, France) using a SQUID cryogenic magnetometer (2G Enterprises, model 755R, with noise level of 10−11Am2) with an attached automatic alternating field 3-axis degausser system (maximum peak field 170 mT) placed in a magnetically shielded room (field of ~250 nT).

Table S28.
IODP Site U1403 samples selected for organic geochemistry analysis via GC-MRM-MS by J.W., J.S. and R.S. Thermal maturity indices (expressed as %) based on the stereochemistry of algal steranes and bacterial hopanes compared to a laboratory blank. 1: ratio of C_{27} diasteranes and regular desmethyl cholestanes; 2: ratio of C_{27} αββ and ααα desmethyl cholestanes; 3: ratio of C_{27} ααα S and R desmethyl cholestanes; 4: ratio of C_{31} S and R hopanes.

Table S29.
Ichthyolith mass accumulation rates at Site U1403 collected by E.S. at the Scripps Institution of Oceanography (University of California San Diego).

Table S30.
LOSCAR model output for all Deccan and extinction simulations. Each scenario for the timing of Deccan outgassing was run with both low (3200 GtS, 4090 GtC) and high (8500 GtS, 9545 GtC) emission volumes, and across a range of climate sensitivities of 2, 3, and 4˚C per doubling of CO_2. For each run, timesteps are expressed both in model time (beginning at t=0, 390kyr before the K/Pg boundary) and as years relative to the K/Pg boundary. Surface temperature refers to the low-latitude surface Pacific Ocean but does not differ significantly between oceans.

Table S31.
Mean absolute error (MAE) and mean minimum absolute error (MMAE) of cases relative to the interpolated $\delta^{13}C$ record. The mean minimum absolute error (MMAE) was calculated for each case by determining whether the empirical data fell outside of the $\delta^{13}C$ range bounded by the high and low outgassing scenarios given a climate sensitivity of 3°C/CO_2 doubling, and, if so, by how much. MAEs were also calculated for each outgassing volume at a climate sensitivity of

3°C/CO_2 doubling (note: climate sensitivity did not noticeably affect $\delta^{13}C$) and as shown in Fig. 4. MMAEs and MAEs were calculated on a 20 kyr interpolated time step from 440 kyr to 10 kyr prior to the K/Pg.

References

1. L. W. Alvarez, W. Alvarez, F. Asaro, H. V. Michel, Extraterrestrial cause for the Cretaceous-Tertiary extinction - experimental results and theoretical interpretation. *Science* **208**, 1095-1108 (1980).
2. A. R. Hildebrand *et al.*, Chicxulub crater - a possible Cretaceous Tertiary Boundary impact crater on the Yucatan Peninsula, Mexico. *Geology* **19**, 867-871 (1991).
3. B. Collen *et al.*, Clarifying misconceptions of extinction risk assessment with the IUCN Red List. *Biology Letters* **12**, 20150843 (2016).
4. J. Morgan *et al.*, Size and morphology of the Chicxulub impact crater. *Nature* **390**, 472-476 (1997).
5. P. Schulte *et al.*, The Chicxulub Asteroid Impact and Mass Extinction at the Cretaceous-Paleogene Boundary. *Science* **327**, 1214-1218 (2010).
6. G. Ravizza, D. VonderHaar, A geochemical clock in earliest Paleogene pelagic carbonates based on the impact-induced Os isotope excursion at the Cretaceous-Paleogene boundary. *Paleoceanography* **27**, PA3219 (2012).
7. F. M. Gradstein, J. G. Ogg, M. D. Schmitz, G. M. Ogg, *The Geologic Time Scale 2012*. (Elsevier B.V., Amsterdam, 2012).
8. B. Schoene *et al.*, U-Pb constraints on pulsed eruption of the Deccan Traps across the end-Cretaceous mass extinction. *Science* **363**, 862-866 (2019).
9. C. J. Sprain *et al.*, The eruptive tempo of Deccan volcanism in relation to the Cretaceous-Paleogene boundary. *Science* **363**, 866-870 (2019).
10. A. L. Chenet *et al.*, Determination of rapid Deccan eruptions across the Cretaceous-Tertiary boundary using paleomagnetic secular variation: 2. Constraints from analysis of eight new sections and synthesis for a 3500-m-thick composite section. *Journal of Geophysical Research-Solid Earth* **114**, B06103 (2009).
11. A. L. Chenet, X. Quidelleur, F. Fluteau, V. Courtillot, S. Bajpai, K-40-Ar-40 dating of the Main Deccan large igneous province: Further evidence of KTB age and short duration. *Earth and Planetary Science Letters* **263**, 1-15 (2007).
12. B. Schoene *et al.*, U-Pb geochronology of the Deccan Traps and relation to the end-Cretaceous mass extinction. *Science* **347**, 182-184 (2015).
13. P. R. Renne *et al.*, State shift in Deccan volcanism at the Cretaceous-Paleogene boundary, possibly induced by impact. *Science* **350**, 76-78 (2015).
14. P. R. Renne *et al.*, Time Scales of Critical Events Around the Cretaceous-Paleogene Boundary. *Science* **339**, 684-687 (2013).
15. M. A. Richards *et al.*, Triggering of the largest Deccan eruptions by the Chicxulub impact. *Geological Society of America Bulletin* **127**, 1507-1520 (2015).
16. E. Font *et al.*, Deccan volcanism induced high-stress environment during the Cretaceous-Paleogene transition at Zumaia, Spain: Evidence from magnetic, mineralogical and biostratigraphic records. *Earth and Planetary Science Letters* **484**, 53-66 (2018).
17. N. Artemieva, J. Morgan, E. S. Party, Quantifying the Release of Climate-Active Gases by Large Meteorite Impacts With a Case Study of Chicxulub. *Geophysical Research Letters* **44**, 10180-10188 (2017).
18. S. P. S. Gulick *et al.*, The first day of the Cenozoic. *Proceedings of the National Academy of Sciences of the United States of America* **116**, 19342-19351 (2019).

19. D. A. Kring, D. D. Durda, Trajectories and distribution of material ejected from the Chicxulub impact crater: implications for postimpact wildfires. *Journal of Geophysical Research-Planets* **107**, (2002).
20. J. Morgan, N. Artemieva, T. Goldin, Revisiting wildfires at the K-Pg boundary. *J Geophys Res-Biogeo* **118**, 1508-1520 (2013).
21. S. Ohno *et al.*, Production of sulphate-rich vapour during the Chicxulub impact and implications for ocean acidification. *Nature Geoscience* **7**, 279-282 (2014).
22. T. Tyrrell, A. Merico, D. I. A. McKay, Severity of ocean acidification following the end-Cretaceous asteroid impact. *Proceedings of the National Academy of Sciences of the United States of America* **112**, 6556-6561 (2015).
23. M. J. Henehan *et al.*, Rapid ocean acidification and protracted Earth System recovery followed the end-Cretaceous Chixulub impact. *Proceedings of the National Academy of Sciences of the United States of America*, (2019).
24. J. Vellekoop *et al.*, Rapid short-term cooling following the Chicxulub impact at the Cretaceous-Paleogene boundary. *Proceedings of the National Academy of Sciences of the United States of America* **111**, 7537-7541 (2014).
25. K. Kaiho *et al.*, Global climate change driven by soot at the K-Pg boundary as the cause of the mass extinction. *Sci Rep-Uk* **6**, (2016).
26. J. Brugger, G. Feulner, S. Petri, Baby, it's cold outside: Climate model simulations of the effects of the asteroid impact at the end of the Cretaceous. *Geophysical Research Letters* **44**, 419-427 (2017).
27. C. G. Bardeen, R. R. Garcia, O. B. Toon, A. J. Conley, On transient climate change at the Cretaceous-Paleogene boundary due to atmospheric soot injections. *Proceedings of the National Academy of Sciences of the United States of America* **114**, E7415-E7424 (2017).
28. L. Alegret, E. Thomas, K. C. Lohmann, End-Cretaceous marine mass extinction not caused by productivity collapse. *Proceedings of the National Academy of Sciences of the United States of America* **109**, 728-732 (2012).
29. B. J. Marshall, R. C. Thunell, M. J. Henehan, Y. Astor, K. E. Wejnert, Planktonic foraminiferal area density as a proxy for carbonate ion concentration: A calibration study using the Cariaco Basin ocean time series. *Paleoceanography* **28**, 363-376 (2013).
30. M. Aberhan, S. Weidemeyer, W. Kiessling, R. A. Scasso, F. A. Medina, Faunal evidence for reduced productivity and uncoordinated recovery in Southern Hemisphere Cretaceous-Paleogene boundary sections. *Geology* **35**, 227-230 (2007).
31. P. M. Sheehan, T. A. Hansen, Detritus Feeding as a Buffer to Extinction at the End of the Cretaceous. *Geology* **14**, 868-870 (1986).
32. D. S. Robertson, M. C. McKenna, O. B. Toon, S. Hope, J. A. Lillegraven, Survival in the first hours of the Cenozoic. *Geological Society of America Bulletin* **116**, 760-768 (2004).
33. E. M. Shoemaker, Impact cratering through geologic time. *Journal of the Royal Astronomical Society of Canada* **92**, 297-309 (1998).
34. J. D. Archibald *et al.*, Cretaceous Extinctions: Multiple Causes. *Science* **328**, 973-973 (2010).
35. G. Keller, J. Punekar, P. Mateo, Upheavals during the Late Maastrichtian: Volcanism, climate and faunal events preceding the end-Cretaceous mass extinction. *Palaeogeography Palaeoclimatology Palaeoecology* **441**, 137-151 (2016).
36. S. V. Sobolev *et al.*, Linking mantle plumes, large igneous provinces and environmental catastrophes. *Nature* **477**, 312-U380 (2011).

37. M. T. Jones, D. A. Jerram, H. H. Svensen, C. Grove, The effects of large igneous provinces on the global carbon and sulphur cycles. *Palaeogeography Palaeoclimatology Palaeoecology* **441**, 4-21 (2016).
38. A. Schmidt *et al.*, Selective environmental stress from sulphur emitted by continental flood basalt eruptions. *Nature Geoscience* **9**, 77-82 (2016).
39. S. Self, S. Blake, K. Sharma, M. Widdowson, S. Sephton, Sulfur and chlorine in Late Cretaceous Deccan magmas and eruptive gas release. *Science* **319**, 1654-1657 (2008).
40. Materials and methods are available as supplementary materials at the Science website.
41. M. J. Henehan, P. M. Hull, D. E. Penman, J. W. B. Rae, D. N. Schmidt, Biogeochemical significance of pelagic ecosystem function: an end-Cretaceous case study. *Philosophical Transactions of the Royal Society B-Biological Sciences* **371**, 20150510 (2016).
42. J. S. K. Barnet *et al.*, A new high-resolution chronology for the late Maastrichtian warming event: Establishing robust temporal links with the onset of Deccan volcanism. *Geology* **46**, 147-150 (2018).
43. J. S. K. Barnet *et al.*, A high-fidelity benthic stable isotope record of Late Cretaceous-Early Eocene climate change and carbon-cycling. *Paleoceanography and Paleoclimatology* **34**, 672-691 (2019).
44. L. Q. Li, G. Keller, Abrupt deep-sea warming at the end of the Cretaceous. *Geology* **26**, 995-998 (1998).
45. R. D. Norris, P. A. Wilson, P. Blum, a. t. E. Scientists, in *Proc. IODP, 342,* R. D. Norris, Wilson, P.A., Blum, P., and the Expedition 342 Scientists, Ed. (Integrated Ocean Drilling Program, College Station, TX, 2014).
46. N. Robinson, G. Ravizza, R. Coccioni, B. Peucker-Ehrenbrink, R. Norris, A high-resolution marine Os-187/Os-188 record for the late Maastrichtian: distinguishing the chemical fingerprints of Deccan volcanism and the KP impact event. *Earth and Planetary Science Letters* **281**, 159-168 (2009).
47. R. E. Zeebe, LOSCAR: Long-term Ocean-atmosphere-Sediment CArbon cycle Reservoir Model v2.0.4. *Geoscientific Model Development* **5**, 149-166 (2012).
48. J. C. Zachos, M. A. Arthur, W. E. Dean, Geochemical evidence for suppression of pelagic marine productivity at the Cretaceous/Tertiary boundary. *Nature* **337**, 61-64 (1989).
49. H. S. Birch, H. K. Coxall , P. N. Pearson, D. Kroon, D. N. Schmidt, Partial collapse of the marine carbon pump after the Cretaceous-Paleogene boundary. *Geology* **44**, 287-290 (2016).
50. C. J. Sprain, P. R. Renne, W. A. Clemens, G. P. Wilson, Calibration of chron C29r: New high-precision geochronologic and paleomagnetic constraints from the Hell Creek region, Montana. *Geological Society of America Bulletin* **130**, 1615-1644 (2018).
51. E. J. Rohling *et al.*, Comparing Climate Sensitivity, Past and Present. *Annual Review of Marine Science, Vol 10* **10**, 261-+ (2018).
52. K. G. MacLeod, P. C. Quinton, J. Sepulveda, M. H. Negra, Postimpact earliest Paleogene warming shown by fish debris oxygen isotopes (El Kef, Tunisia). *Science* **360**, 1467-1469 (2018).
53. S. D'Hondt, P. Donaghay, J. C. Zachos, D. Luttenberg, M. Lindinger, Organic carbon fluxes and ecological recovery from the Cretaceous-Tertiary mass extinction. *Science* **282**, 276-279 (1998).

54. J. D. Witts *et al.*, Macrofossil evidence for a rapid and severe Cretaceous-Paleogene mass extinction in Antarctica. *Nat Commun* **7**, 11738 (2016).
55. T. S. Tobin, Recognition of a likely two phased extinction at the K-Pg boundary in Antarctica. *Sci Rep-Uk* **7**, 16317 (2017).
56. P. M. Hull, R. D. Norris, T. J. Bralower, J. D. Schueth, A role for chance in marine recovery from the end-Cretaceous extinction. *Nature Geoscience* **4**, 856-860 (2011).
57. J. J. Pospichal, in *The Cretaceous-Tertiary event and other catastrophes in Earth history: Geological Society of America Special Paper 307,* G. Ryder, D. Fastovsky, S. Gartner, Eds. (1996), pp. 335-360.
58. E. C. Sibert, M. Friedman, P. M. Hull, G. Hunt, R. D. Norris, Two pulses of origination in Pacific pelagic fish following the Cretaceous-Paleogene Mass Extinction. *Proceedings of the Royal Society B-Biological Sciences*, 20181194 (2018).
59. M. Edmonds, New geochemical insights into volcanic degassing. *Philosophical Transactions of the Royal Society a-Mathematical Physical and Engineering Sciences* **366**, 4559-4579 (2008).
60. P. F. Sexton *et al.*, Eocene global warming events driven by ventilation of oceanic dissolved organic carbon. *Nature* **471**, 349-352 (2011).
61. R. D. Norris, in *Palaeobiology II,* D. E. G. Briggs, P. G. Crowther, Eds. (Blackwell Science Ltd., Oxford, 2001), pp. 229-231.
62. R. D. Norris *et al.*, in *Proc. IODP 342,* R. D. Norris, P. A. Wilson, P. Blum, a. t. E. Scientists, Eds. (College Station, TX (Integrated Ocean Drilling Program), 2014).
63. T. Bralower, I. Premoli Silva, M. J. Malone, e. al., Site 1209. *Site 1209, Proc. ODP, Initial Reports* **198**, 1-102 (2002).
64. T. Bralower, I. Premoli Silva, M. J. Malone, e. al., Leg 198 Summary. *Leg 198 Summary, Proc. ODP, Initial Reports* **198**, 1-148 (2002).
65. G. R. Heath, L. H. Burckle, e. al., in *Init. Repts. DSDP, 86,* G. R. Heath, L. H. Burckle, e. al., Eds. (U.S. Govt. Printing Office, Washington, 1985), vol. 86, pp. 91-137.
66. S. S. Party, in *Proc. ODP, Init. Repts., 208,* J. C. Zachos, D. Kroon, P. Blum, Eds. (Ocean Drilling Program, College Station, TX, 2004), pp. 1-92.
67. S. S. Party, in *Proc. ODP, Init. Repts., 208,* J. C. Zachos, D. Kroon, P. Blum, Eds. (Ocean Drilling Program, College Station, TX, 2004).
68. T. Westerhold *et al.*, Astronomical calibration of the Paleocene time. *Palaeogeography Palaeoclimatology Palaeoecology* **257**, 377-403 (2008).
69. S. J. Batenburg *et al.*, Cyclostratigraphy and astronomical tuning of the Late Maastrichtian at Zumaia (Basque country, Northern Spain). *Earth and Planetary Science Letters* **359-360**, 264-278 (2012).
70. F. J. Hilgen, K. F. Kuiper, L. J. Lourens, Evaluation of the astronomical time scale for the Paleocene and earliest Eocene. *Earth and Planetary Science Letters* **300**, 139-151 (2010).
71. T. Westerhold, U. Röhl, J. Laskar, Time scale controversy: Accurate orbital calibration of the early Paleogene. *Geochemistry Geophysics Geosystems* **13**, (2012).
72. J. Dinarès-Turell, T. Westerhold, V. Pujalte, U. Röhl, D. Kroon, Astronomical calibration of the Danian stage (Early Paleocene) revisited: Settling chronologies of sedimentary records across the Atlantic and Pacific Oceans. *Earth and Planetary Science Letters* **405**, 119-131 (2014).

73. T. Westerhold, U. Röhl, B. Donner, H. K. McCarren, J. C. Zachos, A complete high-resolution Paleocene benthic stable isotope record for the central Pacific (ODP Site 1209). *Paleoceanography*, (2011).
74. C. Jung, S. Voigt, O. Friedrich, M. C. Koch, M. Frank, Campanian-Maastrichtian ocean circulation in the tropical Pacific. *Paleoceanography* **28**, 562-573 (2013).
75. C. Jung, S. Voigt, O. Friedrich, High-resolution carbon-isotope stratigraphy across the Campanian-Maastrichtian boundary at Shatsky Rise (tropical Pacific). *Cretaceous Research* **37**, 177-185 (2012).
76. L. M. Fuqua, T. J. Bralower, M. A. Arthur, M. E. Patzkowsky, Evolution of calcareous nannoplankton and the recovery of marine food webs after the cretaceous-paleocene mass extinction. *Palaios* **23**, 185-194 (2008).
77. S. J. Jiang, T. J. Bralower, M. E. Patzkowsky, L. R. Kump, J. D. Schueth, Geographic controls on nannoplankton extinction across the Cretaceous/Palaeogene boundary. *Nature Geoscience* **3**, 280-285 (2010).
78. J. D. Schueth, K. Keller, T. J. Bralower, M. E. Patzkowsky, The Probable Datum Method (PDM): a technique for estimating the age of origination or extinction of nannoplankton. *Paleobiology* **40**, 541-559 (2014).
79. J. D. Schueth, T. J. Bralower, S. Jiang, M. E. Patzkowsky, The role of regional survivor incumbency in the evolutionary recovery of calcareous nannoplankton from the Cretaceous/Paleogene (K/Pg) mass extinction. *Paleobiology*, 1-19 (2015).
80. P. Bown, Selective calcareous nannoplankton survivorship at the Cretaceous-Tertiary boundary. *Geology* **33**, 653-656 (2005).
81. T. J. Bralower, in *Proc. ODP, Sci. Results 146 (Pt. 2),* T. J. Bralower, I. Premoli Silva, M. J. Malone, Eds. (2005), pp. 1-15.
82. I. Premoli Silva, M. R. Petrizzo, D. Melloni, in *Proc. ODP, Sci. Results, 198,* T. Bralower, I. Premoli Silva, M. J. Malone, Eds. (2005), vol. 198, pp. 1-16.
83. L. Alegret, E. Thomas, Food supply to the seafloor in the Pacific Ocean after the Cretaceous/Paleogene boundary event. *Marine Micropaleontology* **73**, 105-116 (2009).
84. E. C. Sibert, P. M. Hull, R. D. Norris, Resilience of Pacific pelagic fish across the Cretaceous/Palaeogene mass extinction. *Nature Geoscience* **7**, 667-670 (2014).
85. P. M. Hull, R. D. Norris, Diverse patterns of ocean export productivity change across the Cretaceous-Paleogene boundary: New insights from biogenic barium. *Paleoceanography* **26**, 1-10 (2011).
86. A. Dutton, K. C. Lohmann, R. M. Leckie, Insights from the Paleogene tropical Pacific: Foraminiferal stable isotope and elemental results from Site 1209, Shatsky Rise. *Paleoceanography* **20**, PA 3004 (2005).
87. T. D. Frank *et al.*, The Maastrichtian record from Shatsky Rise (northwest Pacific): A tropical perspective on global ecological and oceanographic changes. *Paleoceanography* **20**, PA 1008 (2005).
88. H. V. Michel, F. Asaro, W. Alvarez, L. W. Alvarez, in *Init. Repts. DSDP, 86,* G. R. Heath, L. H. Burckle, e. al., Eds. (U. S. Govt. Printing Office, Washington, 1985), vol. 86, pp. 533-538.
89. J. Gerstel, R. C. Thunell, The Cretaceous/Tertiary boundary event in the North Pacific: planktonic foraminiferal results from Deep Sea Drilling Project Site 577, Shatsky Rise. *Paleoceanography* **1**, 97-117 (1986).

90. J. C. Zachos, M. A. Arthur, R. Thunell, D. F. Williams, E. J. Tappa, in *Init. Repts. DSDPP, 86,* G. R. Heath, L. H. Burckle, e. al., Eds. (U.S. Govt. Printing Office, Washington, 1985), pp. 513 - 532.
91. A. A. Wright *et al.*, in *Init. Repts. DSDPP, 86,* G. R. Heath, L. H. Burckle, e. al., Eds. (U. S. Govt. Printing Office, Washington, 1985), pp. 799-804.
92. B. R. T. Simoneit, H. R. Beller, in *Init. Repts. DSDP, 86,* G. R. Heath, L. H. Burckle, e. al., Eds. (U.S. Govt. Printing Office, Washington, 1985), pp. 671-674.
93. S. D'Hondt, G. Keller, Some patterns of planktic foraminiferal assemblage turnover at the Cretaceous Tertiary boundary. *Marine Micropaleontology* **17**, 77-118 (1991).
94. H. K. Coxall, S. D'Hondt, J. C. Zachos, Pelagic evolution and environmental recovery after the Cretaceous-Paleogene mass extinction. *Geology* **34**, 297-300 (2006).
95. J. Gerstel, R. Thunell, R. Ehrlich, Danian Faunal Succession - Planktonic Foraminiferal Response to a Changing Marine-Environment. *Geology* **15**, 665-668 (1987).
96. D. Kroon, J. C. Zachos, L. S. Party, in *Proc. ODP, Sci. Results 208,* D. Kroon, J. C. Zachos, C. Richter, Eds. (Ocean Drilling Program, College Station, TX, 2007), pp. 1-55.
97. L. Woelders *et al.*, Latest Cretaceous climatic and environmental change in the South Atlantic region. *Paleoceanography* **32**, 466-483 (2017).
98. S. Voigt, A. S. Gale, C. Jung, H. C. Jenkyns, Global correlation of Upper Campanian - Maastrichtian successions using carbon-isotope stratigraphy: development of a new Maastrichtian timescale. *Newsletters on Stratigraphy* **45**, 25-53 (2012).
99. S. J. Batenburg *et al.*, Late Maastrichtian carbon isotope stratigraphy and cyclostratigraphy of the Newfoundland Margin (Site U1403, IODP Leg 342). *Newsletters on Stratigraphy*, (2017).
100. T. J. Bralower, C. K. Paull, R. M. Leckie, The Cretaceous-Tertiary boundary cocktail: Chicxulub impact triggers margin collapse and extensive sediment gravity flows. *Geology* **26**, 331-334 (1998).
101. A. Klaus, R. D. Norris, D. Kroon, J. Smit, Impact-induced mass wasting at the K-T boundary: Blake Nose, western North Atlantic. *Geology* **28**, 319-322 (2000).
102. R. D. Norris, J. Firth, J. S. Blusztajn, G. Ravizza, Mass failure of the North Atlantic margin triggered by the Cretaceous-Paleogene bolide impact. *Geology* **28**, 1119-1122 (2000).
103. R. Tada *et al.*, in *Catastrophic events and mass extinctions: impacts and beyond: Geological Society of America Special Paper 356,* C. Koeberl, K. G. MacLeod, Eds. (2002), vol. 356, pp. 109-123.
104. J. Smit *et al.*, in *The Cretaceous-Tertiary event and other catastrophes in earth history,* G. Ryder, D. Fastovsky, S. Gartner, Eds. (1996), vol. 307, pp. 151-182.
105. J. Bourgeois, T. A. Hansen, P. L. Wiberg, E. G. Kauffman, A tsunami deposit at the Cretaceous-Tertiary boundary in Texas. *Science* **241**, 567-570 (1988).
106. J. Smit, The global stratigraphy of the Cretaceous-Tertiary boundary impact ejecta. *Annual Review of Earth and Planetary Sciences* **27**, 75-113 (1999).
107. G. Keller, W. Stinnesbeck, T. Adatte, D. Stuben, Multiple impacts across the Cretaceous-Tertiary boundary. *Earth-Science Reviews* **62**, 327-363 (2003).
108. G. Keller *et al.*, More evidence that the Chicxulub impact predates the K/T mass extinction. *Meteoritics & Planetary Science* **39**, 1127-1144 (2004).
109. G. Keller *et al.*, Chicxulub impact predates K-T boundary: new evidence from Brazos, Texas. *Earth and Planetary Science Letters* **255**, 339-356 (2007).

110. S. J. Batenburg *et al.*, Late Maastrichtian carbon isotope stratigraphy and cyclostratigraphy of the Newfoundland Margin (Site U1403, IODP Leg 342). *Newsletters on Stratigraphy*, (2017).
111. F. J. Hilgen, H. A. Abeis, K. F. Kuiper, L. J. Lourens, M. Wolthers, Towards a stable astronomical time scale for the Paleocene: Aligning Shatsky Rise with the Zumaia - Walvis Ridge ODP Site 1262 composite. *Newsletters on Stratigraphy* **48**, 91-110 (2015).
112. S. Expedition, Paleogene Newfoundland sediment drifts. *IODP Prel. Rept. 342*, (2012).
113. D. Paillard, L. Labeyrie, P. Yiou, Macintosh program performs time-series analysis. *EOS Trans. AGU* **77**, 379 (1996).
114. J. Laskar, M. Gastineau, J. B. Delisle, A. Farres, A. Fienga, Strong chaos induced by close encounters with Ceres and Vesta. *Astron Astrophys* **532**, (2011).
115. J. P. Cogn, PaleoMac: A Macintosh (TM) application for treating paleomagnetic data and making plate reconstructions. *Geochemistry Geophysics Geosystems* **4**, (2003).
116. J. G. Ogg, in *The Geologic Time Scale,* F. M. Gradstein, J. G. Ogg, M. D. Schmitz, G. D. Ogg, Eds. (Elsevier, Oxford, United Kingdom,, 2012), pp. 85-113.
117. G. Ravizza, B. Peucker-Ehrenbrink, Chemostratigraphic evidence of Deccan volcanism from the marine osmium isotope record. *Science* **302**, 1392-1395 (2003).
118. F. S. Paquay, G. E. Ravizza, T. K. Dalai, B. Peucker-Ehrenbrink, Determining chondritic impactor size from the marine osmium isotope record. *Science* **320**, 214-218 (2008).
119. G. Ravizza, Reconstructing the marine Os-187/Os-188 record and the particulate flux of meteoritic osmium during the late Cretaceous. *Geochimica Et Cosmochimica Acta* **71**, 1355-1369 (2007).
120. D. Loroch, A. Deutsch, J. Berndt, A. Bornemann, The Cretaceous/Paleogene (K-Pg) boundary at the J Anomaly Ridge, Newfoundland (IODP Expedition 342, Hole U1403B). *Meteoritics & Planetary Science* **51**, 1370-1385 (2016).
121. K. Moriya, A. S. Goto, T. Hasegawa, Stable carbon and oxygen isotope analyses of carbonate using a continuous flow isotope ratio mass spectrometry. *The science reports of the Kanazawa University* **56**, 45-58 (2012).
122. F. Minoletti, M. de Rafelis, M. Renard, S. Gardin, J. Young, Changes in the pelagic fine fraction carbonate sedimentation during the Cretaceous-Paleocene transition: contribution of the separation technique to the study of Bidart section. *Palaeogeography Palaeoclimatology Palaeoecology* **216**, 119-137 (2005).
123. J. Sepulveda, J. E. Wendler, R. E. Summons, K. U. Hinrichs, Rapid resurgence of marine productivity after the Cretaceous-Paleogene mass extinction. *Science* **326**, 129-132 (2009).
124. H. Rashid, E. Grosjean, Detecting the source of Heinrich layers: An organic geochemical study. *Paleoceanography* **21**, PA 3014 (2006).
125. A. H. Kasprak *et al.*, Episodic photic zone euxinia in the northeastern Panthalassic Ocean during the end-Triassic extinction. *Geology* **43**, 307-310 (2015).
126. J. C. Zachos *et al.*, in *Proc. ODP, Sci. Results, 120,* S. W. Wise, Jr. , R. Schlich, Eds. (Ocean Drilling Program, College Station, TX, 1992), pp. 961–977.
127. K. R. Johnson, M. L. Reynolds, K. W. Werth, J. R. Thomasson, Overview of the Late Cretaceous, early Paleocene, and early Eocene megafloras of the Denver Basin, Colorado. *Rocky Mountain Geology* **38**, 101-120 (2003).

128. S. D'Hondt, M. Lindinger, A stable isotopic record of the Maastrichtian ocean-climate system: South Atlantic DSDP Site 528. *Palaeogeography Palaeoclimatology Palaeoecology* **112**, 363-378 (1994).
129. L. Alegret, E. Thomas, Benthic foraminifera across the Cretaceous/Paleogene boundary in the Southern Ocean (ODP Site 690): Diversity, food and carbonate saturation. *Marine Micropaleontology* **105**, 40-51 (2013).
130. F. Quillevere, R. D. Norris, D. Kroon, P. A. Wilson, Transient ocean warming and shifts in carbon reservoirs during the early Danian. *Earth and Planetary Science Letters* **265**, 600-615 (2008).
131. W. A. Berggren, R. D. Norris, Biostratigraphy, phylogeny and systematics of Paleocene trochospiral planktic foraminifera. *Micropaleontology* **43**, 1-116 (1997).
132. S. Esmeray-Senlet *et al.*, Evidence for reduced export productivity following the Cretaceous/Paleogene mass extinction. *Paleoceanography* **30**, 718-738 (2015).
133. J. Erez, B. Luz, Experimental Paleotemperature Equation for Planktonic-Foraminifera. *Geochimica Et Cosmochimica Acta* **47**, 1025-1031 (1983).
134. N. J. Shackleton, M. A. Hall, A. Boersma, Oxygen and carbon isotope data from Leg 74 foraminifers. *Initial Rep. Deep Sea Drill. Proj. 74: Washington (U.S. Govt. Printing Office)*, 599–612 (1984).
135. L. D. Stott, J. P. Kennett, in *Proc. ODP, Sci. Repts., 113,* P. F. Barker, J. P. Kennett, e. al., Eds. (Ocean Drilling Program, College Station, TX, 1990), pp. 829-848.
136. P. Wilf, K. R. Johnson, B. T. Huber, Correlated terrestrial and marine evidence for global climate chanaes before mass extinction at the Cretaceous-Paleogene boundary. *Proceedings of the National Academy of Sciences of the United States of America* **100**, 599-604 (2003).
137. L. Nordt, S. Atchley, I. Dworkin, Terrestrial evidence for two greenhouse events in the latest Cretaceous. *GSA Today* **13**, 4-9 (2003).
138. S. I. Dworkin, L. Nordt, S. Atchley, Determining terrestrial paleotemperatures using the oxygen isotopic composition of pedogenic carbonate. *Earth and Planetary Science Letters* **237**, 56-68 (2005).
139. C. E. Leslie *et al.*, Revised age constraints for Late Cretaceous to early Palaeocene terrestrial strata from the Dawson Creek section, Big Bend National Park, west Texas. *GSA Bulletin* **130**, 1143-1163 (2018).
140. T. S. Tobin *et al.*, Extinction patterns, delta(18) O trends, and magnetostratigraphy from a southern high-latitude Cretaceous-Paleogene section: Links with Deccan volcanism. *Palaeogeography Palaeoclimatology Palaeoecology* **350**, 180-188 (2012).
141. T. S. Tobin, G. P. Wilson, J. M. Eiler, J. H. Hartman, Environmental change across a terrestrial Cretaceous-Paleogene boundary section in eastern Montana, USA, constrained by carbonate clumped isotope paleothermometry. *Geology* **42**, 351-354 (2014).
142. S. V. Petersen, A. Dutton, K. C. Lohmann, End-Cretaceous extinction in Antarctica linked to both Deccan volcanism and meteorite impact via climate change. *Nat Commun* **7**, 12079 (2016).
143. R. LeCain, W. C. Clyde, G. P. Wilson, J. Riedel, in *Through the End of the Cretaceous in the Type Locality of the Hell Creek Formation in Mon- tana and Adjacent Areas: Geological Society of America Special Paper 503,* G. P. Wilson, W. A. Clemens, J. R. Horner, J. H. Hartman, Eds. (2014), pp. 137-147.

144. J. Vellekoop *et al.*, Evidence for Cretaceous-Paleogene boundary bolide "impact winter" conditions from New Jersey, USA. *Geology* **44**, 619-622 (2016).
145. L. Woelders *et al.*, Robust multi-proxy data integration, using Late Cretaceous paleotemperature records as a case study. *Earth and Planetary Science Letters* **500**, 215-224 (2018).
146. E. E. McIver, J. F. Basinger, Flora of the Ravenscrag Formation (Paleocene), southwestern Saskatchewan, Canada. *Palaeontographica Canadiana*, (1993).
147. K. S. Davies-Vollum, Early Palaeocene palaeoclimatic inferences from fossil floras of the western interior, USA. *Palaeogeography Palaeoclimatology Palaeoecology* **136**, 145-164 (1997).
148. D. J. Peppe, Megafloral change in the early and middle Paleocene in the Williston Basin, North Dakota, USA. *Palaeogeography Palaeoclimatology Palaeoecology* **298**, 224-234 (2010).
149. D. J. Peppe *et al.*, Sensitivity of leaf size and shape to climate: global patterns and paleoclimatic applications. *New Phytol.* **190**, 724-739 (2011).
150. P. Wilf, K. R. Johnson, Land plant extinction at the end of the Cretaceous: a quantitative analysis of the North Dakota megafloral record. *Paleobiology* **30**, 347-368 (2004).
151. I. M. Miller, M. T. Brandon, L. J. Hickey, Using leaf margin analysis to estimate the mid-Cretaceous (Albian) paleolatitude of the Baja BC block. *Earth and Planetary Science Letters* **245**, 95-114 (2006).
152. D. J. Peppe, D. A. D. Evans, A. V. Smirnov, Magnetostratigraphy of the Ludlow Member of the Fort Union Formation (Lower Paleocene) in the Williston Basin, North Dakota. *Geological Society of America Bulletin* **121**, 65-79 (2009).
153. R. K. Olsson, K. G. Miller, J. V. Browning, D. Habib, P. J. Sugarman, Ejecta layer at the Cretaceous-Tertiary boundary, Bass River, New Jersey (Ocean Drilling Program Leg 174AX). *Geology* **25**, 759-762 (1997).
154. R. K. Olsson, K. G. Miller, J. V. Browning, J. D. Wright, B. S. Cramer, Sequence stratigraphy and sea-level change across the Cretaceous-Tertiary boundary on the New Jersey passive margin. *Geol Soc Am Spec Pap* **356**, 97-108 (2002).
155. K. G. Miller *et al.*, in *Proc. ODP, Init. Repts., 174AX (Suppl.),* K. G. Miller, P. J. Sugarman, J. V. Browning, et al., Eds. (Ocean Drilling Program, College Station, TX 1999), pp. 1-65.
156. T. Dunkley Jones *et al.*, Climate model and proxy data constraints on ocean warming across the Paleocene-Eocene Thermal Maximum. *Earth-Science Reviews* **125**, 123-145 (2013).
157. J. Vellekoop *et al.*, Palynological evidence for prolonged cooling along the Tunisian continental shelf following the K-Pg boundary impact. *Palaeogeography Palaeoclimatology Palaeoecology* **426**, 216-228 (2015).
158. E. C. Sibert, M. Friedman, P. M. Hull, G. Hunt, R. D. Norris, Two pulses of origination in Pacific pelagic fish following the Cretaceous-Paleogene Mass Extinction. *Proceedings of the Royal Society B-Biological Sciences* **285**, 20181194 (2018).
159. M. Friedman, Explosive morphological diversification of spiny-finned teleost fishes in the aftermath of the end-Cretaceous extinction. *Proceedings of the Royal Society B-Biological Sciences* **277**, 1675-1683 (2010).

160. J. Kriwet, M. J. Benton, Neoselachian (Chondrichthyes, Elasmobranchii) diversity across the Cretaceous-Tertiary boundary. *Palaeogeography Palaeoclimatology Palaeoecology* **214**, 181-194 (2004).
161. M. P. Hain, D. M. Sigman, J. A. Higgins, G. H. Haug, The effects of secular calcium and magnesium concentration changes on the thermodynamics of seawater acid/base chemistry: Implications for Eocene and Cretaceous ocean carbon chemistry and buffering. *Global Biogeochemical Cycles* **29**, 517-533 (2015).
162. J. C. G. Walker, J. F. Kasting, Effects of fuel and forest conservation on future levels of atmospheric carbon dioxide. *Palaeogeography Palaeoclimatology Palaeoecology* **97**, 151-189 (1992).
163. J. Uchikawa, R. E. Zeebe, Influence of terrestrial weathering on ocean acidification and the next glacial inception. *Geophysical Research Letters* **35**, L23608 (2008).
164. S. D'Hondt, Consequences of the Cretaceous/Paleogene mass extinction for marine ecosystems. *Annu. Rev. Ecol. Evol. Syst.* **36**, 295-317 (2005).
165. E. Anagnostou *et al.*, Changing atmospheric CO2 concentration was the primary driver of early Cenozoic climate. *Nature* **533**, 380-384 (2016).
166. D. J. Beerling, B. H. Lomax, D. L. Royer, G. R. Upchurch, L. R. Kump, An atmospheric pCO(2) reconstruction across the Cretaceous-Tertiary boundary from leaf megafossils. *Proceedings of the National Academy of Sciences of the United States of America* **99**, 7836-7840 (2002).
167. N. C. Arens, A. H. Jahren, Carbon isotope excursion in atmospheric CO2 at the Cretaceous-Tertiary boundary: evidence from terrestrial sediments. *Palaios* **15**, 314-322 (2000).
168. T. Arinobu, R. Ishiwatari, K. Kaiho, M. A. Lamolda, Spike of pyrosynthetic polycyclic aromatic hydrocarbons associated with an abrupt decrease in delta C-13 of a terrestrial biomarker at the Cretaceous-Tertiary boundary at Caravaca, Spain. *Geology* **27**, 723-726 (1999).
169. S. J. Day, M. Maslin, in *Large metorite impacts III: Geological Society of America Special Paper 384,* T. Kenkmann, F. Hörz, A. Deutsch, Eds. (2005), pp. 239-258.
170. M. D. Max, W. P. Dillon, C. Nishimura, B. G. Hurdle, Sea-floor methane blow-out and global firestorm at the K-T boundary. *Geo-Marine Letters* **18**, 285-291 (1999).
171. S. Self, M. Widdowson, T. Thordarson, A. E. Jay, Volatile fluxes during flood basalt eruptions and potential effects on the global environment: A Deccan perspective. *Earth and Planetary Science Letters* **248**, 518-532 (2006).
172. P. M. Hull, P. J. S. Franks, R. D. Norris, Mechanisms and models of iridium anomaly shape across the Cretaceous-Paleogene boundary. *Earth and Planetary Science Letters* **301**, 98-106 (2011).
173. T. Yamaguchi, A. Bornemann, H. Matsui, H. Nishi, Latest Cretaceous/Paleocene deep-sea ostracode fauna at IODP Site U1407 (western North Atlantic) and their response to environmental changes at the Cretaceous/Paleogene boundary and the Latest Danian Event. *Marine Micropaleontology* **135**, 32-44 (2017).
174. E. Sibert, R. Norris, J. Cuevas, L. Graves, Eighty-five million years of Pacific Ocean gyre ecosystem structure: long-term stability marked by punctuated change. *Proceedings of the Royal Society B-Biological Sciences* **283**, 20160189 (2016).
175. M. Kucera, B. A. Malmgren, Terminal Cretaceous warming event in the mid-latitude South Atlantic Ocean: evidence from poleward migration of Contusotruncana contusa

(planktonic foraminifera) morphotypes. *Palaeogeography Palaeoclimatology Palaeoecology* **138**, 1-15 (1998).
176. R. K. Olsson, J. D. Wright, K. G. Miller, Paleobiogeography of Pseudotextularia elegans during the latest Maastrichtian global warming event. *Journal of Foraminiferal Research* **31**, 275-282 (2001).
177. N. Thibault, S. Gardin, The calcareous nannofossil response to the end-Cretaceous warm event in the Tropical Pacific. *Palaeogeography Palaeoclimatology Palaeoecology* **291**, 239-252 (2010).
178. J. Punekar, P. Mateo, G. Keller, Effects of Deccan volcanism on paleoenvironment and planktic foraminifera: A global survey. *Volcanism, Impacts, and Mass Extinctions: Causes and Effects* **505**, 91-116 (2014).
179. G. P. Wilson, D. G. DeMar Jr., G. Carter, in *Through the End of the Cretaceous in the Type Locality of the Hell Creek Formation in Montana and Adjacent Areas: Geological Society of America Special Paper 503,* W. G. P., W. A. Clemens, J. H. Horner, J. H. Hartman, Eds. (2014), pp. 271-297.
180. G. P. Wilson, Mammalian extinction, survival, and recovery dynamics across the Cretaceous-Paleogene boundary in northeastern Montana, USA. *GSA Spec. Paper* **503**, 365-392 (2014).
181. S. Abramovich, G. Keller, Planktonic foraminiferal response to the latest Maastrichtian abrupt warm event: a case study from South Atlantic DSDP Site 525A. *Marine Micropaleontology* **48**, 225-249 (2003).
182. G. Keller, S. Abramovich, Lilliput effect in late Maastrichtian planktic foraminifera: Response to environmental stress. *Palaeogeography Palaeoclimatology Palaeoecology* **284**, 47-62 (2009).
183. S. Abramovich, S. Yovel-Corem, A. Almogi-Labin, C. Benjamini, Global climate change and planktic foraminiferal response in the Maastrichtian. *Paleoceanography* **25**, PA2201 (2010).
184. A. Pardo, G. Keller, Biotic effects of environmental catastrophes at the end of the Cretaceous and early Tertiary*: Guembelitria* and *Heterohelix* blooms. *Cretaceous Research* **29**, 1058-1073 (2008).
185. G. Keller, A. Pardo, Disaster opportunists Guembelitrinidae: index for environmental catastrophes. *Marine Micropaleontology* **53**, 83-116 (2004).
186. W. Y. Lu *et al.*, Late inception of a resiliently oxygenated upper ocean. *Science* **361**, 174-177 (2018).
187. P. B. Wignall, *The worst of times: how life on earth survived eighty million years of extinctions*. (Princeton University Press, 2015).
188. K. M. Meyer, A. Ridgwell, J. L. Payne, The influence of the biological pump on ocean chemistry: implications for long-term trends in marine redox chemistry, the global carbon cycle, and marine animal ecosystem. *Geobiology* **14**, 207-219 (2016).
189. A. H. Knoll, M. J. Follows, A bottom-up perspective on ecosystem change in the Mesozoic oceans. *Proceedings of the Royal Society B-Biological Sciences* **283**, 20161755 (2016).
190. R. E. Zeebe, P. Westbroek, A simple model for the $CaCO_3$ saturation state of the ocean: The "Strangelove", the "Neritan", and the "Cretan" Ocean. *Geochemistry Geophysics Geosystems* **4**, 1104 (2003).

191. A. Ridgwell, A Mid Mesozoic Revolution in the regulation of ocean chemistry. *Marine Geology* **217**, 339-357 (2005).
192. N. H. Landman *et al.*, Ammonite extinction and nautilid survival at the end of the Cretaceous. *Geology* **42**, (2014).
193. N. P. Kelley, N. D. Pyenson, Evolutionary innovation and ecology in marine tetrapods from the Triassic to the Anthropocene. *Science* **348**, 301-308 (2015).
194. J. J. Pospichal, Calcareous nannofossils at the K-T Boundary, El Kef - no evidence for stepwise, gradual, or sequential extinctions. *Geology* **22**, 99-102 (1994).
195. J. J. Pospichal, S. W. Wise Jr., F. Asaro, N. Hamilton, in *Global catastrophes in earth history: an interdisciplinary conference on impacts, volcanism, and mass mortality: Geological Society of America Special Paper 247,* V. L. Sharpton, P. D. Ward, Eds. (1990), vol. 247, pp. 497-507.
196. S. L. D'Hondt, T. D. Herbert, J. King, C. Gibson, in *The Cretaceous-Tertiary event and other catastrophes in Earth history: Geological Society of America Special Paper 307,* G. Ryder, D. Fastovsky, S. Gartner, Eds. (1996), pp. 303–317.
197. R. M. Corfield, N. J. Shackleton, J. Gerstel, R. Thunell, Danian Faunal Succession - Planktonic Foraminiferal Response to a Changing Marine-Environment - Comment and Reply. *Geology* **16**, 378-380 (1988).
198. K. J. Hsü *et al.*, Mass Mortality and Its Environmental and Evolutionary Consequences. *Science* **216**, 249-256 (1982).
199. L. R. Kump, Interpreting carbon-isotope excursions : Strangelove Oceans. *Geology* **19**, 299-302 (1991).
200. S. A. Alvarez *et al.*, Diversity decoupled from ecosystem function and resilience during mass extinction recovery. *Nature* **574**, 242-245 (2019).
201. J. Vellekoop *et al.*, Shelf hypoxia in response to global warming after the Cretaceous-Paleogene boundary impact. *Geology* **46**, 683-686 (2018).
202. W. Qin *et al.*, Confounding effects of oxygen and temperature on the TEX86 signature of marine Thaumarchaeota. *Proceedings of the National Academy of Sciences of the United States of America* **112**, 10979-10984 (2015).
203. S. J. Hurley *et al.*, Influence of ammonia oxidation rate on thaumarchaeal lipid composition and the TEX86 temperature proxy. *Proceedings of the National Academy of Sciences of the United States of America* **113**, 7762-7767 (2016).
204. R. W. Smith, T. S. Bianchi, X. X. Li, A re-evaluation of the use of branched GDGTs as terrestrial biomarkers: Implications for the BIT Index. *Geochimica Et Cosmochimica Acta* **80**, 14-29 (2012).
205. S. Fietz, A. Martinez-Garcia, C. Huguet, G. Rueda, A. Rosell-Mele, Constraints in the application of the Branched and Isoprenoid Tetraether index as a terrestrial input proxy. *Journal of Geophysical Research-Oceans* **116**, C10032 (2011).
206. R. Coccioni *et al.*, The Dan-C2 hyperthermal event at Gubbio (Italy): Global implications, environmental effects, and cause(s). *Earth and Planetary Science Letters* **297**, 298-305 (2010).
207. M. Gutjahr *et al.*, Very large release of mostly volcanic carbon during the Palaeocene–Eocene Thermal Maximum. *Nature* **548**, 573-577 (2017).
208. L. D. Stott, J. P. Kennett, New constraints on early Tertiary paleoproductivity from carbon isotopes in foraminifera. *Nature* **342**, 526-529 (1989).

209. S. V. Petersen *et al.*, Temperature and salinity of the Late Cretaceous Western Interior Seaway. *Geology* **44**, 903-906 (2016).
210. R. A. Duncan, D. G. Pyle, Rapid Eruption of the Deccan Flood Basalts at the Cretaceous Tertiary Boundary. *Nature* **333**, 841-843 (1988).
211. V. Courtillot *et al.*, Deccan Flood Basalts and the Cretaceous Tertiary Boundary. *Nature* **333**, 843-846 (1988).
212. V. Courtillot *et al.*, Deccan flood basalts at the Cretaceous-Tertiary boundary. *Earth and Planetary Science Letters* **80**, 361-374 (1986).
213. C. J. Sprain, P. R. Renne, G. P. Wilson, W. A. Clemens, High-resolution chronostratigraphy of the terrestrial Cretaceous-Paleogene transition and recovery interval in the Hell Creek region, Montana. *GSA Bulletin* **127**, 393-409 (2014).
214. A. L. Chenet, F. Fluteau, V. Courtillot, M. Gerard, K. V. Subbarao, Determination of rapid Deccan eruptions across the Cretaceous-Tertiary boundary using paleomagnetic secular variation: Results from a 1200-m-thick section in the Mahabaleshwar escarpment. *Journal of Geophysical Research-Solid Earth* **113**, B04101 (2008).
215. H. B. Vonhof, J. Smit, High-resolution late Maastrichtian early Danian oceanic Sr-87/Sr-86 record: Implications for Cretaceous-Tertiary boundary events. *Geology* **25**, 347-350 (1997).
216. M. Widdowson, K. G. Cox, Uplift and erosional history of the Deccan Traps, India: Evidence from laterites and drainage patterns of the Western Ghats and Konkan Coast. *Earth and Planetary Science Letters* **137**, 57-69 (1996).
217. E. Font *et al.*, Mercury anomaly, Deccan volcanism, and the end-Cretaceous mass extinction. *Geology* **44**, 171-174 (2016).
218. J. Smit, C. Koeberl, P. Claeys, A. Montanari, Mercury anomaly, Deccan volcanism and the end-Cretaceous mass extinction. *Geology* **44**, e381 (2016).
219. E. Font, T. Adatte, S. Planke, H. Svensen, W. M. Kürschner, Impact, volcanism, global change, and mass extinction. *Palaeogeography Palaeoclimatology Palaeoecology* **441**, 1-3 (2016).
220. D. Stuben *et al.*, Late Maastrichtian paleoclimatic and paleoceanographic changes inferred from Sr/Ca ratio and stable isotopes. *Palaeogeography Palaeoclimatology Palaeoecology* **199**, 107-127 (2003).
221. B. Samant, D. M. Mohabey, P. Srivastava, D. Thakre, Palynology and clay mineralogy of the Deccan volcanic associated sediments of Saurashtra, Gujarat: Age and paleoenvironments. *J Earth Syst Sci* **123**, 219-232 (2014).
222. A. S. Khadkikar, D. A. Sant, V. Gogte, R. V. Karanth, The influence of Deccan volcanism on climate: insights from lacustrine intertrappean deposits, Anjar, western India. *Palaeogeography Palaeoclimatology Palaeoecology* **147**, 141-149 (1999).
223. P. Ghosh, M. R. G. Sayeed, R. Islam, S. M. Hundekari, Inter-basaltic clay (bole bed) horizons from Deccan traps of India: Implications for palaeo-weathering and palaeo-climate during Deccan volcanism. *Palaeogeography Palaeoclimatology Palaeoecology* **242**, 90-109 (2006).
224. V. C. Bowman, J. E. Francis, R. A. Askin, J. B. Riding, G. T. Swindles, Latest Cretaceous-earliest Paleogene vegetation and climate change at the high southern latitudes: palynological evidence from Seymour Island, Antarctic Peninsula. *Palaeogeography Palaeoclimatology Palaeoecology* **408**, 26-47 (2014).

225. D. B. Kemp *et al.*, A cool temperate climate on the Antarctic Peninsula through the latest Cretaceous to early Paleogene. *Geology* **42**, 583-586 (2014).
226. V. C. Bowman, J. E. Francis, J. B. Riding, Late Cretaceous winter sea ice in Antarctica? *Geology* **41**, 1227-1230 (2013).
227. A. O'Dea, E. Hakansson, P. D. Taylor, B. Okamura, Environmental change prior to the K-T boundary inferred from temporal variation in the morphology of cheilostome bryozoans. *Palaeogeography Palaeoclimatology Palaeoecology* **308**, 502-512 (2011).
228. E. Barrera, G. Keller, Productivity across the Cretaceous/Tertiary boundary in high latitudes. *Geological Society of America Bulletin* **106**, 1254-1266 (1994).
229. T. Mizukami, K. Kaiho, M. Oba, Significant changes in land vegetation and oceanic redox across the Cretaceous/Paleogene boundary. *Palaeogeography Palaeoclimatology Palaeoecology* **369**, 41-47 (2013).
230. Y. Kajiwara, K. Kaiho, Oceanic Anoxia at the Cretaceous Tertiary Boundary Supported by the Sulfur Isotopic Record. *Palaeogeography Palaeoclimatology Palaeoecology* **99**, 151-162 (1992).
231. K. Kaiho *et al.*, Oceanic primary productivity and dissolved oxygen levels at the Cretaceous/Tertiary boundary: Their decrease, subsequent warming, and recovery. *Paleoceanography* **14**, 511-524 (1999).
232. L. Alegret, E. Thomas, Cretaceous/Paleogene boundary bathyal paleo-environments in the central North Pacific (DSDP Site 465), the Northwestern Atlantic (ODP Site 1049), the Gulf of Mexico and the Tethys: the benthic foraminiferal record. *Palaeogeography Palaeoclimatology Palaeoecology* **224**, 53-82 (2005).
233. J. Punekar *et al.*, A multi-proxy approach to decode the end-Cretaceous mass extinction. *Palaeogeography Palaeoclimatology Palaeoecology* **441**, 116-136 (2016).
234. E. Font *et al.*, Atmospheric halogen and acid rains during the main phase of Deccan eruptions: Magnetic and mineral evidence. *Volcanism, Impacts, and Mass Extinctions: Causes and Effects* **505**, 353-368 (2014).
235. T. R. Lyson *et al.*, Exceptional continental record of biotic recovery after the Cretaceous-Paleogene mass extinction. *Science*, (2019).
236. G. P. Wilson, Mammalian Faunal Dynamics During the Last 1.8 Million Years of the Cretaceous in Garfield County, Montana. *Journal of Mammalian Evolution* **12**, 53-76 (2005).
237. B. Samant, D. M. Mohabey, Palynoflora from Deccan volcano-sedimentary sequence (Cretaceous-Palaeogene transition) of central India: implications for spatio-temporal correlation. *Journal of Biosciences* **34**, 811-823 (2009).
238. B. Samant, S. Bajpai, Palynoflora from the Lakshmipur intertrappean deposits of Kutch, Gujarat: age implications. *Journal of the Palaeonotological Society of India* **Golden Jubilee Volume 50**, 169-176 (2005).
239. C. R. Marshall, P. D. Ward, Sudden and gradual molluscan extinctions in the latest Cretaceous of western European Tethys. *Science* **274**, 1360-1363 (1996).
240. W. J. Zinsmeister, R. M. Feldmann, M. O. Woodburne, D. H. Elliot, Latest Cretaceous Earliest Tertiary Transition on Seymour Island, Antarctica. *Journal of Paleontology* **63**, 731-738 (1989).
241. J. S. Adolfssen, D. J. Ward, Crossing the Boundary: An Elasmobranch Fauna from Stevns Klint, Denmark. *Palaeontology* **57**, 591-629 (2014).

242. N. Thibault, D. Husson, Climatic fluctuations and sea-surface water circulation patterns at the end of the Cretaceous era: Calcareous nannofossil evidence. *Palaeogeography Palaeoclimatology Palaeoecology* **441**, 152-164 (2016).
243. S. Abramovich, G. Keller, High stress late Maastrichtian paleoenvironment: inference from planktonic foraminifera in Tunisia. *Palaeogeography Palaeoclimatology Palaeoecology* **178**, 145-164 (2002).
244. G. Keller, *Guembelitria*-dominated late Maastrichtian planktic foraminiferal assemblages mimic early Danian in central Egypt. *Marine Micropaleontology* **47**, 71-99 (2003).
245. G. Keller, Low-diversity, late Maastrichtian and early Danian planktic foraminiferal assemblages of the eastern Tethys. *Journal of Foraminiferal Research* **34**, 49-73 (2004).
246. P. M. Hull, Life in the aftermath of mass extinctions. *Curr. Biol.* **25**, R941–R952 (2015).
247. P. A. Holroyd, G. P. Wilson, H. J. Hutchison, Temporal changes within the latest Cretaceous and early Paleogene turtle faunas of northeastern Montana. *Geological Society of America Special Papers*, 299-312 (2014).
248. D. A. Pearson, T. Schaefer, K. R. Johnson, D. J. Nichols, J. P. Hunter, in *The Hell Creek Formation and the Cretaceous-Tertiary Boundary in the Northern Great Plains,* J. H. Hartman, K. R. Johnson, D. J. Nichols, Eds. (Geological Society of America, Special Paper 361, 2002), pp. 145–167.
249. D. E. Fastovsky *et al.*, Shape of Mesozoic dinosaur richness. *Geology* **32**, 877-880 (2004).
250. S. C. Wang, P. Dodson, Estimating the diversity of dinosaurs. *Proceedings of the National Academy of Sciences of the United States of America* **103**, 13601-13605 (2006).
251. P. M. Sheehan, D. E. Fastovsky, C. Barreto, R. G. Hoffmann, Dinosaur abundance was not declining in a "3 m gap" at the top of the Hell Creek Formation, Montana and North Dakota: Reply. *Geology* **28**, 1151-1151 (2000).
252. P. M. Sheehan, D. E. Fastovsky, R. G. Hoffmann, C. B. Barreto, No statistical support for sudden (or gradual) extinction of dinosaurs: Comment. *Geology* **24**, 957-958 (1996).
253. J. D. Archibald, in *The Complete Dinosaur,* M. K. Brett-Surman, T. R. Holtz, J. O. Farlow, B. Walter, Eds. (Indiana Press, Bloomington, 2012), pp. 1027-1038.
254. P. M. Barrett, A. J. McGowan, V. Page, Dinosaur diversity and the rock record. *Proceedings of the Royal Society B-Biological Sciences* **276**, 2667-2674 (2009).
255. S. L. Brusatte *et al.*, The extinction of the dinosaurs. *Biological Reviews* **90**, 628-642 (2015).
256. A. A. Chiarenza *et al.*, Ecological niche modelling does not support climatically-driven dinosaur diversity decline before the Cretaceous/Paleogene mass extinction. *Nat Commun* **10**, (2019).
257. M. Schlüter, T. Steuber, M. Parente, J. Mutterlose, Evolution of a Maastrichtian-Paleocene tropical shallow-water carbonate platform (Qalhat, NE Oman). *Facies* **54**, 513-527 (2008).
258. T. Steuber, M. Schlueter, Strontium-isotope stratigraphy of Upper Cretaceous rudist bivalves: Biozones, evolutionary patterns and sea-level change calibrated to numerical ages. *Earth-Science Reviews* **114**, 42-60 (2012).
259. T. Steuber, S. F. Mitchell, D. Buhl, G. Gunter, H. U. Kasper, Catastrophic extinction of Caribbean rudist bivalves at the Cretaceous-Tertiary boundary. *Geology* **30**, 999-1002 (2002).

260. P. Bown, Calcareous nannoplankton evolution: a tale of two oceans. *Micropaleontology* **51**, 299-308 (2005).
261. I. Arenillas, J. A. Arz, E. Molina, Quantifying the evolutionary turnover across the K-T boundary catastrophic planktic foraminiferal extinction event at El Kef, Tunisia. *Gff* **124**, 121-126 (2002).
262. I. Arenillas, J. A. Arz, E. Molina, C. Dupuis, An independent test of planktic foraminiferal turnover across the Cretaceous/Paleogene (K/P) boundary at El Kef, Tunisia: Catastrophic mass extinction and possible survivorship. *Micropaleontology* **46**, 31-49 (2000).
263. I. Arenillas, J. A. Arz, E. Molina, Spanish and Tunisian Cretaceous/Tertiary boundary sections: A planktic foraminiferal biostratigraphic comparison and evolutionary events. *Gf* **122**, 11-12 (2000).
264. K. G. MacLeod, D. L. Whitney, B. T. Huber, C. Koeberl, Impact and extinction in remarkably complete K/T boundary sections from Demerara Rise, tropical western North Atlantic. *Geological Society of America Bulletin* **119**, 768-768 (2007).
265. B. T. Huber, K. G. MacLeod, R. D. Norris, Abrupt extinction and subsequent reworking of Cretaceous planktonic foraminifera across the Cretaceous-Tertiary boundary: Evidence from the subtropical North Atlantic. *Geol Soc Am Spec Pap* **356**, 277-289 (2002).
266. R. D. Norris, B. T. Huber, J. Self-Trail, Synchroneity of the K-T oceanic mass extinction and meteorite impact: Blake Nose, western North Atlantic. *Geology* **27**, 419-422 (1999).
267. G. Keller *et al.*, Environmental changes during the Cretaceous-Paleogene mass extinction and Paleocene-Eocene Thermal Maximum: Implications for the Anthropocene. *Gondwana Research* **56**, 69-89 (2018).
268. G. Keller, L. Li, N. MacLeod, The Cretaceous Tertiary boundary stratotype section at El Kef, Tunisia: How catastrophic was the mass extinction? *Palaeogeography Palaeoclimatology Palaeoecology* **119**, 221-254 (1996).
269. G. Keller, Extinction, Survivorship and Evolution of Planktic Foraminifera across the Cretaceous Tertiary Boundary at El-Kef, Tunisia. *Marine Micropaleontology* **13**, 239-263 (1988).
270. J. A. Arz, I. Arenillas, E. Molina, R. Sepulveda, Planktonic foraminiferal stability in the Upper Maastrichtian and the catastrophic mass extinction at the Cretaceous-Tertiary (K/T) boundary at Caravaca (Spain). *Rev Geol Chile* **27**, 27-47 (2000).
271. I. Arenillas, J. A. Arz, E. Molina, C. Dupuis, The Cretaceous/Paleogene (K/P) boundary at Ain Settara, Tunisia: Sudden catastrophic mass extinction in planktic foraminifera. *Journal of Foraminiferal Research* **30**, 202-218 (2000).
272. P. Claeys, W. Kiessling, W. Alvarez, in *Catastrophic events and mass extinctions: impacts and beyond: Geological Society of America Special Paper 356,* C. Koeberl, K. G. MacLeod, Eds. (2002), vol. 356, pp. 55 - 69.
273. K. R. Johnson, D. J. Nichols, M. Attrep, C. J. Orth, High-Resolution Leaf-Fossil Record Spanning the Cretaceous Tertiary Boundary. *Nature* **340**, 708-711 (1989).
274. J. R. Moore *et al.*, in *Through the End of the Cretaceous in the Type Locality of the Hell Creek Formation in Montana and Adjacent Areas: Geological Society of America Special Paper 503,* G. P. Wilson, W. A. Clemens, J. R. Horner, J. H. Hartman, Eds. (2014), pp. 123-135.
275. D. J. Nichols, K. R. Johnson, Plants and the K-T Boundary. *Plants and the K-T Boundary*, 1-280 (2008).

276. B. F. Bohor, E. E. Foord, P. J. Modreski, D. M. Triplehorn, Mineralogic Evidence for an Impact Event at the Cretaceous-Tertiary Boundary. *Science* **224**, 867-869 (1984).
277. J. F. Mchone, R. A. Nieman, C. F. Lewis, A. M. Yates, Stishovite at the Cretaceous-Tertiary Boundary, Raton, New-Mexico. *Science* **243**, 1182-1184 (1989).
278. S. R. Meyers, S. E. Peters, A 56 million year rhythm in North American sedimentation during the Phanerozoic. *Earth and Planetary Science Letters* **303**, 174-180 (2011).
279. R. A. DePalma *et al.*, A seismically induced onshore surge deposit at the KPg boundary, North Dakota. *Proceedings of the National Academy of Sciences of the United States of America* **116**, 8190-8199 (2019).
280. K. G. Miller *et al.*, Relationshp between mass extinction and iridium across the Cretaceous-Paleogene boundary in New Jersey. *Geology* **38**, 867-870 (2010).
281. B. F. Bohor, P. J. Modreski, E. E. Foord, Shocked Quartz in the Cretaceous-Tertiary Boundary Clays - Evidence for a Global Distribution. *Science* **236**, 705-709 (1987).
282. L. Alegret *et al.*, Cretaceous-Paleogene boundary deposits at Loma Capiro, central Cuba: Evidence for the Chicxulub impact. *Geology* **33**, 721-724 (2005).
283. R. A. Denne *et al.*, Massive Cretaceous-Paleogene boundary deposit, deep-water Gulf of Mexico: New evidence for widespread Chicxulub-induced slope failure. *Geology* **41**, 983-986 (2013).
284. A. R. Soria *et al.*, Slumping and a sandbar deposit at the Cretaceous-Tertiary boundary in the El Tecolote section (northeastern Mexico): An impact-induced sediment gravity flow. *Geology* **29**, 231-234 (2001).
285. L. Alegret *et al.*, The Cretaceous/Tertiary boundary: sedimentology and micropalaeontology at El Mulato section, NE Mexico. *Terra Nova* **14**, 330-336 (2002).
286. H. Sigurdsson, R. M. Leckie, G. D. Acton, e. al., Caribbean volcanism, Cretaceous/Tertiary impact, and ocean-climate history: synthesis of Leg 165. *Proc. ODP, Initial Reports 165*, 377-400 (1997).
287. W. Alvarez, F. Asaro, A. Montanari, Iridium profile for 10-million years across the Cretaceous-Tertiary boundary at Gubbio (Italy). *Science* **250**, 1700-1702 (1990).
288. H. V. Michel, F. Asaro, W. Alvarez, L. W. Alvarez, in *Init. Repts. DSDP, 62,* J. Thiede, T. L. Vallier, Eds. (U.S. Govt. Printing Office, Washington, 1981), vol. 62, pp. 847-849.
289. J. A. Wolfe, Paleobotanical Evidence for a June Impact Winter at the Cretaceous Tertiary Boundary. *Nature* **352**, 420-423 (1991).
290. D. J. Nichols, Plants at the K/T Boundary. *Nature* **356**, 295-295 (1992).
291. L. J. Hickey, L. J. Mcweeney, Plants at the K/T Boundary. *Nature* **356**, 295-296 (1992).
292. E. E. McIver, Paleobotanical evidence for ecosystem disruption at the Cretaceous-Tertiary boundary from Wood Mountain, Saskatchewan, Canada. *Canadian Journal of Earth Sciences* **36**, 775-789 (1999).
293. R. H. Tschudy, C. L. Pillmore, C. J. Orth, J. S. Gilmore, J. D. Knight, Disruption of the terrestrial plant ecosystem at the Cretaceous-Tertiary boundary, western interior. *Science* **225**, 1030-1032 (1984).
294. D. J. Nichols, Geologic and Biostratigraphic Framework of the Nonmarine Cretaceous-Tertiary Boundary Interval in Western North-America. *Review of Palaeobotany and Palynology* **65**, 75-84 (1990).
295. K. R. Johnson, L. J. Hickey, in *Global catastrophes in Earth history; an interdisciplinary conference on impacts, volcanism, and mass mortality,* V. L. Sharpton, P. D. Ward, Eds. (Geological Society of America Special Paper 247, 1990), pp. 433-444.

296. D. J. Nichols, R. F. Fleming, in *Global catastrophes in Earth history; an interdisciplinary conference on impacts, volcanism, and mass mortality,* V. L. Sharpton, P. D. Ward, Eds. (Geological Society of America Special Paper 247, 1990), pp. 445-455.
297. D. J. Nichols, J. L. Brown, M. Attrep, C. J. Orth, A New Cretaceous Tertiary Boundary Locality in the Western Powder River Basin, Wyoming - Biological and Geological Implications. *Cretaceous Research* **13**, 3-30 (1992).
298. K. R. Johnson, Megaflora of the Hell Creek and lower Fort Union Formations in the western Dakotas: Vegetational response to climate change, the Cretaceous-Tertiary boundary event, and rapid marine transgression. *Geological Society of America Special Paper* **361**, 329-391 (2002).
299. D. J. Nichols, Palynology and palynostratigraphy of the Hell Creek Formation in North Dakota: a microfossil record of plants at the end of Cretaceous time. *Geological Society of America Special Paper* **361**, 393-456 (2002).
300. V. Vajda, A. Bercovici, The global vegetation pattern across the Cretaceous-Paleogene mass extinction interval: A template for other extinction events. *Global and Planetary Change* **122**, 29-49 (2014).
301. A. R. Sweet, D. R. Braman, The K-T-Boundary and Contiguous Strata in Western Canada - Interactions between Paleoenvironments and Palynological Assemblages. *Cretaceous Research* **13**, 31-79 (1992).
302. R. Coccioni, S. Galeotti, K-T Boundary Extinction - Geologically Instantaneous or Gradual Event - Evidence from Deep-Sea Benthic Foraminifera. *Geology* **22**, 779-782 (1994).
303. J. Sepulveda *et al.*, Stable isotope constraints on marine productivity across the Cretaceous-Paleogene mass extinction. *Paleoceanography and Paleoclimatology* **34**, 1195-1217 (2019).
304. J. N. Milligan, D. L. Royer, P. J. Franks, G. R. Upchurch, M. L. McKee, No Evidence for a Large Atmospheric CO2 Spike Across the Cretaceous-Paleogene Boundary. *Geophysical Research Letters* **46**, 3462-3472 (2019).
305. G. P. Wilson, Mammals across the K/Pg boundary in northeastern Montana, USA: dental morphology and body-size patterns reveal extinction selectivity and immigrant-fueled ecospace filling. *Paleobiology* **39**, 429-469 (2013).
306. D. S. Robertson, W. M. Lewis, P. M. Sheehan, O. B. Toon, K-Pg extinction patterns in marine and freshwater environments: The impact winter model. *J Geophys Res-Biogeo* **118**, 1006-1014 (2013).
307. R. F. Fleming, D. J. Nichols, in *Extinction Events in Earth History,* E. G. Kauffman, O. H. Walliser, Eds. (Springer-Verlag, Berlin, 1990), pp. 347–350.
308. B. Blonder, D. L. Royer, K. R. Johnson, I. Miller, B. J. Enquist, Plant Ecological Strategies Shift Across the Cretaceous-Paleogene Boundary. *PLoS Biology* **12**, (2014).
309. M. P. Donovan, P. Wilf, C. C. Labandeira, K. R. Johnson, D. J. Peppe, Novel Insect Leaf-Mining after the End-Cretaceous Extinction and the Demise of Cretaceous Leaf Miners, Great Plains, USA. *PLoS One* **9**, (2014).
310. P. Wilf, C. C. Labandeira, K. R. Johnson, B. Ellis, Decoupled plant and insect diversity after the end-Cretaceous extinction. *Science* **313**, 1112-1115 (2006).
311. W. Kiessling, R. C. Baron-Szabo, Extinction and recovery patterns of scleractinian corals at the Cretaceous-Tertiary boundary. *Palaeogeography Palaeoclimatology Palaeoecology* **214**, 195-223 (2004).

312. W. Kiessling, E. Flugel, J. Golonka, Paleoreef maps: Evaluation of a comprehensive database on Phanerozoic reefs. *Aapg Bull* **83**, 1552-1587 (1999).
313. W. Kiessling, P. Claeys, in *Geological and biological effects of impact events,* E. Buffetaut, C. Koeberl, Eds. (Springer, Berlin, 2001), pp. 83-140.
314. E. Flügel, W. Kiessling, in *Phanerozoic Reef Patterns. SEPM Special Publication 72,* W. Kiessling, E. Flügel, J. Golonka, Eds. (2002), pp. 691-723.
315. S. Esmeray-Senlet, S. Ozkan-Altiner, D. Altiner, K. G. Miller, Planktonic Foraminiferal Biostratigraphy, Microfacies Analysis, Sequence Stratigraphy, and Sea-Level Changes across the Cretaceous-Paleogene Boundary in the Haymana Basin, Central Anatolia, Turkey. *Journal of Sedimentary Research* **85**, 489-508 (2015).
316. A. B. Smith, C. H. Jeffery, Selectivity of extinction among sea urchins at the end of the Cretaceous period. *Nature* **392**, 69-71 (1998).
317. M. Aberhan, W. Kiessling, Persistent ecological shifts in marine molluscan assemblages across the end-Cretaceous mass extinction. *Proceedings of the National Academy of Sciences of the United States of America* **112**, 7207-7212 (2015).
318. J. D. Stilwell, Patterns of biodiversity and faunal rebound following the K-T boundary extinction event in Austral Palaeocene molluscan faunas. *Palaeogeography Palaeoclimatology Palaeoecology* **195**, 319-356 (2003).
319. C. E. Sogot, E. M. Harper, P. D. Taylor, Biogeographical and ecological patterns in bryozoans across the Cretaceous-Paleogene boundary: Implications for the phytoplankton collapse hypothesis. *Geology* **41**, 631-634 (2013).
320. C. E. Sogot, E. M. Harper, P. D. Taylor, The Lilliput Effect in Colonial Organisms: Cheilostome Bryozoans at the Cretaceous-Paleogene Mass Extinction. *PLoS One* **9**, (2014).
321. E. Hakansson, E. Thomsen, Benthic extinction and recovery patterns at the K/T boundary in shallow water carbonates, Denmark. *Palaeogeography Palaeoclimatology Palaeoecology* **154**, 67-85 (1999).
322. T. A. Hansen, P. H. Kelley, D. M. Haasl, Paleoecological patterns in molluscan extinctions and recoveries: comparison of the Cretaceous-Paleogene and Eocene-Oligocene extinctions in North America. *Palaeogeography Palaeoclimatology Palaeoecology* **214**, 233-242 (2004).
323. J. Aguirre, J. I. Baceta, J. C. Braga, Recovery of marine primary producers after the Cretaceous-Tertiary mass extinction: Paleocene calcareous red algae from the Iberian Peninsula. *Palaeogeography Palaeoclimatology Palaeoecology* **249**, 393-411 (2007).
324. J. Aguirre, R. Riding, J. C. Braga, Late Cretaceous incident light reduction: evidence from benthic algae. *Lethaia* **33**, 205-213 (2000).
325. I. Arenillas, J. A. Arz, V. Gilabert, Blooms of aberrant planktic foraminifera across the K/Pg boundary in the Western Tethys: causes and evolutionary implications. *Paleobiology* **44**, 460-489 (2018).
326. L. Alegret, E. Thomas, Deep-sea environments across the Cretaceous/Paleogene boundary in the eastern South Atlantic Ocean (ODP Leg 208, Walvis Ridge). *Marine Micropaleontology* **64**, 1-17 (2007).
327. L. Alegret, Recovery of the deep-sea floor after the Cretaceous-Paleogene boundary event: The benthic foraminiferal record in the Basque-Cantabrian basin and in South-eastern Spain. *Palaeogeography Palaeoclimatology Palaeoecology* **255**, 181-194 (2007).

328. C. J. Hollis, K. A. Rodgers, R. J. Parker, Siliceous plankton bloom in the earliest tertiary of Marlborough, New-Zealand. *Geology* **23**, 835-838 (1995).
329. H. Brinkhuis, W. J. Zachariasse, Dinoflagellate cysts, sea level changes and planktonic foraminifers across the Cretaceous-Tertiary boundary at El Haria, Northwest Tunisia. *Marine Micropaleontology* **13**, 153-191 (1988).
330. P. M. Sheehan, D. E. Fastovsky, R. G. Hoffmann, C. B. Berghaus, D. L. Gabriel, Sudden Extinction of the Dinosaurs - Latest Cretaceous, Upper Great-Plains, USA. *Science* **254**, 835-839 (1991).
331. P. M. Sheehan, D. E. Fastovsky, C. Barreto, R. G. Hoffmann, Dinosaur abundance was not declining in a " 3 m gap " at the top of the Hell Creek Formation, Montana and North Dakota. *Geology* **28**, 523-526 (2000).
332. N. R. Longrich, T. Tokaryk, D. J. Field, Mass extinction of birds at the Cretaceous-Paleogene (K-Pg) boundary. *Proceedings of the National Academy of Sciences of the United States of America* **108**, 15253-15257 (2011).
333. N. R. Longrich, B. A. S. Bhullar, J. A. Gauthier, Mass extinction of lizards and snakes at the Cretaceous-Paleogene boundary. *Proceedings of the National Academy of Sciences of the United States of America* **109**, 21396-21401 (2012).
334. K. R. Johnson, Leaf-Fossil Evidence for Extensive Floral Extinction at the Cretaceous Tertiary Boundary, North-Dakota, USA. *Cretaceous Research* **13**, 91-117 (1992).
335. C. C. Labandeira, K. R. Johnson, P. Wilf, Impact of the terminal Cretaceous event on plant-insect associations. *Proceedings of the National Academy of Sciences of the United States of America* **99**, 2061-2066 (2002).
336. A. D. Barnosky *et al.*, Has the Earth's sixth mass extinction already arrived? *Nature* **471**, 51-57 (2011).
337. D. Jablonski, Extinctions - a Paleontological Perspective. *Science* **253**, 754-757 (1991).
338. D. A. Vilhena *et al.*, Bivalve network reveals latitudinal selectivity gradient at the end-Cretaceous mass extinction. *Sci Rep-Uk* **3**, 1790 (2013).
339. D. M. Raup, D. Jablonski, Geography of End-Cretaceous marine bivalve extinctions. *Science* **260**, 971-973 (1993).
340. P. D. Ward, W. J. Kennedy, Maastrichtian Ammonites from the Biscay Region (France, Spain). *Journal of Paleontology* **67**, 1-58 (1993).
341. P. R. Bown, J. A. Lees, J. R. Young, in *Coccolithophores: from molecular processes to global impact,* H. R. Thierstein, J. R. Young, Eds. (Springer, Berlin, 2004), pp. 481- 508.
342. M. N. Bramlette, E. Martini, The great change in calcareous nannoplankton fossils between the Maestrichtian and Danian. *Micropaleontology* **10**, 291-322 (1964).
343. J. Smit, J. Hertogen, An extraterrestrial event at the Cretaceous-Tertiary boundary. *Nature* **285**, 198-200 (1980).
344. I. Premoli-Silva, H. P. Luterbacher, The Cretaceous-Tertiary boundary in the Southern Alps. *Rivista Italiana di Paleontologia e Stratigrafia* **72**, 1183-1198 (1966).
345. J. Aguirre, R. Riding, J. C. Braga, Diversity of coralline red algae: origination and extinction patterns from the Early Cretaceous to the Pleistocene. *Paleobiology* **26**, 651-667 (2000).
346. M. Friedman, Ecomorphological selectivity among marine teleost fishes during the end-Cretaceous extinction. *Proceedings of the National Academy of Sciences of the United States of America* **106**, 5218-5223 (2009).

347. E. C. Sibert, R. D. Norris, New Age of the Fishes initiated by the Cretaceous-Paleogene mass extinction. *Proceedings of the National Academy of Sciences of the United States of America* **PNAS Early Edition**, 8537-8542 (2015).
348. E. Thomas, in *Large ecosystem perturbations: causes and consequences: Geological Society of America Special Paper 424,* S. Monechi, R. Coccioni, M. R. Rampino, Eds. (2007), pp. 1–23.
349. S. J. Culver, Benthic foraminifera across the Cretaceous-Tertiary (K-T) boundary: a review. *Marine Micropaleontology* **47**, 177-226 (2003).
350. E. Thomas, in *Global catastrophes in earth history: An interdisciplinary conference on impacts, volcanism and mass mortality: Geological Society of America Special Paper 247*. (1990), pp. 481-496.
351. L. Alegret, E. Thomas, Upper Cretaceous and lower Paleogene benthic foraminifera from northeastern Mexico. *Micropaleontology* **47**, 269-316 (2001).
352. A. M. T. Elewa, Paleobiogeography of Maastrichtian to early Eocene Ostracoda of North and West Africa and the Middle East. *Micropaleontology* **48**, 391-398 (2002).
353. C. J. Hollis, C. P. Strong, K. A. Rodgers, K. M. Rogers, Paleoenvironmental changes across the Cretaceous/Tertiary boundary at Flaxbourne River and Woodside Creek, eastern Marlborough, New Zealand. *New Zealand Journal of Geology and Geophysics* **46**, 177-197 (2003).
354. H. Brinkhuis, J. P. Bujak, J. Smit, G. J. M. Versteegh, H. Visscher, Dinoflagellate-based sea surface temperature reconstructions across the Cretaceous-Tertiary boundary. *Palaeogeography Palaeoclimatology Palaeoecology* **141**, 67-83 (1998).
355. U. Bleil, in *Init. Repts. DSDP, 86,* G. R. Heath, L. H. Burckle, e. al., Eds. (U.S. Govt. Printing Office, Washington, 1985), pp. 441-458.
356. G. R. Dickens, J. Backman, Core alignment and composite depth scale for the lower Paleogene through uppermost Cretaceous interval at Deep Sea Drilling Project Site 577. *Newsletters on Stratigraphy* **46**, 47–68 (2013).
357. A. S. Henriksson, Biochronology of the Terminal Cretaceous Calcareous Nannofossil Zone of Micula-Prinsii. *Cretaceous Research* **14**, 59-68 (1993).
358. A. Boersma, in *Initial Rep. Deep Sea Drill. Proj. 62,* J. Thiede, T. L. Vallier, Eds. (U.S. Govt. Printing Office, Washington, D.C., 1981), pp. 377-396.
359. A. D. Chave, in *Initial Rep. Deep Sea Drill. Proj. 74,* J. H. Blakeslee, M. Lee, Eds. (U.S. Govt. Printing Office, Washington, D.C., 1984), pp. 525-531.
360. J. A. Alcalá-Herrera, E. L. Grossman, S. Gartner, Nannofossil Diversity and Equitability and Fine-Fraction Delta C-13 across the Cretaceous Tertiary Boundary at Walvis Ridge Leg-74, South-Atlantic. *Marine Micropaleontology* **20**, 77-88 (1992).
361. N. Hamilton, in *Proc. ODP, Sci. Repts., 113,* P. F. Barker, J. P. Kennett, e. al., Eds. (Ocean Drilling Program, College Station, TX, 1990).
362. H. V. Michel, F. Asaro, W. Alvarez, L. W. Alvarez, in *Proc. ODP, Sci. Results, 113,* P. F. Barker, J. P. Kennett, Eds. (Ocean Drilling Program, College, Station, TX, 1990), vol. 113, pp. 159-168.
363. B. T. Huber, K. G. Macleod, N. A. Tur, Chronostratigraphic framework for upper Campanian-Maastrichtian sediments on the blake nose (subtropical North Atlantic). *Journal of Foraminiferal Research* **38**, 162-182 (2008).

364. W. A. Berggren *et al.*, Integrated Paleocene calcareous plankton magnetobiochronology and stable isotope stratigraphy: DSDP Site 384 (NW Atlantic Ocean). *Palaeogeography Palaeoclimatology Palaeoecology* **159**, 1-51 (2000).